Surface Engineering Carbon Nanotube Coated Optical Fibre Sensors For Real-Time Monitoring Of Liquid Chemical Concentrations

I C Lam

PhD 2025

Surface Engineering Carbon Nanotube Coated Optical Fibre Sensors for Real-Time Monitoring of Liquid Chemical Concentrations

lek Cheong Lam

A thesis submitted in partial fulfilment of the requirements of Manchester Metropolitan University for the degree of Doctor of Philosophy

Department of Science and Engineering Manchester Metropolitan University

2025

ABSTRACT

Environmental pollution is a major factor causing the degradation of the environment around us, whether it is emitted naturally or artificially. The exponential advancement of technologies has increased the rate of industrialisation, and before we know it, their chemical emissions have already caused irreparable damage. Consequently, accurate, real-time monitoring of liquid chemical concentrations is vital for maintaining public health, industrial safety and environmental protection. Traditional methods for water quality monitoring rely heavily on laboratory-based techniques that are time-consuming, complex, and unsuitable for large-scale field deployment. This thesis proposes the development and validation of a novel, low-cost, simple-to-fabricate optical fibre sensor platform based on single-walled carbon nanotube coatings applied to standard single-mode optical fibre. The sensor platform operates on an intensity-modulated refractive index sensing mechanism, eliminating complex computational methods for spectrally resolved detection and the need for speciality fibres, thus enabling a compact and scalable design suitable for remote and in situ applications.

The theoretical simulations of a Long Period Fibre Grating sensor showed that a $0.5\mu m$ thickness carbon nanotube coating with a 1.60-1.70RI would yield higher sensitivity for detecting a surrounding medium with a range of 1.30-1.44RI. The coating was experimentally applied through the fabrication of single-walled carbon nanotube coated single mode fibres using a reproducible spray coating methodology. A stabilised 0.00025% (w/w) carbon nanotube suspension was

synthesised for deposition. Amongst the fabricated variants, a 3cm double-coated SWCNT-SMF sensor with an approximate thickness of 0.5 μm has demonstrated the highest performance, with sensitivities of around 20.886 dB/RIU and 5.26 dB/RIU between the ranges 1.3335-1.3451RI and 1.3451RI-1.3789RI respectively. The fabricated sensors have all shown instantaneous response and baseline recovery within 10 seconds, confirming their real-time monitoring capabilities.

By eliminating wavelength-shift analysis and enabling simple bandpass-filter readouts, this sensor platform offers advancement in the development of simplistic, miniaturised and multiplexable chemical sensors with electromagnetic immunity. The findings lay the groundwork for further enhancements through CNT functionalisation for selective detection and gaseous sensing of volatile organic compounds. This research contributes a versatile and accessible sensing technology with strong potential for industrial processes and environmental monitoring.

ACKNOWLEDGEMENTS

Primarily and most importantly, I would like to express my sincerest gratitude to my wife and family for their mental, physical and financial support over the past few years. My gratefulness towards them cannot be expressed enough through these words.

I would like to deeply thank Dr David Sawtell and Dr Kirstie Andrews on my supervisory team for their advice and help on everything all throughout the Ph.D especially during COVID-19. I would also like to thank Dr Tiziana Denaro, for her kind teachings on experimental aspects of the research. None of this would have been accomplished without their generous guidance.

I would like to further thank Hayley Andrews for her incredible help and teachings with the SEM spectroscopy and Dr Muhammad Ijaz for lending me specialised equipment at the time of need.

Lastly, I want to thank MMU for providing me with such an amazing opportunity with the studentship for all these years.

CONTENTS

1	Introduction	. 1
	1.1 Background	. 1
	1.2 Aims and Objectives	. 4
	1.3 List of Publications	. 4
	1.4 Thesis Structure	. 5
2	Literature Review	. 7
	2.1 Liquid Chemical Monitoring Technologies	. 7
	2.1.1 UV-Vis Spectroscopy	. 7
	2.1.2 Electrochemical Sensors (Potentiometric & Amperometric)	. 9
	2.1.3 High Performance Liquid Chromatography	12
	2.1.4 Optical Fibre Sensors	13
	2.2 Optical Fibre Sensing Principles and Configurations	16
	2.2.1 Optical fibre Structures	16
	2.2.2 Operating Principles	18
	2.2.2.1 Evanescent Wave Theory	19
	2.2.2.2 Evanescent Wave Parameters	21
	2.2.3 Long Period Fibre Gratings	22
	2.3 Carbon Nanomaterial Integrated Optical Fibre Sensors	24
	2.3.1 Graphene	26
	2.3.1.1 Graphene Integrated Mach Zehnder Interferometer Sensors	27

2.3.1.2 Graphene Integrated Fibre Bragg Grating Sensors
2.3.2 Carbon Nanotubes
2.3.2.1 Carbon Nanotube Integrated Mach Zehnder Interferomete
Sensors33
2.3.2.2 Carbon Nanotube Coated Fibre Bragg Grating Sensors 34
2.3.2.3 Carbon Nanotube Coated Long Period Fibre Grating Sensors 35
2.3.3 Summary
2.4 Research Gap3
3 Coating Methodologies40
3.1 Chemical Vapour Deposition
3.2 Dip Coating42
3.3 Spray Coating
3.4 The Methodology Adopted: Comparison and Discussion
4 Simulation: Carbon Nanomaterial Coated Long Period Fibre Grating Sensor. 46
4.1 Introduction
4.2 CNT-LPFG Working Principle
4.3 OptiGrating Simulation Methodology
4.4 Simulation Results
4.4.1 Uncoated LPFG
4.4.2 Various RI Coatings
4 4 2 1 1 50RL Coated LPEG 55

	4.4.2.2 1.60RI Coated LPFG 5.	/
	4.4.2.3 1.70RI Coated LPFG59	9
	4.4.2.4 1.80RI Coated LPFG6	1
	4.4.2.5 1.90RI Coated LPFG	3
	4.5 Comparison: Results against Theory	5
	4.6 Comparison: Amongst Various RI coatings	6
	4.7 Comparison: Coating Thickness	8
	4.8 Discussion	1
	4.8.1 Sensitivity vs Linearity	1
	4.8.2 Abnormalities and Mode Transitions	2
	4.8.3 Comparison to Literatures	3
	4.9 Summary	6
5	Fabrication of SWCNT-SMF sensor	8
	5.1 Introduction	8
	5.2 Experimental Methodologies	0
	5.2.1 Fibre Sensor Probe Fabrication Methodology80	0
	5.2.1.1 SMF Preparation	0
	5.2.1.2 SWCNT Solution Preparation87	1
	5.2.1.3 Coating Stage83	3
	5.2.2 Characterisation Methodology	5
	5.2.3 RI Sensing Methodology86	6

	5.2.3.1 RI Sensor Setup	. 86
	5.2.3.2 RI Sensing Test Solution Preparation	. 87
5.3	Experimental Results and Discussion	. 88
5	.3.1 Prepared SWCNT solution	. 88
	5.3.1.1 0.005% SWCNT Solution	. 89
	5.3.1.2 0.0005% SWCNT Solution	. 89
	5.3.1.3 0.00025% SWCNT Solution	90
	5.3.1.4 0.005% SWCNT Solution with Dispersant	. 91
	5.3.1.5 0.0005% SWCNT Solution with Dispersant	92
	5.3.1.6 0.00025% CNT Solution with Dispersant	93
	5.3.1.7 SWCNT Solution: Choice and Discussion	. 93
5	.3.2 Characterisation of SWCNT-SMFs	. 95
	5.3.2.1 Single Coated SMFs	. 95
	5.3.2.2 Double Coated SMFs	. 97
	5.3.2.3 Quadruple Coating Layer SMFs	99
5	.3.3 RI-Sensing of SWCNT-SMF	101
	5.3.3.1 3cm Non-Coated Fibre	102
	5.3.3.2 1cm Single Coated SWCNT-SMF	105
	5.3.3.3 3cm Single Coated SWCNT-SMF	106
	5.3.3.4 1cm Double Coated SWCNT-SMF	108
	5.3.3.5 3cm Double Coated SWCNT-SMF	110

	5.3.3.6 Quadruple Coated SWCNT-SMF	112
	5.3.3.7 Repeatability	113
	5.3.3.8 Comparison and Discussion	114
	5.4 Limitations	120
	5.5 Summary	121
6 (Conclusion and Further works	123
	6.1 Conclusion	123
	6.2 Further Works	125
	6.2.1 Future Research	125
	6.3 Summary	126
7 I	References	128
ΛС	DDENINIY	1/5

LIST OF TABLES

Table 1 Typical core and cladding dimensions of single-mode and multimode
fibres
Table 2 Step-index single mode optical fibre parameters
Table 3 Parameters of the Long Period Fibre Grating used in the OptiGrating 4.2.3
software
Table 4 The calculated sensitivities of the simulated CNT-LPFG sensor in
correspondence to specific RI detecting ranges
Table 5 Sensitivity of Intensity Modulated carbon nanomaterial coated LPFG
Sensors from existing literatures
Table 6 Chemical Component and their corresponding weight percentages of the
Aqueous CNT dispersant
Table 7 The RIs of the various synthesized concentrations of Dextrose solution
88

LIST OF FIGURES

Figure 1 Typical structure of an optic fibre
Figure 2 Refractive index profile of step-index and graded-index fibres 18
Figure 3 Diagram showing the reflection and refraction which occurs at the core-
cladding interface when the angle of incidence is smaller than the critical angle.
Figure 4 Diagram showing an induced evanescent wave due to a totally internally
reflected light ray
Figure 5 Mode conversion from the fundamental core mode into a forward
propagating cladding mode in an LPFG
Figure 6 Schematic illustration of a carbon nanomaterial coated LPFG 48
Figure 7. Results from an Uncoated LPFG showing the transmission spectral
response between 1.5250-1.675μm wavelengths
Figure 8. Results from an Uncoated LPFG showing the transmittivity response of
the first attenuation band located at 1.550 μm wavelength against the SRI 55
Figure 9. OptiGrating 4.2.3 simulation results from a 1.50RI Coated LPFG with
$0.50\mu m$ overlay thickness showing the transmission spectral response (a)
between 1.525-1.675 μm wavelength (b) Closeup of the first attenuation band
between 1.525-1.675 µm wavelength. 56
Figure 10. Results from a 1.50RI coated LPFG of 0.5µm thickness show the
transmittivity response of the first attenuation band located at 1.550µm
wavelength against the SRI
Figure 11. OptiGrating 4.2.3 simulation results from a 1.60RI Coated LPFG with
$0.50 \mu m$ overlay thickness showing the transmission spectral response (a)

between 1.525-1.675 μm wavelength (b) Closeup of the first attenuation band
between 1.525-1.675 µm wavelength. 58
Figure 12. Results from a 1.60RI coated LPFG of $0.5\mu m$ thickness show the
transmittivity response of the first attenuation band located at 1.550 μm
wavelength against the SRI
Figure 13. OptiGrating 4.2.3 simulation results from a 1.70RI Coated LPFG with
$0.50\mu m$ overlay thickness showing the transmission spectral response (a)
between $1.525-1.675 \mu m$ wavelength (b) Closeup of the first attenuation band
between 1.525-1.675μm wavelength60
Figure 14. Results from a 1.70RI coated LPFG of $0.5 \mu m$ thickness showing the
transmittivity response of the first attenuation band located at 1.550 μm
wavelength against the SRI61
Figure 15 OptiGrating 4.2.3 simulation results from a 1.80RI Coated LPFG with
$0.50\mu m$ overlay thickness showing the transmission spectral response (a)
between $1.525-1.675 \mu m$ wavelength (b) Closeup of the first attenuation band
between 1.525-1.675μm wavelength62
Figure 16. Results from a 1.80RI coated LPFG of $0.5 \mu m$ thickness showing the
transmittivity response of the first attenuation band located at 1.550 μm
wavelength against the SRI63
Figure 17. OptiGrating 4.2.3 simulation results from a 1.90RI Coated LPFG with
$0.50\mu m$ overlay thickness showing the transmission spectral response (a)
between $1.525-1.675 \mu m$ wavelength (b) Closeup of the first attenuation band
hetween 1 525-1 675µm wavelength 64

Figure 18 Results from a 1.80RI coated LPFG of $0.5\mu m$ thickness showing the
transmittivity response of the first attenuation band located at 1.550 μm
wavelength against the SRI65
Figure 19 Comparison with Different Refractive Indexes of Coatings a) Between
1.50-1.90RI b) Between 1.70RI-2.90RI
Figure 20 The transmittivity response of the intensity minima at the $1.550 \mu m$
attenuation band against the SRI with variations of thickness (0.50 μm , 0.52 μm
and 0.54 mm) for a) 1.50RI Coated LPFG b) 1.60RI Coated LPFG c) 1.70RI Coated
LPFG d) 1.80RI Coated LPFG e) 1.90RI Coated LPFG
Figure 21 Schematic illustration of the prepared SMF
Figure 22 Example Coating Setup for the prepared SMF-28 Fibre with masking
tape on the four corners of the glass plate platform for temperature
measurements
Figure 23 Schematic Illustration on SWCNT-SMFs mounted on a) a horizonta
adhesive SEM specimen stub, b) a vertical adhesive specimen stub
Figure 24 Image of the used equipment with the SWCNT-SMF integrated into the
RI sensing setup86
Figure 25 Illustration and model of the SWCNT-SMF sensing element integrated
into the RI sensing setup
Figure 26 Image of an emptied jar of 0.005% concentration (w/w) SWCNT
solution showing severe adherence of SWCNTs on the inside with huge clumps
of SWCNTs at the base
Figure 27 Image of a jar of 0.0005% concentration (w/w) SWCNT solution
showing some adherence of SWCNTs to the inside surface of the jar with splitting
between the SWCNT and IPA-Water90

Figure 28 Image of a jar of 0.00025% concentration (w/w) CNT solution showing
minor adherence of CNTs to the inside surface of the jar and splitting of the CNT
and IPA-Water. 91
Figure 29 Image of a 0.005% concentration (w/w) SWCNT solution with
dispersant that is half-poured showing large clumps of SWCNT adherence to the
inside of the jar91
Figure 30 Image of the base of an emptied 0.001% concentration (w/w) SWCNT
solution with dispersant showing giant clumps of CNTs at the base of the jar. 92
Figure 31 Image of a 0.0005% concentration (w/w) SWCNT solution with
dispersant showing minor adherence to the inside of the jar
Figure 32 Image of a 0.00025% concentration (w/w) SWCNT solution with
dispersant with minimal SWCNTs adhered to the inside of the jar 93
Figure 33 SEM Imagery of a 1cm single coated SMF showing SWCNT deposits
and uncoated areas (enclosed by the red outline) at a) 1000x magnification b)
10,000x magnification96
Figure 34 SEM Imagery of a 3cm single coated SMF showing SWCNT deposits
and uncoated areas (enclosed by the red outline) at a) 1000x magnification b)
10,000x magnification
Figure 35 SEM Imagery of a $1\mu m$ double coated SMF showing SWCNT deposits
at a) 1000x magnification b) 10,000x magnification
Figure 36 SEM Imagery of a $3\mu m$ double coated SMF showing SWCNT deposits
at a) 1000x magnification b) 10,000x magnification
Figure 37 SEM Imagery of a 1cm quadruple coated SMF showing heavy deposits
of SWONTs

Figure 38 SEM Imagery of a 3cm quadruple coated SMF showing heavy deposits
of SWCNTs
Figure 39 Optical Response from the uncoated SMF when subjected to test
solutions of various RIs with a) showing the whole peak b) zoomed into the peak
Figure 40 Intensity Response of the non-coated SMF against SRI at the
wavelength point of 1571.757 \it{nm} with error bars based on standard error across
19 samples a) intensity (units) against SRI b) Loss (dB) against SRI104
Figure 41 Optical Response from a 1 cm single coated SWCNT-SMF when
subjected to test solutions of various RIs with a) showing the whole peak b)
zoomed into the peak
Figure 42 Intensity Response of the 1cm single coated SWCNT-SMF against SRI
at the wavelength point of 1571.757 nm with error bars based on standard error
across 19 samples a) intensity (units) against SRI b) Loss (dB) against SRI106
Figure 43 Optical Response from a 3 nm single coated SWCNT-SMF when
subjected to test solutions of various RIs with a) showing the whole peak b)
zoomed into the peaks
Figure 44 Intensity Response of the $3cm$ single coated SWCNT-SMF against SRI
at the wavelength point of 1571.757 nm with error bars based on standard error
across 19 samples a) intensity (units) against SRI b) Loss (dB) against SRI108
Figure 45 Optical Response from a 1 $\it cm$ double coated SWCNT-SMF when
subjected to test solutions of various RIs with a) showing the whole peak b)
zoomed into the peak

Figure 46 Intensity Response of the 1cm double coated SWCNT-SMF against ERI
at the wavelength point of 1571.757nm with error bars based on standard error
across 19 samples a) intensity (units) against SRI b) Loss (dB) against SRI110
Figure 47 Optical Response from a $3cm$ double coated SWCNT-SMF when
subjected to test solutions of various RIs with a) showing the whole peak b)
zoomed into the peak
Figure 48 Intensity Response of the $3\it{cm}$ double coated SWCNT-SMF against SRI
at the wavelength point of 1571.757 $\it nm$ with error bars based on standard error
across 19 samples a) intensity (units) against SRI b) Loss (dB) against SRI112
Figure 49 Quadruple coated SWCNT-SMFs demonstrating no response and only
background noise
Figure 50 Results depicting repeated RI tests for 3cm Double Coated SWCNT-
SMFs
Figure 51 SEM imagery of the $3cm$ double coated SWCNT-SMF cross-section
showing an approximate 0.5 μm thick SWCNT coating around the 125 \pm 0.7 μm
cladding diameter of the SMF-28117

LIST OF ABBREVIATIONS AND ACRONYMS

CNT - Carbon Nanotube

CVD - Chemical Vapour Deposition

DWCNT - Double-walled Carbon Nanotubes

EC - Electrochemical

EM - Electromagnetic

ERI - Effective Refractive Index

FBG - Fibre Bragg Gratings

GO - Graphene Oxide

HPLC - High-performance Liquid Chromatography

IPA - Isopropanol

IWD - IPA-Water-Dispersant

LPFG - Long Period Fibre Grating

MWCNT - Multi-walled Carbon Nanotubes

MZI - Mach Zehnder Interferometer

OC - Optical Circulator

OLS - Optical Light Source

PAH – Polycyclic Aromatic Hydrocarbons

PCB - Polychlorinated Biphenyls

PCF - Photonic Crystal Fibre

rGO - Reduced Graphene Oxide

RH - Relative Humidity

RI - Refractive Index

SEM – Scanning Electron Microscopy

SMF – Single-mode Fibre

SRI – Surrounding Refractive Index

SWCNT - Single-walled Carbon Nanotube

SWCNT-SMF - Single-walled Carbon Nanotube Coated Single-mode Fibre

TFBG - Tilted Fibre Bragg Grating

UV-Vis - Ultraviolet-visible

1.1 Background

Historical events have taught us the significance of environmental pollution through the consequences of excessive mortalities. With the technological advancement of civilisations since the Industrial Revolution, the demand for chemicals has significantly increased in various sectors such as industrial manufacturing, agriculture, energy production and healthcare. The 1970s Woburn water well contamination, a consequence of improper industrial waste disposal; The 1930 Meuse Valley Fog, a combination of climate and industrial-induced pollution disaster; the 1948 Donora Smog, an industrial over-emission of hydrogen fluoride and sulphur dioxide; the 1952 Great Smog of London, are further examples of the over-emission of pollutants as a result of the industrial revolution emitted from coal power plants and vehicle exhausts. These devasting

disasters have inspired the beginning of environmental pollution monitoring and highlighted their importance.

Water is necessary for the survival of all living species and the preservation and maintenance of good water quality is crucial to our ecosystem and human health, which can further impact socio-economic factors. Heavy metals such as lead, mercury, and arsenic, organic solvents such as benzene and formaldehyde, as well as chlorinated/polycyclic aromatic industrial chemicals such as polychlorinated biphenyls (PCBs) and polycyclic aromatic hydrocarbons (PAHs), are all waterborne pollutants that have affected our water quality across the world (Wulandari et al., 2024; N. M. Ali et al., 2025). Certain water pollutants have been known to be associated with neurological and psychiatric disorders as well as short and long-term physical ailments such as skin diseases, diarrhoea and cancer (Bochynska et al., 2024). For instance, long-term exposure to lead has been known to be linked with cognitive impairments in both adults and children (Goyer, 1993; Ara and Usmani, 2015), whilst benzene is found to be a potent carcinogen causing leukaemia (Reynoso-Noverón et al., 2024).

Traditionally, water quality and various chemical analysis relied on laboratory-based setups with varied techniques, including optical spectroscopy, electrochemistry, and chromatography (Y. Kim et al., 2024; Thakur and Devi, 2024). Conventional methods possess inefficient, complex, costly, and lengthy processes (Ahmed et al., 2020; Zainurin et al., 2022; Essamlali et al., 2024). In response, this thesis explores the development and application of carbon nanotube integrated Optical fibre sensors for liquid chemical concentration monitoring based on refractive index (RI) variation of the analyte. The proposed

sensor system takes a simplistic design approach to detect liquid chemical concentrations with high sensitivity, leveraging the recent innovations in photonics, carbon nanomaterials, and chemical sensing.

In contrast to the conventional methodologies, optical sensor systems offers continuous, real-time monitoring capabilities which enable swift identification of water quality deviation, allowing for prompt remedial actions as emphasized in recent literatures (M. A. Butt et al., 2022; Y. Kim et al., 2024; Lyu et al., 2024). Furthermore, emerging studies highlight the sensitivity of optical sensor systems and their ability to detect subtle changes in contaminant concentrations (Zainurin et al., 2022) (Manish Kumar et al., 2024; S.-q. Zhang et al., 2024; Z. Zhang et al., 2024).

In summary, this research contributes towards the growing body of academic research focused on enhancing water quality monitoring by exploiting carbon nanotube (CNT) integrated optical fibre systems for liquid chemical detection. CNTs offer an exceptional surface area of carbon nanotubes, chemical stability and tuneable functionalisation capabilities, making them highly responsive to a wide range of chemical species. When integrated into optical fibre sensor systems, it enables real-time, remote and highly sensitive detection of contaminants based on intensity modulations. This synergy of the two allows for the development of miniaturised, low-power, and robust sensor platforms capable of operating in harsh environments. The proposed CNT-based optic sensor system offers a promising solution for proactive large-scale environmental management and public health protection.

1.2 Aims and Objectives

This research aims to develop a fully functional CNT coated optical fibre sensor system for real-time and remote monitoring of liquid chemical concentrations based on refractive index changes. The refractive index sensing working principle will be a proof of concept and foundation for sensitive yet versatile liquid concentration monitoring platform. The following objectives will be covered through this thesis:

- Comprehensive literature review on the working theory of existing chemical sensors, coated waveguides and various fibre-based detection methodologies.
- Simulate CNT coated LPFG sensors subjected to an ambient RI range between 1.30-1.44RI to verify the theoretical expectations and investigate various coating parameters. These parameters include simulating coating RIs between 1.50–1.90RI at coating thicknesses between 0.50-0.54μm.
- Synthesis of a stable CNT solution suitable for spray coating.
- Fabrication and Characterisation of CNT optical fibre sensor with various coating durations at lengths of 1 cm and 3 cm.
- Real-time Measurement of varying dextrose solution concentrations with an RI range of 1.3335-1.3789RI to verify the functionality of the fabricated CNT optical fibre sensors.

1.3 List of Publications

Minglong Zhang, Iek Cheong Lam, Arun Kumar, Kin Kee Chow, Peter Han Joo
 Chong. Optical environmental sensing in wireless smart meter network. AIMS

Electronics and Electrical Engineering, 2018, 2(3): 103-116. doi: 10.3934/ElectrEng.2018.3.103

Chow, K.K. and Lam, I.C., 2018, December. Carbon Nanotubes Deposited
 Optical Fibers for Continuous Refractive Index Sensing Applications. In 2018

 IEEE British and Irish Conference on Optics and Photonics (BICOP) (pp. 1-4).
 IEEE.

1.4 Thesis Structure

This section presents and details the organisation of the presented thesis.

Chapter 2 provides a comprehensive literature review, starting with a background analysis of existing liquid chemical sensing technologies. The study then moves on to studying Optical fibre sensors in terms of their theory, working principle and existing hybrid Optical fibre sensors.

Chapter 3 discusses the various CNT coating methodologies, evaluating their advantages and disadvantages. It further explains the rationale for the adopted methodology used for the fabrication in Chapter 5.

Chapter 4 models various carbon nanotube coated long-period fibre gratings that are subjected to simulation in an ambient environment of different RIs. The simulation intends to analyse the effects of an additional layer of darker material around the cladding and compare it with different RIs and thicknesses of the coating. The chapter concludes by discussing the variations of coated long-period fibre grating (LPFG) with optimal sets of parameters identified.

Chapter 5 presents the physical fabrication and practical experimentation of the carbon nanotube coated single mode fibres. It discusses how a stabilized coating

solution is synthesized and the chosen variation for this research. The chapter further details the experimentations to integrate the coated fibre into the RI sensing setup, characterisation and discussion of the fabricated fibres.

Chapter 6 concludes this thesis with a discussion on future potential directions and expansions that are envisioned by this work and to contribute more valuable studies to the literature.

2 LITERATURE REVIEW

2.1 Liquid Chemical Monitoring Technologies

Currently, existing methodologies and techniques are designed to detect aqueous chemical concentrations used across various industrial, environmental and laboratory settings. Examples include ultraviolet—visible spectroscopy (UV-Vis), electrochemical sensors, ultrasonic sensors and optical sensors (Ahmed et al., 2020; Y. Kim et al., 2024). Each type of sensor operates with a distinct set of sensing principles and can differ considerably from one and another due to their applications (Szulczyński and Gębicki, 2017; Zainurin et al., 2022).

2.1.1 UV-Vis Spectroscopy

UV-Vis spectroscopy analysis is a commonly used analytical technique in diverse fields of chemistry, from environmental monitoring to food industries (F. Haque et al., 2021; Khalid et al., 2024). The technique can provide both quantitative

and qualitative analysis of chemical species in a particular sample by measuring the amount of light absorption at specific wavelength. The principle of UV-VIS relies on the Beer-Lambert Law that relates the amount of light absorbance to concentration.

$$A = \varepsilon cl \tag{1}$$

Where A represents absorbance, ε is molar absorptivity, c is the concentration of the analyte and l is the optical path length. As light from a broadband source in the UV-VIS range passes through a liquid sample, certain wavelengths are absorbed by the molecules. A detector would measure the transmitted light intensity and compares it to the incident light to obtain the amount of absorbance. The absorbance spectrum (absorbance against wavelength) reveals the characteristic peaks of specific chemical species or functional groups (Y. Guo et al., 2020; Ríos-Reina and Azcarate, 2022).

UV-Vis spectroscopic analysers stand out for their non-destructive, rapid, efficient and cost-effective capabilities (Shi et al., 2022; Sudharshan and Swetha, 2023; Khalid et al., 2024). The sensor's dependence on the Beer-lambert laws provides a robust framework for quantitative analysis, which makes them indispensable in industrial quality control and research applications (González-Morales et al., 2020; Sudharshan and Swetha, 2023; Qi et al., 2024). For industrial applications, UV-Vis Analysers are found to be an effective on-line replacement for biochemical oxygen demand analysers as they utilise wetchemical procedures for determining the levels of organic material in wastewater,

which is known to produce further chemical wastes (Van Den Broeke et al., 2006; Liauw et al., 2010; Kirsanov et al., 2017).

Despite the widespread use of UV-Vis spectroscopy, they possess certain limitations. A primary challenge of the technology is their selectivity, where chemical compounds with similar chromophores can have overlapping absorption bands, which can lead to ambiguous results, especially from interfering substances. In addition, UV-Vis spectroscopy is unable to deal with concentrations outside the Beer-Lambert Range. Furthermore, due to the working principle of UV-Vis spectroscopy, turbidity can cause light to scatter and have increased absorption, which can lead to erroneous results (Moonen and Diederich, 2004; Mäntele and Deniz, 2017; Qi et al., 2024).

In the recent years, significant studies and advancements have been made in UV-Vis spectroscopy technologies including the miniaturisation of the device (Pena-Pereira et al., 2011), enhanced data processing techniques (Y. Guo et al., 2020) and an improved prediction model (Guan et al., 2024) to improve the its overall functionality and reducing noise interferences.

2.1.2 Electrochemical Sensors (Potentiometric & Amperometric)

The intoxicating agent ethanol is found in beers and wines is one of the main compounds that Electrochemical (EC) sensors detect; hence, they are commonly used in breath analysers. They can also detect industrial chemical compounds such as formaldehyde, carbon monoxide, ammonia and ethylene. EC sensors usually come in two distinct types, which are either classified as amperometric or potentiometric due to the difference in their sensing principle.

The structures of EC potentiometric sensors are simple, which makes the fabrication process guite efficient. For a traditional configuration, the EC potentiometric sensors are mainly membrane-based devices constructed with two electrodes and an electrolyte where the activities occur. One of the electrodes plays the role of the reference electrode, which is submerged in the electrolyte containing the ions of interest at constant activity. The constant activity is due to the redox reaction between the VOC analyte and the reference electrode, which allows a fixed potential to be set at the reference electrode. The other electrode is an ion-selective electrode that will be subjected to perturbations by the surrounding medium. The ion-selective electrodes are typically membrane-based devices which separate the analyte from the inside of the electrode. When the molecules of the VOC analyte pass through the membrane and interact with the indicator electrode, a potential will be set at the ion-selective electrode according to the concentration of the VOC analyte in the sensing environment. With no current flow, the potential difference between the reference and ion-selective electrodes can be measured with a high impedance. As the reference electrode is constant with a fixed potential, the dissolved ion of interest can be related to concentration, which can then be used to obtain the concentration of the VOC analyte in the ambient environment (Stradiotto et al., 2003; Berkel and Özbek, 2024; Toala et al., 2024).

EC amperometric sensors are also mainly membrane-based, but their sensing principle differs entirely from the EC potentiometric sensors, which measure the potential difference with no current flow. Instead, EC amperometric sensors apply a fixed potential to measure the current response. The structure of the EC amperometric sensor is also quite different, as it constructs a potentiostat

connected to three electrodes submerged in an electrolyte. An electrochemical reaction occurs when the specific VOC analyte molecules diffuse through the sensor's membrane towards the working electrode's surface. Depending on whether the VOC analyte is reduced or oxidised in the reaction, electrons would be consumed or released, and as a result, an electric current would be generated. The electric current generated from the redox reaction is proportional to the concentration of the VOC analyte in the environment. The counter electrode balances the reaction at the working electrode, and the electrolyte transports the ionic current. The third electrode takes the role of the reference electrode, which is used to measure the potential of the working electrode (Stradiotto et al., 2003; W.-S. Wang et al., 2010; Szulczyński and Gębicki, 2017; Baracu and Gugoasa, 2021).

In both amperometric and potentiometric EC sensors, the measurement process depends on a reduction or oxidation reaction. Therefore, it should be noted that there is a significant limitation in terms of the EC sensor's selectivity, as not all VOCs are electrochemically active. Furthermore, there are also restrictions on the selection of the dopant for the ion-selective electrode (Stradiotto et al., 2003). EC Potentiometric sensors have been widely used for decades due to their simplicity, rapidity, non-destructive characteristics, and incredibly high selectivity towards hydrogen ions.

In the past, potentiometric sensors have been more widely used, but with the increased amount of research towards the EC amperometric sensors. The potentiometric sensors are found to be less sensitive and slower when put in comparison (J. Wang et al., 1995; Stradiotto et al., 2003). In recent years, there

has been increased research towards developing ion-selective electrodes to enable the monitoring of selective chemicals and significant miniaturisation of the system for wearable technologies (Baracu and Gugoasa, 2021; Pietrzak and Wardak, 2021; Yeung et al., 2021; Morawska and Wardak, 2024; Singh et al., 2024; Ameen et al., 2025).

2.1.3 High Performance Liquid Chromatography

High-performance liquid chromatography (HPLC) is a powerful analytical tool for separating, identifying and quantifying the individual components within a mixture of compounds (BASHARAT et al., 2021; A. H. Ali, 2022). It is commonly used along with UV-Vis, fluorescence and mass spectrometry to provide a more comprehensive analysis (Lindon et al., 2021; Thomas et al., 2022). The technique meets many analytical criteria, such as accurately producing reproducible quantitative data with high sensitivity and selectivity (A. H. Ali, 2022). Hence, it is widely applied in various industries, including pharmaceuticals, environmental, polymer manufacturing and food industries (Kazakevich and Lobrutto, 2006; Snyder et al., 2011; A. H. Ali, 2022).

The technique requires a small sample to be injected into a moving stream of liquid, known as the mobile phase, through a column packed with stationary phase particles. The mixture of compounds would then exhibit varying degrees of retention, allowing each separate component to be analysed (A. H. Ali, 2022; Patil et al., 2023).

Despite being such a strong analytic technique, several drawbacks restrict its application. Due to the nature of HPLC's working principle, the analysis is

relatively time-consuming with high solvent consumption, which makes it inefficient and, most importantly, incapable of real-time and continuous monitoring (Dong, 2013; Al-Sanea and Gamal, 2022; Pal et al., 2024). In addition, a controlled laboratory environment is required to control temperature and humidity, as these can affect the mixture's retention time and separation quality (Snyder et al., 2011; A. H. Ali, 2022).

Nevertheless, HPLC is one of the foundation analytical tools for liquid chemical detection, which can resolve highly complex mixtures. The robust methodology and precision it provides make it a golden standard for laboratory-based chemical sensing. Recent research on the technique has attempted to utilise thin-layer chromatography to allow reduced sample requirement, greater efficiency, and simultaneous analysis of mixtures. In an attempt to reduce HPLC's drawbacks, further developments towards a new approach offer enhanced capabilities such as efficiency, speed and resolution (Gope et al., 2024; F. Guo et al., 2024; Papp et al., 2024).

2.1.4 Optical Fibre Sensors

Optical fibre sensors over the last decade have emerged as a highly promising platform for chemical monitoring, particularly for applications that require real-time continuous and in-situ capabilities (Khonina et al., 2023; Acharya and Kogure, 2024; Wu et al., 2025). These sensors detect variations in the ambient environment based on the changes in light parameters. Optical fibre sensors can be classified as intrinsic or extrinsic depending on their application (Ochoa et al., 2021; Zhu et al., 2023). Intrinsically, optical fibres can be used to measure strain, temperature, pressure, intensity, phase and wavelength (Anjana et al., 2024; T.

Liu et al., 2024; X. Wang et al., 2024; Anjana et al., 2025; H. Wang et al., 2025). For extrinsic sensor devices, optical fibre will only be utilised as a carrier of the data that relays information from the sensing element outside the optical fibre (Gómez-Galdós et al., 2025). The classification of optical fibre sensors can also be further broken down into phase or intensity-modulated sensors. Phase-modulated sensors tend to be an interferometer that provides measurements based on phase shifts, whereas intensity-modulated sensors provide measurements based on loss in intensity or interactions with the evanescent wave (M. Li et al., 2021; Teng et al., 2021).

Many proposed optical sensing devices were still in the research phase around the 1990s (Eguchi, 1992). However, with the increased commercialization of optical fibres, optical waveguides and other optical components, there has been an increase in popularity towards optical methodologies for various detection systems (Khijwania et al., 2005; Alam et al., 2017; Elsherif et al., 2022; Anjana et al., 2024). In addition, with the vast variations and modifications that can be applied to optical fibre sensors, they have been extensively researched for chemical, biological and physical sensing applications (Johny et al., 2021; Ochoa et al., 2021; Abeywardena et al., 2024; Whittaker et al., 2025). Furthermore, several unique properties and characteristics of optical fibre grants them a high affinity towards sensor applications (Eguchi, 1992; Willsch and Bosselmann, 2002; B. Lee, 2003; Villatoro et al., 2005; Szulczyński and Gębicki, 2017; Kohli et al., 2025).

Whether the optical fibres are applied intrinsically or extrinsically for sensor applications, the optical fibres that detect and carry the information through light

rays are immune to electromagnetic interferences. Therefore, unlike the typical electronic devices that may break and cease to work, external electromagnetic disturbances will not degrade the performance of these optical fibre devices. They also do not require any electrical contact or current flow to function as a means of detection (Eguchi, 1992; Fu et al., 2024; Karimian et al., 2025; Kohli et al., 2025; Yu et al., 2025).

As optical fibres do not carry high voltage like copper wires, they are safer for use in hazardous and explosive environments. optical fibres can cause ignition if the light beam is leaked and strong enough to ignite the explosive gas. However, this can be controlled by controlling the intensity and wavelength of the laser beam travelling down the fibre (Willsch and Bosselmann, 2002; Villatoro et al., 2005; Zhou et al., 2015; De Waele et al., 2025).

optical fibres can be fabricated into very small dimensions while still maintaining their robustness allowing their portability in sensor applications (B. Lee, 2003; Szulczyński and Gębicki, 2017; Chapalo et al., 2024; C. Li et al., 2024). This allows them to be used for detection in normally inaccessible areas without affecting the signal's performance.

Optical fibres are chemically unreactive, which allows them to be applied in chemical and biomedical environments (Zubair et al., 2023; Sundari and Edayadulla, 2024; Whittaker et al., 2025). They are also resistant to high temperatures, allowing them to be subjected to a range of harsh environments (Deng and Jiang, 2022; Ma et al., 2022). Furthermore, optical fibres have a large bandwidth, allowing several individual detection points of a terrain can be

multiplexed into a fibre cable, which offers the potential for multiple simultaneous and continuous detection of analytes (B. Lee, 2003; Anjana et al., 2024).

2.2 Optical Fibre Sensing Principles and Configurations

Optical fibres are cylindrical dielectric waveguides that confine and transmit light through the principle of total internal reflection. This section will explore the fundamentals of optical fibres, the principles that enable their sensing capabilities, and configurations that can enhance their overall performance.

2.2.1 Optical fibre Structures

Optical fibre cables can be considered photon conductors composed of transparent materials such as glass and plastics. Almost all optical fibre cables share the same fundamental structure, as shown in Figure 1.

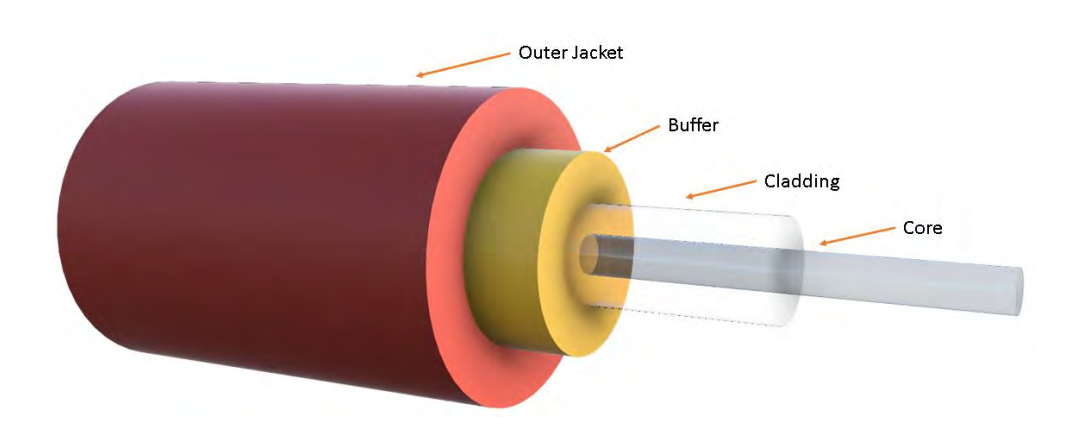


Figure 1 Typical structure of an optic fibre

Located at the centre axis of the optical fibre is the core, which has a higher RI than the cladding that surrounds the core (Selvarajan et al., 2003; Marcuse, 2012). The buffer between the cladding and the jacket provides mechanical isolation, usually containing a lubricant to prevent abrasions. The outer jacket is

typically made from a polymer possessing several attributes, including flexibility, static fatigue, abrasion resistance, moisture resistance, and the ability to be stripped. Depending on the jacket's material, it may also allow operations up to 500°C for long durations or even 700°C for shorter durations (Al-Azzawi, 2017). The jacket will prevent cracks from opening on the fibre's surface which can cause a loss of tensile strength (Marcuse, 2012). The typical dimensions of the optical fibre cable are:

	Typical Dimensions (µm)	
	Core	Cladding
Fibre Type 1 (Single-mode)	9	125
Fibre Type 2 (Multimode)	50	125
Fibre Type 3 (Multimode)	62.5	125
Fibre Type 4 (Multimode)	100	140

Table 1 Typical core and cladding dimensions of single-mode and multimode fibres

There are two types of classification of fibres based on the refractive index profile of the core, step index and graded index optical fibre. Their relative refractive index profiles can be seen in Figure 2.

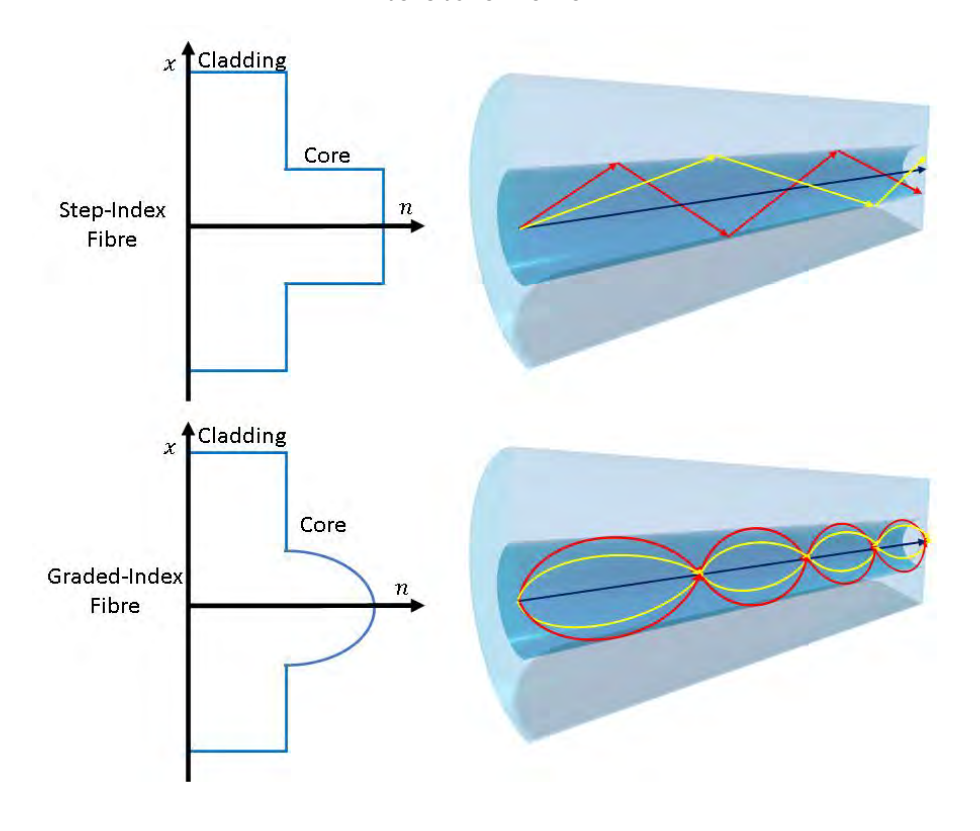


Figure 2 Refractive index profile of step-index and graded-index fibres

In step-index fibres, the refractive index of the core is unchanged throughout the core diameter, but at the core-cladding boundary, there is a sudden change in the RI. However, for graded index fibres, the maximum refractive index at the centre of the core varies as it moves closer towards the cladding. The types of fibres can also be further broken down into single-mode or multimode depending on the number of modes the fibre carries (Selvarajan et al., 2003).

2.2.2 Operating Principles

All optical fibres function with the concept of total internal reflection, where the light source is transmitted down an optical fibre by repeating reflections between the core and cladding interface. For angles of incidence less than the critical angle, refraction occurs, and for angles of incidence greater than the critical angle, total internal reflection occurs. However, for light reflecting near the critical angle at the core region of an optical fibre, a significant proportion of the light's power

extends into the cladding region. This phenomenon is known as the evanescent wave which is what most optical fibre sensors utilise for gas detection (Safira, 2025). The evanescent wave intensity decays exponentially with distance; hence, it only extends to a very short distance from the interface (Ligler and Taitt, 2011; Adam and Zhang, 2014; You et al., 2024).

In some practical sensing applications, a section of the cladding is removed, modified or etched to allow the evanescent field to extend beyond the fibre core into the external environment. The cladding of the optical fibre normally confines the propagating light within the core of the fibre, preventing any significant interactions with the external environment. By partially thinning or modifying an area of the cladding, the confinement of the guided modes decreases, allowing the modal field to expand beyond the core-cladding boundary. The expansion increases the fraction of optical power residing in the evanescent field and results in stronger interactions with the external environment (Memon et al., 2022; Wójcik and Przystalka, 2022). Most optical fibre sensors utilise this phenomenon to allow the interaction of the evanescent wave with the surrounding medium, causing an absorption to occur. The amount of absorptions the evanescent wave experiences can be related to the concentration of the targeted chemical species (M. Butt et al., 2017; You et al., 2024; Meng et al., 2025).

2.2.2.1 Evanescent Wave Theory

When the angle of incidence is smaller than the critical angle, some of the incident wave is transmitted into the cladding medium, and some are reflected back into the core, as shown in Figure 3.

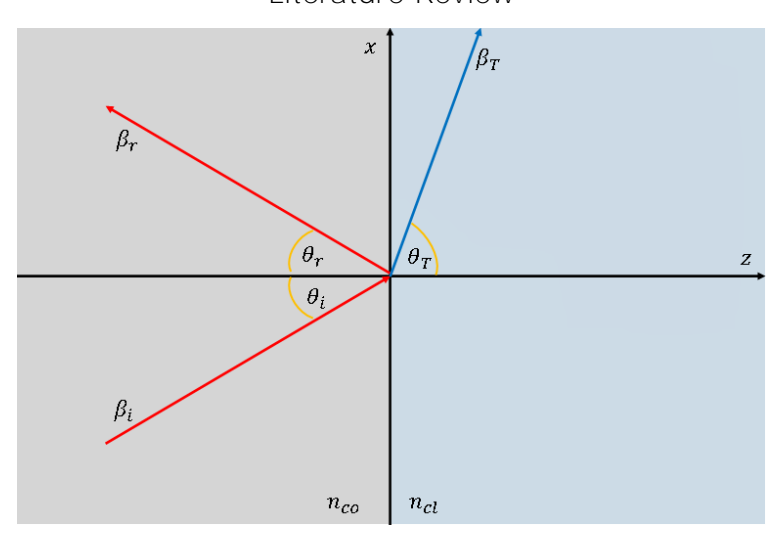


Figure 3 Diagram showing the reflection and refraction which occurs at the core-cladding interface when the angle of incidence is smaller than the critical angle.

When light propagates through an optical fibre via total internal reflection, the electromagnetic waves do not disappear at the core-cladding interface. Each total internal reflection event along the fibre generates an evanescent wave where a small portion of the guided optical field penetrates the core-cladding interface.

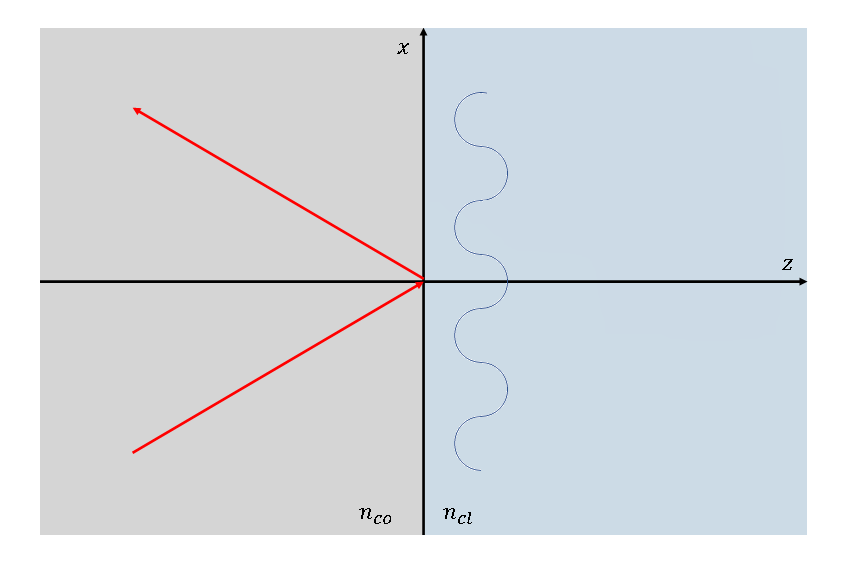


Figure 4 Diagram showing an induced evanescent wave due to a totally internally reflected light ray.

This decaying electric field is what is known as the evanescent wave where the energy is concentrated at the core-cladding interface and does not propagate. As the evanescent wave is oscillating continuously, there is no net energy flow over a complete cycle of oscillation.

2.2.2.2 Evanescent Wave Parameters

There are various parameters that govern the evanescent wave phenomenon, evanescent power and penetration depth are two important parameters that needs to be considered for evanescent wave-based sensors (Punjabi et al., 2015).

Penetration Depth

The penetration depth of the evanescent field is the distance in which the amplitude of the electric field at the core-cladding interface decays to 1/e (36.8%) of its original value (Mirchin et al., 2013; Punjabi et al., 2015; Götz et al., 2020). The penetration depth can be described by equation 2.

$$d_p = \frac{\lambda}{2\pi n_{co} \sqrt{\sin^2 \theta_i - \left(\frac{n_{cl}}{n_{co}}\right)^2}}$$
 (2)

Evanescent power

The amount of power due to the evanescent field can be approximated by calculating the power present in the claddings of a multimode fibre (Equation 3).

$$\frac{P_{cl}}{P_T} = \frac{4}{3\sqrt{M}} = \frac{4\sqrt{2}}{3V} = \frac{4\sqrt{2}}{3} \frac{\lambda}{2\pi r \sqrt{n_{co}^2 - n_{cl}^2}}$$
(3)

Where P_{cl} represents optical power in the fibre cladding, P_T is the total optical power in both core and cladding, M is the number of modes and V representing the V-number. It is clear that with an increase in V-number, there will be a reduced fractional of power found in the

cladding of the fibre. This makes the V-number selection a very important aspect in determining the evanescent power of a fibre optic sensor.

2.2.3 Long Period Fibre Gratings

Traditionally, the cladding regions will be stripped off or sanded down to allow the interactions of the evanescent wave. However, LPFG provides one solution for interactions to occur between the surrounding medium and the propagating light in the core through the cladding modes without any alterations to the mechanical properties of the optical fibre cable. No etching would be required to remove the cladding as the gratings itself will permit the coupling of light in the core into several discrete wavelengths co-propagating in the cladding region, forming cladding modes.

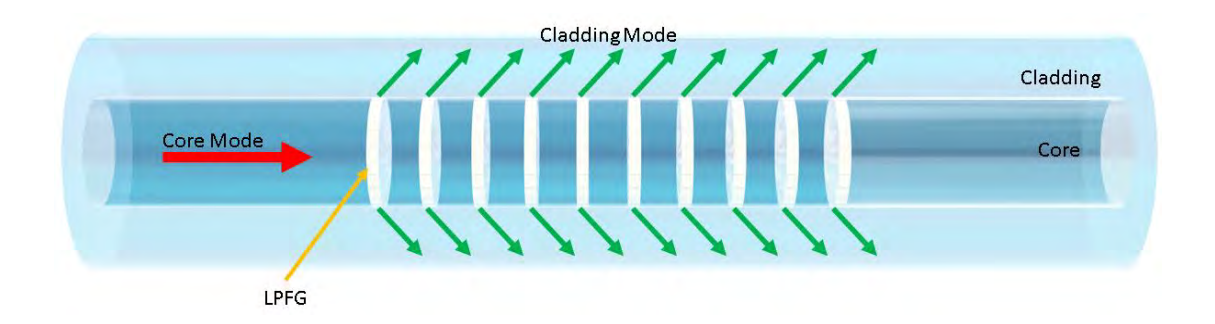


Figure 5 Mode conversion from the fundamental core mode into a forward propagating cladding mode in an LPFG

The coupling of the core mode into cladding modes is dependent on the phase-matching condition:

$$\beta_{01} - \beta_{cl}^m = \frac{2\pi}{\Lambda}, m = 2,3,4 \dots$$
 (4)

Where β_{01} is the propagation constant of the fundamental mode, β_{cl}^m is the propagation constant of the m^{th} co-propagating cladding mode and Λ is the grating period of the LPFG.

Due to the high attenuation of the cladding modes, distinct attenuation bands can be observed to be centred at discrete resonant wavelengths in the transmission spectrum. These resonant wavelengths can be described by the following equation:

$$\lambda_{res,m} = \left(n_{co}^{eff} - n_{cl,m}^{eff}\right)\Lambda \tag{5}$$

Where $\lambda_{res,m}$ represents the m^{th} order resonance wavelength, n_{co}^{eff} is the effective refractive index of the core, $n_{cl,m}^{eff}$ is the effective refractive index of the m^{th} cladding mode. The wavelength of $\lambda_{res,m}$ is dependent on the $n_{cl,m}^{eff}$ which is also further dependent on the refractive index of the ambient environment. When the LPFG is subjected to an ambient environment with a refractive index not exceeding that of the cladding, then according to equation 5 the effective RI of the cladding will be increased whilst the core's effective RI remains the same. Such an environment will cause a shift of the $\lambda_{res,m}$ corresponding to the surrounding RI. On the other hand, if the RI of the surrounding medium possesses a RI higher than that of the cladding, the phase matching condition, as shown in equation 4, will no longer be satisfied. As a result, there will be a loss of the total internal reflection of the light guided by the cladding of LPFG. This behaviour the LPFG exhibits is known to be called radiation modes/leaky cladding modes which will be simulated in Chapter 4 for analysis and comparison (Chen and Gu, 2012; Tan et al., 2014a; Tan et al., 2015).

2.3 Carbon Nanomaterial Integrated Optical Fibre Sensors

Since the discovery of carbon nanomaterials by Sumio Iijima in 1991, there has been an emerging amount of published papers on carbon nanomaterials as they have emerged as highly effective components that have become crucial in various sensing applications. From the explored search term "carbon nanotube" between the years 2000 and 2010, there was a total of 52,224 articles containing the CNT concept and 5,746 patents (Golnabi, 2012). Between the years 2010 and 2020, a search of the term " carbon nanotube" on Google Scholar has identified approximately 387,000 articles, which signifies the amount of research attention that has grown. In the more recent years, carbon nanotube integrated optical fibre sensors have persistently attracted a considerable amount of scientific interest that is reflected by the consistent volume of research output. The Google Scholar search term results for "Carbon nanotubes optical fibre sensors" have approximated 7,700 articles published in the year 2022, followed by 7,770 articles in 2023 and 7,980 articles in 2024. From alternative databases such as the Web Of Science, and semantic scholar, the same search term has identified similar publication consistency each year between 2022 to 2024. The sustained publication activity highlights the ongoing relevance and broadening of the material's applicability across optical fibre sensors.

Carbon nanomaterials exhibit great potential in chemical sensing applications, primarily due to their low-dimensional carbon structures that expose most of their atoms to the surrounding environment, offering a high surface-to-area ratio that maximises interactions and thus enhances sensitivity. Their excellent electrical conductivity, electron mobility and tuneable bandgaps enable rapid and precise

responses to changes in the surrounding environment, making them ideal for real-time monitoring. Carbon nanomaterials can be functionalized with various chemical groups to improve selectivity (Pajuelo-Corral et al., 2022). Additionally, carbon nanomaterials are known for their chemical, and thermal stability, allowing for continuous sensing applications without significant performance degradation over extended period of time (Ayanda et al., 2024; Luo et al., 2024; Paramasivam et al., 2024).

The advantageous properties of these carbon nanomaterials have inspired a growing interest in their integration into optical fibre sensor platforms. Novel concepts of carbon nanomaterial integrated sensors have been proposed, and various approaches are being investigated to achieve a simple, sensitive and stable device for a broad spectrum of applications (Abdel-Karim, 2024; S. Kim et al., 2024; Rao et al., 2024). Amongst the various forms of carbon structure, graphene and carbon nanotubes are most commonly researched with optical fibre sensors. This is due to their widespread study over the past two decades which has led to a stronger understanding of their properties and practical integration methods (Hejazi et al., 2023; Goodrum et al., 2024; Luo et al., 2024). In recent years, the focus of the research has been directed to enhancing the sensing performance by incorporating these carbon nanomaterials on speciality fibre sensing systems such as Mach–Zehnder interferometers (MZIs), fibre Bragg gratings (FBGs), and LPFGs.

When carbon nanomaterials are applied to optical fibre sensors as a coating, they fundamentally change the way light propagates within the fibre. The higher RI of the material modifies the optical boundaries between the cladding and the

external environment, allowing a large portion of the guided light to induce an evanescent field that extends beyond the surface of the fibre. This enhanced evanescent field interaction allows optical fibre sensors to gain increased sensitivity to external RI changes. Chapter 4.2 expands further on the explanation of carbon nanomaterials affect optical fibre sensors. Ultimately, the carbon nanomaterial layer acts as an evanescent field enhancer that can be chemically functionalised for selective absorption of materials. The optical and chemical aspects that the carbon nanomaterial layer plays make them effective for RI and chemical detection.

2.3.1 Graphene

In the recent years, graphene, has attracted a significant amount of scientific interest for the fabrication of sensors incorporated with nanomaterials (Justino et al., 2017). Graphene is a single sheet of sp^2 hybridised carbon atoms arranged in a honeycomb lattice. What gives the materials such strength is the σ C=C bond, which is one of the strongest bonds in materials with a breaking strength of 42 Nm^{-1} of a defect-free sheet (C. Lee et al., 2008). The weak interactions from the π bonds hold the monolayer graphene sheets together in graphite, allowing the layers to slide over each other. Also, the weak bonds are the main reason that makes it challenging to separate graphite into its individual layers. However, physicists have now managed to mechanically cleave out the graphene sheets and isolate the single layer from graphite (D. Li and Kaner, 2008) and synthesizing high quality graphene through chemical vapour deposition (CVD) is now possible. Although the monolayer of carbon atoms is the thinnest known material, it is also the strongest material ever measured while having transparent,

flexible and conductive properties (Bollella et al., 2017). However, for sensing applications, the most notable feature of graphene is the structure of the material. As it is a strictly two-dimensional material, all of the carbon atoms in a single layer of graphene sheet/film are exposed to the environment, which maximises the surface-to-area ratio. Another property of graphene is its high electron mobility and high specific surface area accompanied by low electrical noise, which has contributed to the raised attention in sensing applications over the last few years (Demon et al., 2020). For optical fibre sensors, graphene is found to be highly compatible in forming thin films on the surfaces of the silica optical fibres. Furthermore, the monolayer graphene is highly flexible due to its single atom-thick structure, allowing it to seamlessly adapt to the curvature of optical fibres without detachment and structural degradation from mechanical stress (Tan et al., 2015).

2.3.1.1 Graphene Integrated Mach Zehnder Interferometer Sensors

A sensor developed based on the MZI detects chemical concentration variation by measuring the wavelength shift in the spectral fringe of the interference spectrum. In an MZI, light from the broadband source is split into two paths, one is the reference path and the other is a sensing path. The sensing path is exposed to the surrounding environment which affects the guided light whilst the reference path remains isolated from external conditions. Both paths are then recombined at an output coupler and thus generates interference fringes.

The condition for constructive or destructive interference is dependent on the phase difference.

$$\varphi = \frac{2\pi\Delta n_{eff}L}{\lambda} \tag{6}$$

Where φ represents the phase difference between the optical paths, Δn_{eff} the effective RI difference between the core and cladding, L the interferometer interaction length and λ the wavelength of the light from the broadband.

Destructive interference occurs when the phase difference satisfies the equation:

$$\varphi_m = (2m+1)\pi \tag{7}$$

Thus the mth-order interference valley λ_m can be expressed by

$$\lambda_m = \frac{2\Delta n_{eff} L}{\lambda} \tag{8}$$

As the wavelength of the mth- order interference valley will be changing with the external RI, the effective RI changes causing an observed wavelength shift in the interference pattern (Q. Wang et al., 2016; Ahsani et al., 2019; Xia and Zhao, 2020). Thus the amount of wavelength shift of the mth-order interference valley $\Delta\lambda_m$ can be represented by:

$$\Delta \lambda_m = \frac{2\Delta n_{eff} L}{2m+1} \tag{9}$$

The changes in the interference patterns indicates the variations in the environment which can enable precise sensing of physical and chemical conditions..

In a 2016 paper, a pilot demonstration of a graphene overlayed photonic crystal fibre (PCF) for RI sensing applications was presented (Q. Wang et al., 2016). In the study, a PCF is spliced in between two single-mode fibres (SMFs) to form a PCF-MZI and the sensing element is formed with the deposition of graphene that overlays the PCF. The integration of the graphene overlay on the PCF Mach-Zehnder Interferometer sensing scheme has shown a 16.3% increase in sensitivity between the sensing range of 1.3333-1.3737RI.

For the detection of a specific chemical, ammonia, a study on an all-optical interferometric sensor was proposed and developed entirely based on graphene and a microfibre hybrid waveguide. The overlay of graphene has allowed a highly sensitive detection of the change in ammonia concentration with a resolution up to 0.3 ppm achieved. With adjustments to the length and area of the graphene on the microfibre, the sensitivity can be further tuned. The proposed sensor device demonstrated high sensitivity with fast response, and the resolution was mainly limited due to the limitations of the optical spectrum analyser (Yao et al., 2014). Similarly, in another paper, a graphene coated MZI device was proposed for the detection of ammonia and a wavelength shift sensitivity of 3pm/ppm was achieved over a linear range of 10-180ppm. (Hao and Chiang, 2017). The sensor's performance can also be improved by adjusting the thickness and length of the coating around the optical fibre.

Graphene oxide (GO) is a carbon nanomaterial that is further derived down from graphene and remains to inherit excellent properties. Graphene oxide can be produced in a more cost-effective process and shows greater potential for large scale production of Graphene-based functional groups compared to Graphene. The various functional groups applied to Graphene such as hydroxyl, carboxyl, carbonyl, epoxy etc. allow for selectivity in the gas sensor. A recent study utilised a GO coated substrate composed of a single-mode fibre, photonic crystal and another single-mode forming a MZI for ammonia sensing has shown remarkable response and recovery times with good selectivity and wavelength shift sensitivities (Fenjan et al., 2023). In another prior research, a Graphene Oxide coated MZI ammonia sensor formed from two MMF and a thin core fibre was found to exhibit a high wavelength shift sensitivity of 4.97pm/pmm which is higher than the previously mentioned graphene coated MZI gas sensors (Fan et al., 2021).

2.3.1.2 Graphene Integrated Fibre Bragg Grating Sensors

FBGs are the inscription of a refractive index modulation of the core in the optical fibre. As a result, coupling occurs between the propagating and counter propagating core mode which forms a spectral peak present in the reflection spectrum. The detection of concentration variation of a gas can be derived from the amount of wavelength shift in the reflected spectrum. In the past, FBGs based sensors have demonstrated a wide range of applications in the literature for several physical parameters which include temperature, strain, pressure, bending and refractive index detection. In the last few years, the research lines of FBGs in optical fibre sensors have progressed towards a new route where coatings and

thin films are being applied to enhance their sensitivity and enable selective chemical detection.

In a study, a GO coated FBG sensor was proposed for the detection of ethanol in petrol. The sensor has been reported to be able to detect ethanol proportions within petrol down to a minimum concentration of 0.5%, which is 10 times lower than the concentration detected by an uncoated FBG (P. Kumar et al., 2019). In a more recent study, a TiO₂ functionalized reduced graphene oxide (rGO) coated on an etched FBG based sensor was proposed for the detection of ethanol (Shadab and Raghuwanshi, 2022). The proposed device was found to be better than a bare FBG based sensor and a TiO₂ Coated FBG sensor with final wavelength shift sensitivities of 5.91nm/RIU in petrol.

For the detection of nitrogen dioxide NO₂, another FBG sensor was proposed with the integration of a rGO coating. The detection mechanism is based on changes in the Bragg wavelength caused by the effective refractive index variation of the rGO coating induced by the adsorption of the NO₂ molecules at the surface of the rGO coating. The device was able to detect NO₂ down to a lower limit of 0.5ppm with a high sensitivity of 0.8pm/min (Sridevi et al., 2016).

2.3.2 Carbon Nanotubes

Aside from Graphene, there have been other carbon-based nanomaterials that have shown promising results; these include single-walled carbon nanotubes (SWCNTs), double-walled carbon nanotubes (DWCNT) and multi-walled carbon nanotubes (MWCNTs). The SWCNTs were initially discovered by Lijima and Ichihashi, where they revealed and discussed the synthesis of SWCNTs with a

diameter of 1 nm diameter (Iijima and Ichihashi, 1993). SWCNTs can be fabricated to have dimensions around 1-2nm in diameters at various lengths. The DWCNTs are structured as two concentric carbon nanotubes with the inner tube enclosed by the outer tube. Finally, the MWCNTs are structured encased with multiple layers of CNTs, with a diameter range between 2nm to 50nm depending on the number of layers/tubes it encloses. Between each layer of the tubes, the approximate distance is estimated to be about 0.34nm (Ibrahim, 2013). Since the discovery of SWCNTs, various research has been conducted on its properties, such as depending on the structure of the tubule, the diameter and the degree of helical arrangement, it would exhibit variations of properties (Hamada et al., 1992). In addition, there are studies revolving around the sensitivity of the absorption peaks with predictions that the decreasing diameters of SWCNTs, would shift the absorption peaks towards the higher energy side of the spectrum (Kataura et al., 1999)

Similar to the other variations of carbon nanomaterials, CNTs are found to be highly compatible with silica as the CNTs can form thin films on the surfaces of silica which is important for optical fibre sensors (Ferrier and Honeychurch, 2021; Nor et al., 2023; Mohan and Negi, 2024). For chemical sensing, they have been found to be coated on photonic crystal fibres, LPFG and FBG to enhance the interactions with the ambient environment due to the CNT's unique absorption characteristics.

Currently, chemical vapour deposition (CVD) is regarded as the most promising technique for the direct growth and deposition of CNTs onto a substrate (Pant et al., 2021). However, the CVD technique is known to consume too much

precursors in the process and requires a high temperature environment between 700-1000°C (X. Liu, 2006; Shoukat and Khan, 2021). Thus, a low-cost, large scale deposition of CNTs remains challenging (L. Wang et al., 2025). The challenges become more apparent on platforms such as optical fibres which will be discussed further in Chapter 3.

2.3.2.1 Carbon Nanotube Integrated Mach Zehnder Interferometer Sensors

A significant amount of literature has been found on a graphene MZI sensors as discussed in chapter 2.3.1.1, but MZI sensors integrated with CNTs are still in the early stages of research. In an earlier paper, a MZI configuration based optical setup was proposed with the integration of CNTs for refractive index detection. The proposed sensing element of the device consists of a short length of PCF sandwiched between two single-mode fibres forming the MZI configurations. A thin layer of CNT is deposited around the photonic crystal fibre region. The experimentation of the sensing element displayed distinct intensity changes with little wavelength shifts across different refractive indexes of solutions between 1.33-1.42RI. The setup allowed the device to obtain continuous measurements and gain immunity from the free spectral range limitations (Tan et al., 2014b). A more recent paper, proposed an SWCNT integrated MZI sensor for the selective detection of ammonia. The MZI was formed in this design by fusion splicing a small section of thin-core fibre between two SMFs. At an ammonia exposure with concentrations between 1 to 960ppm, the experimental results show an approximately linear relationship in the range of 1-20ppm, which can be a monitoring low concentration potential application for ammonia gas environments (Huang et al., 2017).

2.3.2.2 Carbon Nanotube Coated Fibre Bragg Grating Sensors

Similarly to Graphene integrated FBG sensors, the literature on CNT-FBG sensors is limited. A primary research focus in the recent years for FBG sensors was based around the detection of temperature, strain and stress rather than aqueous chemicals. Therefore, the integration of a CNT layer that can provide functionalisation may not be of use in such scenarios (Alhussein et al., 2025; Lv et al., 2025; D. Sun et al., 2025; S. Sun et al., 2025). However, a variety of sensors proposed and developed for the detection of various chemical parameter have been proposed and developed over the years. A CNT coated FBG sensor was proposed for the detection of a broad range of relative humidity (RH). The high surface-to-volume ratio of the CNT coating allowed high adsorption of water molecules and provided the FBG sensor with a detectable range of RH between 20-90% with a sensitivity of approximately 31pm/%RH, which is found to be much higher than existing bare FBG based humidity sensors (B. N. Shivananju et al., 2014).

In another study, a different variation of FBG sensors was also integrated with CNTs (C. Liu et al., 2016). The CNTs were deposited on the tilted fibre Bragg grating (TFBG) region of the sensor to investigate both refractive index and temperature sensing measurements from the ambient environment. In the field of biochemical industries, and environmental monitoring, the measurements of these two variables are indispensable processes hence in this particular sensor it was ideal to simultaneously measure both variables. With the deposition of CNTs on the region of the TFBG, the sensing range of the TBFG is found to have extended seven times the original and has enhanced the sensitivity towards the

low refractive index regions. From a different paper, a similar CNT-TFBG design was proposed showing agreement with the increase in sensitivity (Jiang et al., 2016).

For targeted chemical detection, a selective CNT-FBG was proposed and investigated for the detection of CO₂ at room temperature. In order to measure the CO₂, the CNT coating of the CNT-FBG incorporated a functionalisation group. The functionalised CNT-FBG sensor shows improved sensitivity and the ability to discriminate target gas amongst various gases (B. Shivananju et al., 2013).

2.3.2.3 Carbon Nanotube Coated Long Period Fibre Grating Sensors

As discussed in Chapter 2.2.3, LPFGs provide a solution for maintaining the fibre's mechanical strength whilst providing interactions between the propagating light in the fibre and the outside medium. A study has proposed a design for RI where CNTs are deposited around the exposed LPFG cladding region of the fibre (Tan et al., 2015). The design can allow for a mechanically robust fabrication of an RI sensor that requires no fibre tapering or etching with continuous monitoring capabilities. The sensor was found to exhibit a sensitivity of 31dB/RIU between the an RI range of 1.33-1.38RI.

In a layer-by-layer assembly of polyelectrolytes-wrapped MWCNT on an LPFG sensor, the response has shown pure intensity modulation without wavelength shifts between 1.3488-1.4337RI with a high RI sensitivity of 85dB/RIU (Ni et al., 2019). However, a downside in the sensor design lies in the layer-by-layer process which requires long duration with careful control during the dip coating. The coating methodology can introduce defects, limited uniformity and manufacturing throughput at larger scales of fabrication.

2.3.3 Summary

Both CNTs and graphene have been extensively researched, they offer their each and own unique advantages in terms of sensitivity, durability and functionalisation which are critical for high-performance sensing applications. The choice between CNTs and graphene involves the consideration of various factors, including their ease of integration, physical and chemical properties which contributes to the overall performance of the sensor.

While graphene has a high surface area, it remains as a two-dimensional structure which cannot be comparable to the level of interactions with analytes from CNTs. Both materials can be functionalized covalently and non-covalently to enhance sensitivity and selectivity. Functionalisation processes of CNTs are typically more straightforward in comparison to graphene functionalisation. Graphene is a two-dimensional structure with a single atomic layer which can make functionalisation more challenging without degrading its properties. Furthermore, due to the nature of graphene there are minimal structural modifications that can be applied (Kuila et al., 2012). CNTs in contrast can offer adjustments to the diameter and length with chirality control (Tang et al., 2024). As a coating, graphene can allow greater uniformity than CNTs due to application of their single atomic layers but face challenges related to film continuity, layer control and defects that can impact senor performance.

The carbon nanomaterial coating plays an important role in enhancing the evanescent field interaction between the guided light and the surrounding medium arising from the contrast in the RI of the coating and the cladding of the fibre. The optical coupling induced by the carbon nanomaterials improves the

overall sensitivity. A detailed theoretical analysis of the enhanced interaction induced by the coating is presented in Chapter 4.2.

In summary, CNTs offer several advantages over graphene in sensitivity functionalisation and structural modifications for chemical sensing applications. There are difficulties in achieving efficient, effective and uniform coatings for optical fibre platforms.

2.4 Research Gap

Chemical sensors for liquids monitoring are crucial to detect and quantify chemical substances in various environments. These sensors are vital in industrial processes and safety, public safety, healthcare and environmental monitoring. Sensors with high sensitivity, real-time and continuous monitoring capabilities are highly sought after. Long-established platforms such as UV-Vis spectroscopy, EC analysers, and HPLCs have been widely adopted due to their accuracy and robust analytical capabilities. However, their ability to be utilised in a remote or in-situ environment with continuous monitoring is often restricted by operational constraints such as equipment maintenance, calibration and portability as well as the need to prepare samples for analysis.

In contrast, recent advancements in optical fibre sensing technologies have offered viable alternatives, particularly due to their small dimensions, ability to operate in harsh environments with distributed sensing capabilities and immunity to electromagnetic interferences. With the integration of carbon nanomaterials such as CNTs, the performance of optical fibre sensors has been further enhanced in terms of sensitivity and selectivity.

Research into carbon nanomaterial-based optical fibre sensors has expanded significantly, with various fibre structures and modifications such as FBGs, LPFGs and PCFs. Several studies have demonstrated the enhancements and functional benefits of these optical fibre set-ups for chemical monitoring applications with high sensitivity. However, much of this work is focused around complex fibre geometries, speciality fibres and speciality systems that hinders reproducibility, scalability and commercial translation. Furthermore, literature focusing on the use of standard single-mode fibres as a base platform remains limited despite their simplicity, cost-effectiveness and compatibility with existing fibre network infrastructures.

Carbon nanomaterial integrated optical fibre sensors have shown promising results and potential for chemical monitoring. However, several areas remain narrowly explored, features that have yet to be uncovered and critical gaps that persist in the field:

- The complexity and scalability of fabrication are primary issues, as most carbon nanomaterial integrated optical fibre sensors utilise speciality fibre designs and multi-stage coating processes that are not easily scalable. For example, the lack of a simplified and reproducible approach, such as using commercially available SMFs and simplistic coating methodology, limits their practical deployment.
- The trade-off between functionality and simplicity. There is a significant amount of literature in which a high-performance optical fibre sensor has been demonstrated using sophisticated systems.

However, limited research explores sensor designs that offer comparable sensitivity but with higher adaptability.

• Currently, a significant proportion of literature on optical fibre sensors are found to primarily be based on wavelength shifts in response to RI as their primary mechanism rather than intensity change. If the primary mechanism can function based on intensity change in response to RI, the requirement of a high-resolution optical spectrum analyser can be eliminated along with the need for advanced computational algorithms that are more suited for real-time applications.

This research aims to address the identified gaps by developing a chemical sensor based on the surface engineering of carbon nanotubes onto single-mode optical fibres. The use of SMF as the base platform will reduce fabrication complexity and allow for scalability. The integration of CNTs will enable intensity-based sensing, allowing the research to explore a cost-effective alternative to wavelength shift detections and opens the possibility of functionalisation for selectivity. In combination, this approach will pave the way for simultaneous, field-deployable sensors capable of real-time continuous in-site monitoring across various applications, from water quality analysis to environmental monitoring and industrial processes.

3 COATING METHODOLOGIES

The integration of CNTs onto optical fibres is a critical step in the development of a high-sensitivity chemical sensor. As discussed in the previous sections, CNTs offer several advantageous properties, but the literature surrounding their coating methodologies remains limited and fragmented. Few studies offer quantitative insight on how coating parameters can affect the optical response. This section discusses the commonly used CNT coating techniques and their applicability for optical fibres.

3.1 Chemical Vapour Deposition

CVD is a widely used method for synthesising CNTs. This methodology involves the decomposition of gaseous carbon sources at high temperatures in the presence of a catalyst to induce the growth of CNTs on a targeted platform (Dresselhaus and Avouris, 2001; Meyyappan, 2004; Mukul Kumar and Ando,

2010). It is generally found that low temperature CVD of about 600-900°C yields MWCNT, and higher temperatures of 900-1200°C favours the growth of SWCNT (Mukul Kumar and Ando, 2010). Due to the nature of CVD, high purity of CNTs can be grown with precise control over the CNT's parameters such as length, diameter and chirality.

Despite such outstanding advantages, due to the platform for the coating being an optical fibre, there are limitations and restrictions to utilising this technique. The primary restriction is the temperature requirement of CVD. Optical fibres are typically made from silica, which is sensitive to high temperatures, and exposure to CVD can cause structural damage and degradation of optical properties. Furthermore, with the low withstanding temperatures of the polymer jacket of the SMF-28, it will need to be removed prior CVD. Removing the jacket at lengths exceeding the coating region can lead to the bare optical fibre being highly susceptible to physical damage and temperature variations, thus reducing its operational lifespan. The jacket of the fibre is usually applied during the manufacturing process after the fibre is drawn from the preform. Postmanufacturing jacketing poses many challenges due to alignment of the fibre within the jacket, uniform application of the jacket, thermal effects from the curing process of the jacket and contamination of the fibre during its unjacketed durations can all cause damage and degradation to performance of the fibre. Furthermore, the CNT coating can also be damaged during the rejacketing process. Wafer structures are ideal due to their flat planar surface for the uniform deposition of thin films using CVD (Madou, 2011). On the other hand, fibres are cylindrical with curved surface, making uniform deposition more challenging compared to wafers (Wei, 1988).

To bypass the temperature issues faced by the optical fibre, CVD can be used to first deposit the CNT on a donor substrate first and then use wet/dry transfer techniques to migrate the CNTs to the optical fibre (Suk et al., 2011; Cole et al., 2012). However, these techniques will require highly precise transfer conditions to avoid damaging the film and have limited efficiencies in scalability for mass production.

CVD is undoubtedly an advanced technique for the synthesis of highly controlled parameters of CNTs but it has poor compatibility with optical fibres and poses many challenges that may require complex solutions to overcome.

3.2 Dip Coating

Traditional dip coating can be a very straightforward and cost-effective approach to coating optical fibres without any complex equipment. The process requires the immersion of the optical fibre in a prepared CNT suspension which is then withdrawn at a controlled speed before the drying the coated fibre (Spotnitz et al., 2004; Jang et al., 2008). Dip coatings typically require elevated drying temperatures using an oven to accelerate the drying durations down to 30minutes or it can take hours and overnight drying under room temperatures (Fang et al., 2019).

The thickness of the coating can somewhat be controlled by the speed of withdrawal. Faster speeds of withdrawal can allow for thinner coatings but can cause weak adhesion and incomplete coverage, whilst slower speeds can lead to thicker but uneven coatings. The layer-by-layer technique can be used to overcome inconsistencies for improved coverage of coating by first rinsing loosely

bound CNTs and then drying the coated fibre before the next coating application, creating a multilayer structure (Rivero et al., 2019).

3.3 Spray Coating

Spray Coating is another simplistic approach to coating optical fibres with very thin layers of CNTs. The process involves using a spray gun or airbrush to atomize a prepared CNT suspended solution into fine droplets to deposit onto the optical fibre and then dry (Kim et al., 2010; Kunaraj et al., 2023). The fine atomization of CNT suspension can allow even distribution of CNTs over the fibre's surface (Gojny et al., 2004). This methodology is highly compatible with existing industrial processes, can be scaled up for mass production, and is adaptable to a range of fibre diameters and lengths. In addition, spray coating is a non-destructive process which does not involve high temperatures or harsh chemicals and thus preserves the optic properties of the optical fibre.

The coating thickness can be controlled through the variation of simple parameters such as spray distance, pressure, deposition time and the concentration of the CNTs in the CNT suspension. However, there are difficulties in achieving a consistent coating thickness across the entire length of the fibre, hence it is important ensure the target substrate is centralised within coating area.

3.4 The Methodology Adopted: Comparison and Discussion

CVD is undoubtedly an advanced technique for the synthesising highly controlled parameters of CNTs with high purity which can ultimately allow for a high quality

SWCNT-SMF. However, CVD has poor compatibility with the natural material of optical fibres, which cannot easily allow the direct growth of CNT onto the optical fibres, which ensues a series of additional complex processes. Dip coating can be a much more simplistic and cost-effective approach in contrast to CVD, but struggles with coverage and precision. Although the coverage can be improved through additional layers, the overall coating process can take a long time due to the withdrawal speeds and drying times.

In the fabrication of the SWCNT-SMF in the later Chapter 5, we have chosen to adopt the spray coating methodology primarily for its fast, streamlined process, efficiency and ease of use, offering a balanced scalability for potential high throughput industrial applications. Due to the nature of spray coating there can be issues in uniformity. However, with the working principle of our fibre sensor being the localized interactions with the evanescent field, the impact of nonuniformity may not be significant. The primary function of the CNT coating is to enhance the interactions between the evanescent field, and the external environment, thereby increasing the sensitivity to the surrounding RI of the environment. The evanescent field only extends a short distance from the core into the cladding and the presence of CNTs should be sufficient for the sensing mechanism to function effectively. The huge advantage of evanescent field sensors is that they rely on cumulative effects of evanescent field along a length of the fibre. Therefore, the overall performance of the sensor depends more on the average interactions of the evanescent field and the CNT coating rather than the uniformity of the coating. This means that certain localized areas of CNT densities can still dominate the sensor response, compensating for areas that are uncovered, excessively covered or insufficiently covered. The main concern of

the non-uniformity lies only in the possibility of mode transitions to occur at areas where the non-uniform thickness far exceeds the thickness tolerances of mode transitions. Ultimately, as long as the spray coating methodology can provide sufficient balanced CNT coverage around the fibre, even if it is non-uniform, the sensor's performance can remain robust.

4 SIMULATION: CARBON NANOMATERIAL COATED LONG PERIOD FIBRE GRATING SENSOR

4.1 Introduction

LPFGs provides a solution for permitting interactions between the surrounding medium and the propagating light in the core via cladding modes. This unique interaction allows the LPFGs to have increased sensitivity to RI changes in the surrounding environment. Unlike other speciality fibres such as side-polished fibres and tapered fibres, LPFG does not require any mechanical alterations to the fibre structure, allowing them to maintain **the fibre's** structural integrity and long-term stability. When the LPFG sensor is exposed to the surrounding

Simulation: Carbon Nanomaterial Coated Long Period Fibre Grating Sensor environment with an RI lower than the cladding, the effective refractive index (ERI) of the cladding increases, leading to a blueshift in the resonant wavelength of the fibre. However, suppose the surrounding refractive index (SRI) exceeds that of the cladding. In that cases, the phase-matching condition will no longer be satisfied and there will be a loss of internal reflected light, leading to changes in the fibre's transmission properties.

While various speciality fibres have been derived down from the fundamental SMFs and how they are widely used in all optical applications, there has been limited exploration into CNT coated SMF for sensing applications. In comparison, the integration of CNT coatings on LPFG sensors has garnered more interest in recent years. This is primarily due to the enhanced interactions between the surrounding medium and **the 'leaky' modes**, which inherently makes LPFGs more sensitive to RI changes than the conventional SMFs.

In this section, we build upon the existing body of knowledge from recent literature, offering more in-depth exploration with a comparative analysis to better understand the effects of CNT coatings on optical fibre sensors. To simulate the CNT-LPFG design, the OptiGrating 4.2.3 software is utilised for its powerful ability to simulating grating designs and handle complex optical fibre structures through the transfer matrix method. This will help provide insights into the unexplored potential of CNT optical fibre sensors and pave the way for a novel chemical sensing platform with a simplistic approach.

Simulation: Carbon Nanomaterial Coated Long Period Fibre Grating Sensor

4.2 CNT-LPFG Working Principle

As discussed in Section 2.2.3.5, LPFGs provide a solution for permitting light interactions between the surrounding medium and the propagating light in the core through cladding modes without any mechanical alteration. For a CNT-LPFG sensor, the addition of a higher RI layer around the LPFG cladding will disrupt the **fibre's** phase-matching conditions. As a result, the LPFG cladding modes become 'leaky', leading to changes between all the light interactions in the guided fibre core, the cladding, the coating and the surrounding medium.

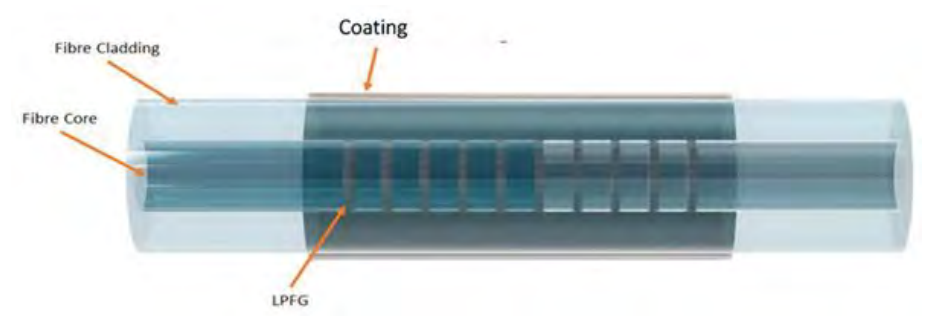


Figure 6 Schematic illustration of a carbon nanomaterial coated LPFG

In this scenario, the CNT-LPFG fibre can be modelled as a four-layer cylindrical waveguide (Figure 6) in which the amount of reflectance R at the fibre cladding/thin film interface can be expressed by equation 10 (Leveque and Villachon-Renard, 1990; Lu et al., 2014).

Simulation: Carbon Nanomaterial Coated Long Period Fibre Grating Sensor

$$R = \left| \frac{r_{cl/f} + r_{f/ext} e^{-i\varphi}}{1 + r_{cl/f} r_{f/ext} e^{-i\varphi}} \right|^{2}$$
 (10)

$$r_{cl/f} = \frac{n_{cl} - n_f}{n_{cl} + n_f} \tag{11}$$

$$r_{f/ext} = \frac{n_f - n_{ext}}{n_f + n_{ext}} \tag{12}$$

$$\varphi = \frac{4\pi}{\lambda} n_f d_f \tag{13}$$

Where $r_{cl/f}$ and $r_{f/ext}$ are the reflection coefficients of the cladding/thin film and thin film/external medium interfaces respectively. The refractive indices n_{cl} , n_{ext} and n_f correspond to the cladding, external medium and carbon nanotube thin film layer, while φ represents the phase change within the thin film layer of finite thickness d_f . The presence of the CNT coating layer of higher RI, enhances the evanescent wave interactions with the external medium, thereby improving the sensor's sensitivity towards RI changes.

The behaviour of the LPFG with a higher RI overlay can be described by the phase-matching condition

$$\beta_{co} - \beta_{cl,m} = \frac{2\pi}{\Lambda} \tag{14}$$

Where $\beta_{co}=\frac{2\pi}{\lambda}n_{co,eff}$ and $\beta_{cl,m}=\frac{2\pi}{\lambda}n_{cl,m,eff}$ are the propagation constants of the core and the mth cladding mode, and Λ is the grating period.

Simulation: Carbon Nanomaterial Coated Long Period Fibre Grating Sensor When the phase-matching condition is satisfied, coupling between the core mode and an mth order cladding mode occurs. Equivalently, the resonant wavelength λ_{res} can be expressed as

$$\lambda_{res} = (n_{co,eff} - n_{cl,m,eff})\Lambda \tag{15}$$

Therefore, for a standard LPFG, it can be interpreted that the lower-order modes are tightly confined in the cladding, while higher-order modes extend further out with greater interaction with the cladding or external environment. In addition, it is expected to have multiple resonance bands as several modes may satisfy the phase-matching condition. When the RI of the external environment increases, then the $n_{cl,m,eff}$ will increase accordingly and thus all resonance bands will shift. If we model a LPFG with an overlay of around 1.50RI coating that is slightly higher than the cladding, it can be predicted that the cladding modes are still mostly guided in the cladding, with only partial evanescent wave penetration into the coating. Although the $n_{cl,m,eff}$ of several modes slightly increases it remains distinctly below $n_{co,eff}$, which allows the phase matching condition below to satisfy multiple modes (m = 1, 2, 3, ...).

$$\frac{\lambda_{res}}{\Lambda} = n_{co,eff} - n_{cl,m,eff} \tag{16}$$

In such a case, the lower-order modes remain confined in the cladding whilst higher-order modes now extend further outwards and penetrate into the coating. As the coating has a higher RI, these higher-order modes experience a larger increase in $n_{cl,m,eff}$ and changes in the external RI should lead to greater shifts in the resonance bands.

Simulation: Carbon Nanomaterial Coated Long Period Fibre Grating Sensor For an LPFG with a much higher RI coating between 1.60-1.80RI, many cladding modes will lose their phase-matching condition. As $n_{cl,m,eff}$ would be much higher, many of them may exceed the $n_{co,eff}$ and they would no longer satisfy the phase-matching condition for any real wavelength. That mode would no longer be guided by the cladding and would become 'leaky' or guided in the coating. However, at least one mode still satisfies the condition, and that is the lowest-order hybrid mode. The lowest hybrid mode has an effective index just below the $n_{co,eff}$, so the phase-matching condition remains true at some wavelengths. For hybrid modes, part of their optic field lies in the cladding, but a large portion lies in the coating instead. As the hybrid mode is confined mostly in the coating, there are minimal to no changes in the resonance wavelength and leaves only intensity modulation to external RI changes. Although there is only one mode that satisfies the phase-matching condition, all the coupling energy from the core mode is transferred into that single hybrid mode, which can provide deeper resonance.

Another notable phenomenon of the CNT-LPFG sensor is the mode transition. With reference to Del Villar (Del Villar et al., 2006), who proposed the concept of mode transition, when the thickness of the overlay reaches a certain value, cladding modes will be guided by the overlay. Therefore, with an increase in the thickness of the CNT coating, modes guided in the cladding transition into the CNT layer. These mode transitions are evident for overlay thicknesses 400-600nm and 1900-2100nm in which the higher-order mode replaces the low-order modes (Gu et al., 2013). Thus, the amount of enhanced interaction is dependent on both the thickness and RI of the CNT layer.

4.3 OptiGrating Simulation Methodology

As we may know, an LPFG is formed through the introduction of a periodic refractive index modulation at the core of the optical fibre. Therefore, the structural aspects of an optical fibre were initially designed using the OptiGrating software.

	Step-Index Single-mode Fibre Parameters	
	Diameter	Refractive Index
Core	4.1µm	1.46
Cladding	62.5µm	1.45
Coating	0.5µm	1.50-2.00
Ambient Environment	20µm	1.00-1.44

Table 2 Step-index single mode optical fibre parameters

The structure of the optical fibre is based on a step-index single-mode fibre, with a core diameter of $4.1\,\mu m$ with a refractive index of $1.46\,RI$ and a cladding diameter of $62.5\,\mu m$ with a refractive index of $1.45\,RI$. Upon setting the parameters of the optical fibre's structure, another layer around the fibre's cladding is created with a width of $20\,\mu m$ and a refractive index of 1. This layer intends to simulate the surrounding ambient environment, air, the fibre is initially around. The refractive index of this layer will be changed accordingly to the simulation parameters to simulate various ambient environment.

LPFG Parameters		
Refractive Index Modulation	0.0001RI	
Grating Length	9cm	
Grating Period	246.8 µm	

Table 3 Parameters of the Long Period Fibre Grating used in the OptiGrating 4.2.3 software

The index modulation at the core of the fibre is what defines an LPFG. For our design of the LPFG, a sine grating with a uniform refractive index modulation of 0.0001RI was induced across a 9cm length of the optical fibre.

Simulation: Carbon Nanomaterial Coated Long Period Fibre Grating Sensor The parameters inputted into the OptiGrating 4.2.3 Software so far have defined an LPFG, but in order to simulate a CNT coated LPFG sensor, another layer must be included in the design. This layer intends to replicate the carbon nanotube coating and is introduced between the cladding of the LPFG and the surrounding medium. The typical refractive index CNT in comparison to the silica fibre's core and cladding is much higher with a typically value around 1.50-2.50RI depending on their structure density and thickness. To replicate the layer of carbon nanomaterial, an additional layer was initially introduced to the fibre parameters with a width of $0.5\mu m$ and a refractive index of 1.7RI.

The designed CNT coated LPFG will be simulated under an SRI of 1.30-1.44RI to investigate the effects of the variation of coating RI and thickness. The SRI ranges to be simulated are the typical RI ranges of water, acetone, ethanol and kerosene at room temperature. Across all the simulations, all modes between LP(0,0) and up to LP(0,10) were included for this particular investigation.

4.4 Simulation Results

4.4.1 Uncoated LPFG

In order to understand the effects of the additional layer of coating, an uncoated LPFG was initially simulated to set as a reference for comparison with the rest of the simulated parameters.

For the initial simulation of an uncoated LPFG, the results (Figure 7) have shown three clear distinct attenuation bands between the 1.525-1.675 μm wavelength of the transmission spectral response.

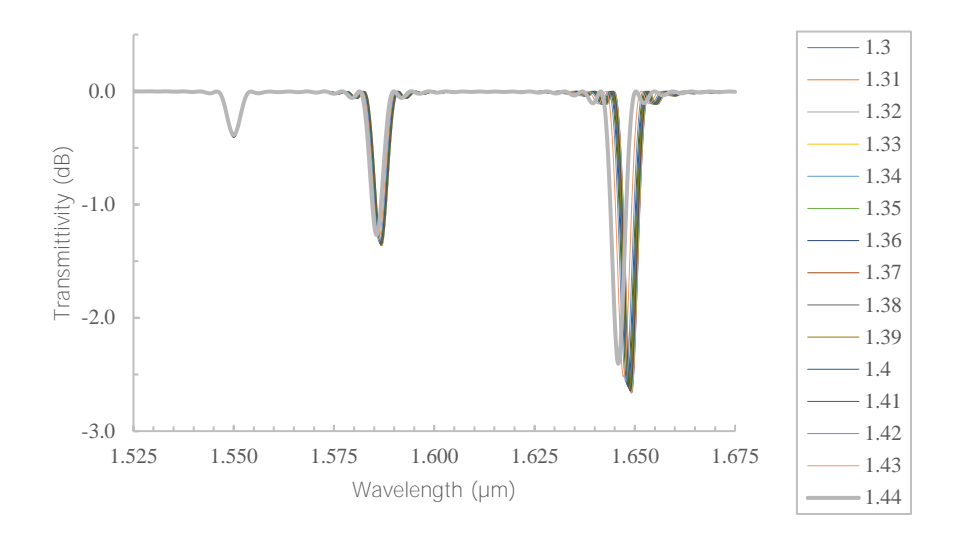


Figure 7. Results from an Uncoated LPFG showing the transmission spectral response between 1.5250-1.675μm wavelengths

The first attenuation band demonstrates a change in transmittivity against the change of the SRI between 1.30-1.44RI whilst the second and third attenuation band demonstrates both attenuation band shift as well as a transmittivity change against the change of SRI. With an increase in the SRI, the second and third attenuation band demonstrates a correlation between attenuation band shift and a reduction in the attenuation band's transmittivity. It should also be noted that with the change of SRI, there is a greater attenuation band shift and change in transmittivity found for the third attenuation band than the second attenuation band.

Simulation: Carbon Nanomaterial Coated Long Period Fibre Grating Sensor

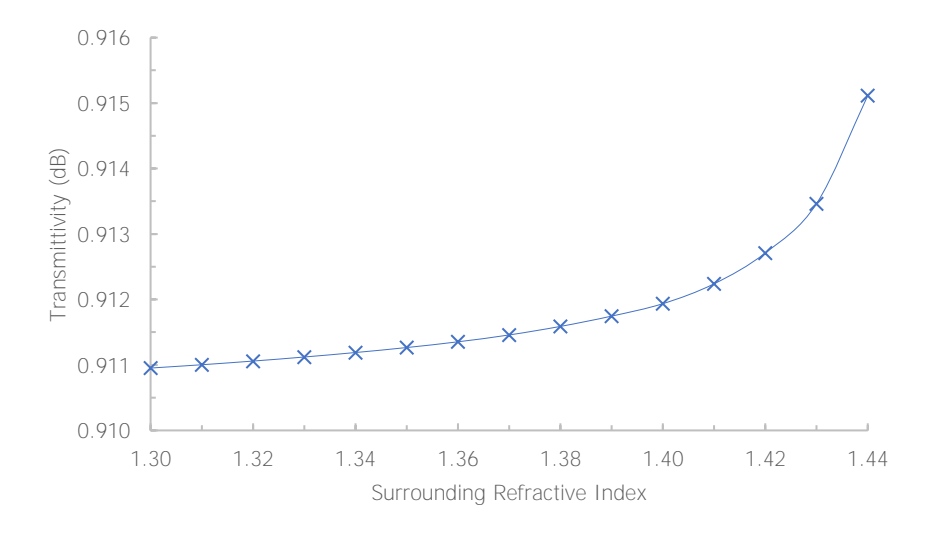


Figure 8. Results from an Uncoated LPFG showing the transmittivity response of the first attenuation band located at 1.550µm wavelength against the SRI.

With a closer inspection at the first attenuation band as shown in Figure 8, the transmittivity response against the SRI change can be described to be in an non-linear increasing relation.

4.4.2 Various RI Coatings

Utilising the fibre and grating parameters outlined in Chapter 4.3 along with the simulation methodology provided, this section will display the simulated transmission spectral response received from the different RI of coatings between 1.50-1.90RI at an overlay thickness of $0.5 \mu m$, which is subjected to an SRI between 1.30-1.44RI.

4.4.2.1 1.50RI Coated LPFG

A coating with a refractive index of 1.50RI is only slightly higher than the cladding's refractive index. However, an evident change has already been observed in the transmission spectral response. As shown in Figure 9a), when a 1.50RI coated LPFG of 0.5μm thickness is subjected to an SRI between 1.30-1.41RI, three distinct attenuation bands can still be observed between 1.525-

Simulation: Carbon Nanomaterial Coated Long Period Fibre Grating Sensor $1.675\mu m$ wavelength of the transmission spectrum. However, when subjected to an SRI of 1.42-1.44RI, there is only one attenuation band, which is found to be located at the $1.550\mu m$ wavelength of the transmission spectrum.

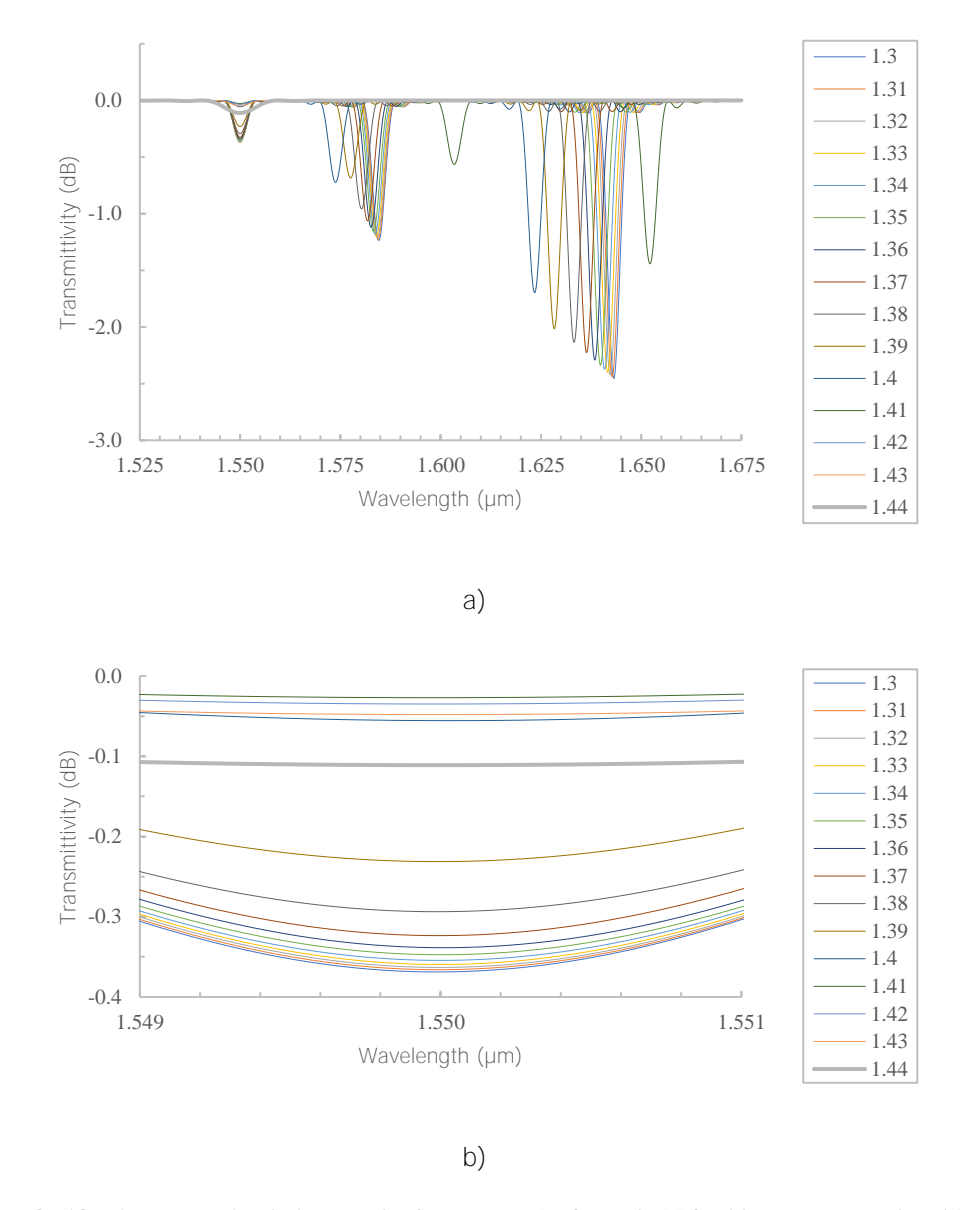


Figure 9. OptiGrating 4.2.3 simulation results from a 1.50RI Coated LPFG with 0.50μm overlay thickness showing the transmission spectral response (a) between 1.525-1.675μm wavelength (b) Closeup of the first attenuation band between 1.525-1.675μm wavelength.

From Figure 9, the first attenuation band remains to have no attenuation band shift against the change in SRI and only affects the transmittivity of the first attenuation band. The second and third attenuation bands, as shown in Figure 9a), remain to have a blue shift with the change in RI from 1.30-1.41RI. However,

Simulation: Carbon Nanomaterial Coated Long Period Fibre Grating Sensor the amount of attenuation band shift against the change in SRI is more apparent when compared to the uncoated LPFG.

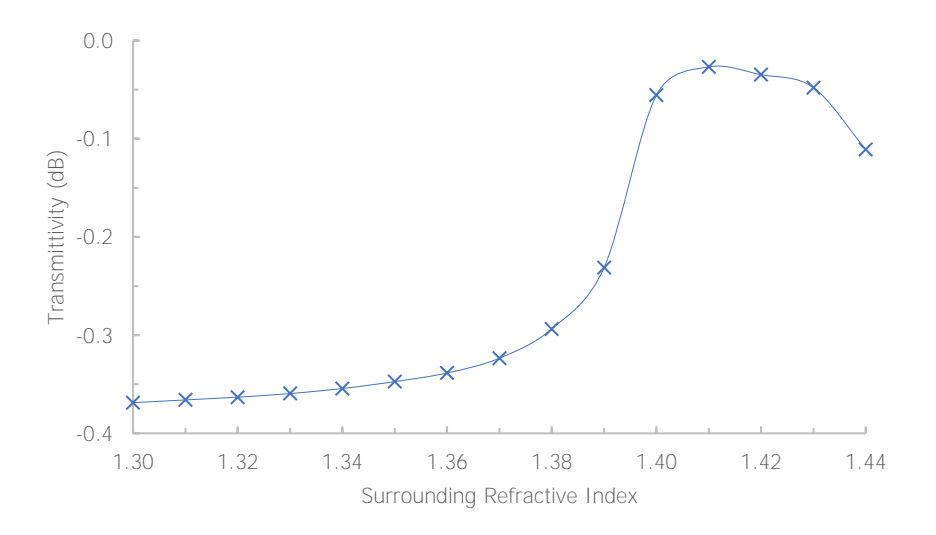


Figure 10. Results from a 1.50RI coated LPFG of 0.5µm thickness show the transmittivity response of the first attenuation band located at 1.550µm wavelength against the SRI.

The transmittivity response against the change in SRI for the first attenuation band can be observed in Figure 10. There is trend of an exponentially increasing transmittivity response against the change in SRI between 1.30-1.40RI. However, between an SRI of 1.41-1.44RI, a gradual decreasing relationship is observed with the transmittivity response.

4.4.2.2 1.60RI Coated LPFG

At a coating with a refractive index of 1.60RI, the effects of applying a coating with a higher refractive index than the cladding are now clearer, as shown in Figure 11. Unlike the transmittivity response received from a 1.50RI Coated LPFG, a 1.60RI coated LPFG only has one attenuation band observed at 1.550 μm wavelength of the transmission spectrum. The attenuation band also has a much lower minimum set starting with -46dB being the lowest minimum observed (Figure 11b).

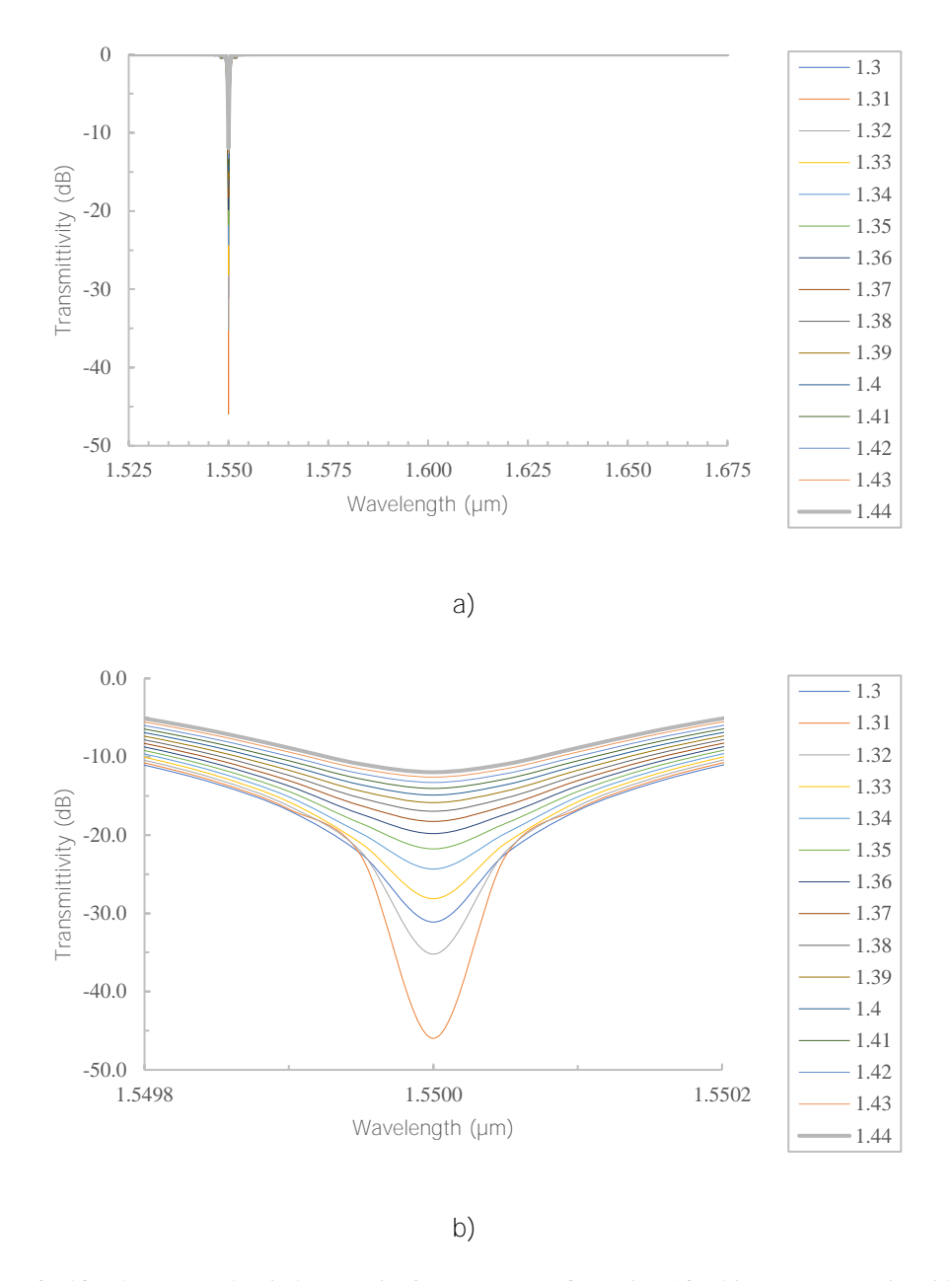


Figure 11. OptiGrating 4.2.3 simulation results from a 1.60RI Coated LPFG with 0.50μm overlay thickness showing the transmission spectral response (a) between 1.525-1.675μm wavelength (b) Closeup of the first attenuation band between 1.525-1.675μm wavelength.

From Figure 12, apart from the initial transmittivity response from an SRI of 1.30, a positive non-linear correlation in transmittivity can be observed from the increase in SRI from 1.31-1.44RI. With a much lower minimum observed from the attenuation band for a 1.60RI Coated LPFG (Figure 11) than an Uncoated LPFG and a 1.50RI Coated LPFG, the amount of transmittivity change against the change in SRI is also observed to be significantly higher overall (Figure 12).

Simulation: Carbon Nanomaterial Coated Long Period Fibre Grating Sensor

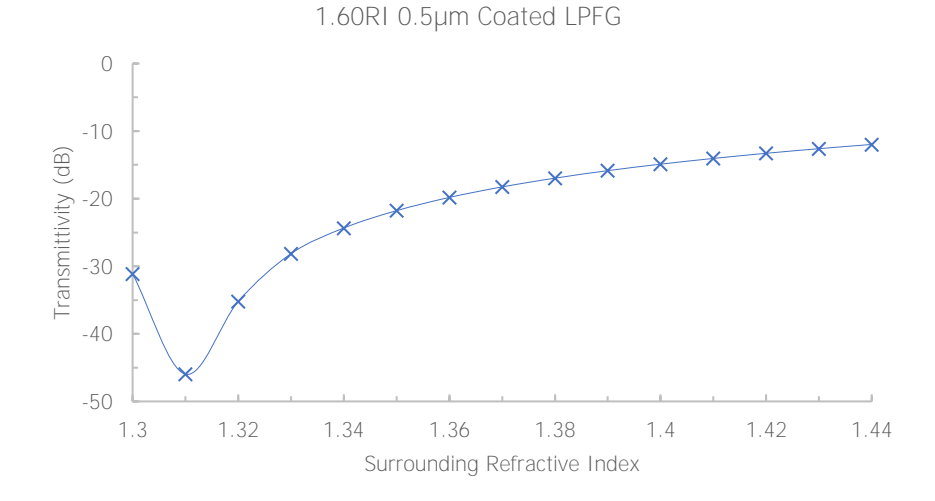


Figure 12. Results from a 1.60RI coated LPFG of 0.5\pm thickness show the transmittivity response of the first attenuation band located at 1.550\pm wavelength against the SRI.

4.4.2.3 1.70RI Coated LPFG

With a 1.70RI coating, one attenuation band can be observed at the 1.550μm wavelength of the transmission spectrum. The attenuation bandwidth observed is significantly narrower than that of an Uncoated LPFG, 1.50RI Coated LPFG and 1.60RI Coated LPFG. The lowest minima of the attenuation band observed from Figure 13b is approximately -7.42dB.

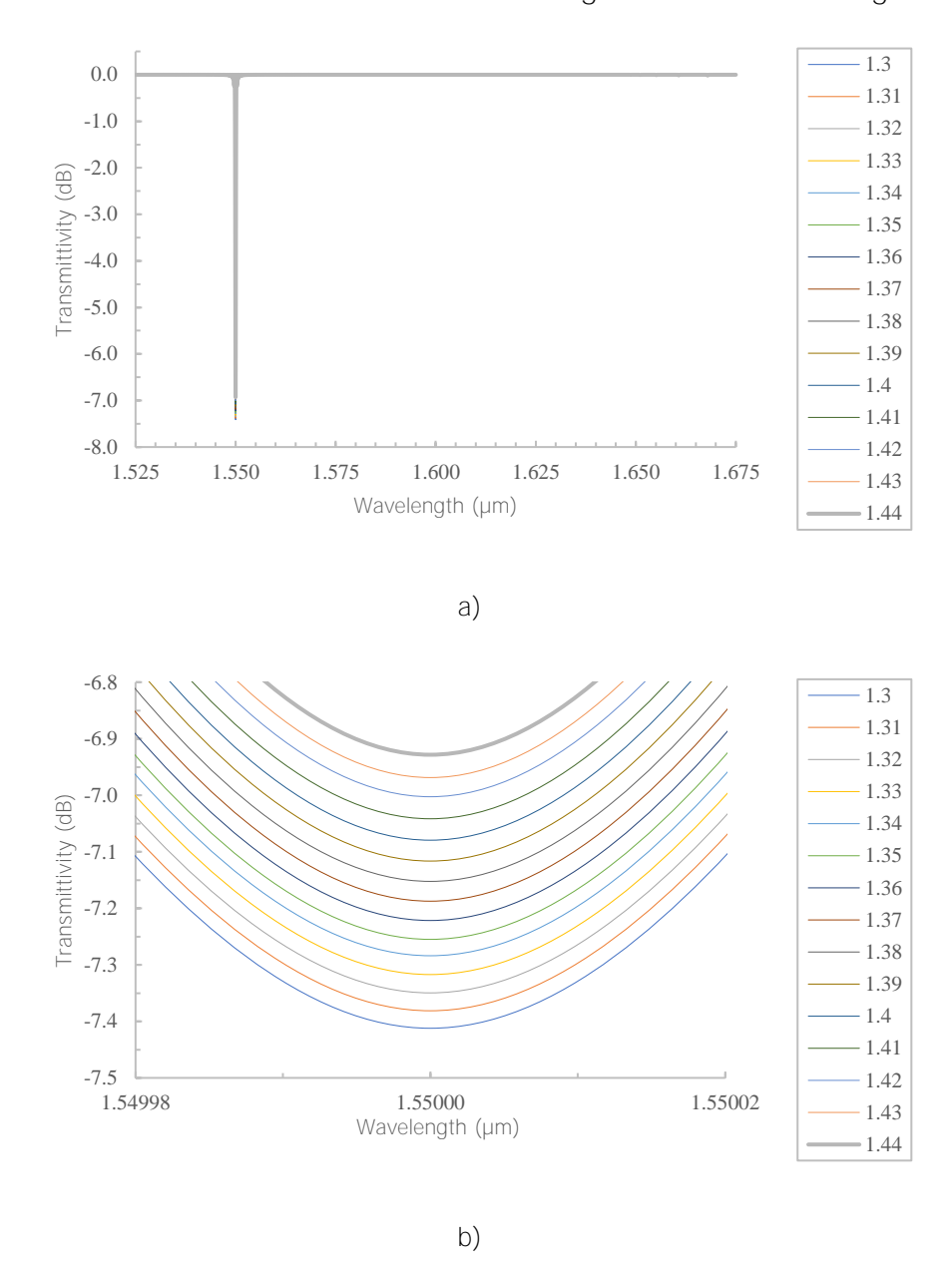


Figure 13. OptiGrating 4.2.3 simulation results from a 1.70RI Coated LPFG with 0.50µm overlay thickness showing the transmission spectral response (a) between 1.525-1.675µm wavelength (b) Closeup of the first attenuation band between 1.525-1.675µm wavelength.

Despite the minimum of a 1.70RI Coated LPFG being located much higher than a 1.60RI Coated LPFG, the separation between each minima in the 1.70RI Coated LPFG is quite even as shown in Figure 13b. From a change of viewpoint, Figure 14 shows the transmittivity response against the change in SRI, which suggests a clear linear correlation between an SRI of 1.30-1.44RI.

Simulation: Carbon Nanomaterial Coated Long Period Fibre Grating Sensor

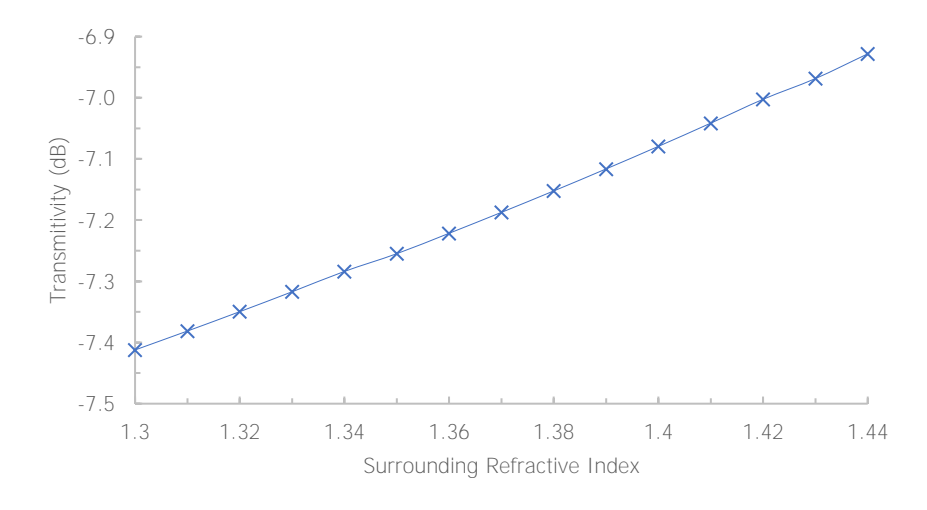


Figure 14. Results from a 1.70RI coated LPFG of 0.5 \(\mu \) thickness showing the transmittivity response of the first attenuation band located at 1.550 \(\mu \) wavelength against the SRI.

4.4.2.4 1.80RI Coated LPFG

From Figure 15, the application of a significantly higher coating RI around the LPFG also results in the formation of a single attenuation band with a narrower attenuation bandwidth and raised minimum level. Observing closely at the attenuation peak in Figure 15b, the overall separation between each minima is quite even but there is a clear gap showing more transmittivity change between the SRI 1.39-1.40RI.

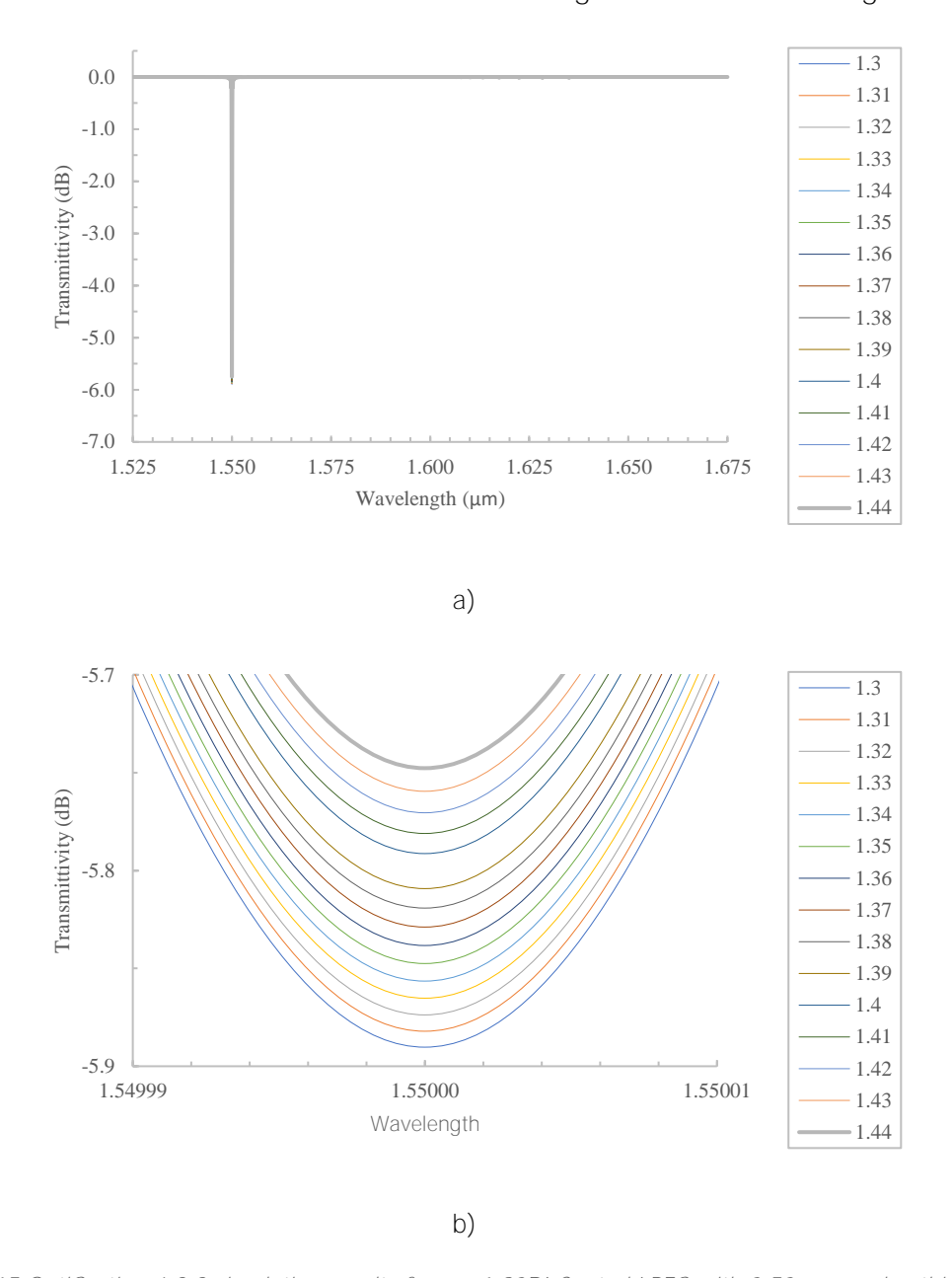


Figure 15 OptiGrating 4.2.3 simulation results from a 1.80RI Coated LPFG with 0.50µm overlay thickness showing the transmission spectral response (a) between 1.525-1.675µm wavelength (b) Closeup of the first attenuation band between 1.525-1.675µm wavelength.

Some linear correlation can be observed between the change in SRI against the change in transmittivity as shown in Figure 16. However, with the 'gap' highlighted in Figure 15b, a 'step' in the linear correlation can be observed in Figure 23.

Simulation: Carbon Nanomaterial Coated Long Period Fibre Grating Sensor

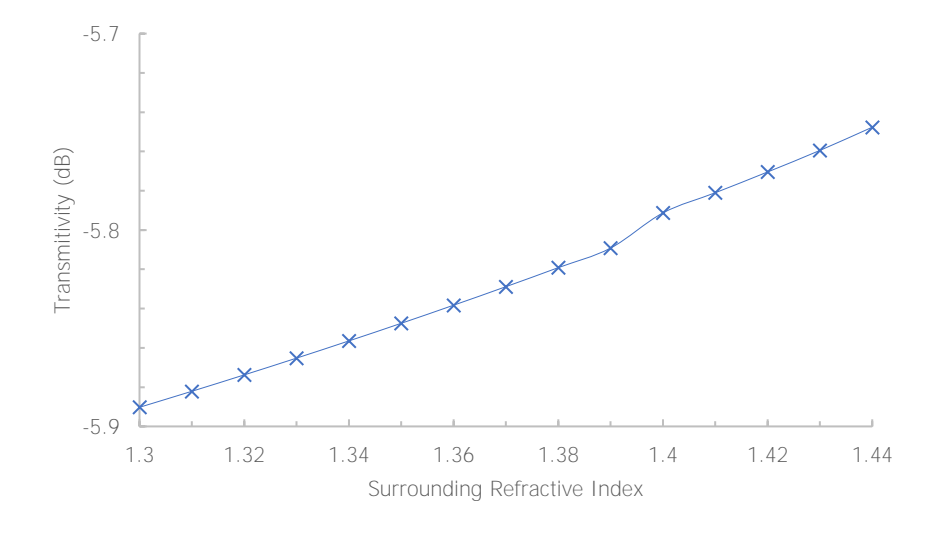


Figure 16. Results from a 1.80RI coated LPFG of 0.5μm thickness showing the transmittivity response of the first attenuation band located at 1.550μm wavelength against the SRI.

4.4.2.5 1.90RI Coated LPFG

With a much higher RI coating around the LPFG to 1.90RI, the attenuation bandwidth is now the narrowest among all the previous simulated refractive indexes of coatings. For a 1.90RI Coated LPFG, only one attenuation band can be observed in the transmission spectrum and the minimum of the attenuation band observed in Figure 17 is found to be slightly higher than what was observed in a 1.70RI and 1.80RI Coated LPFG.

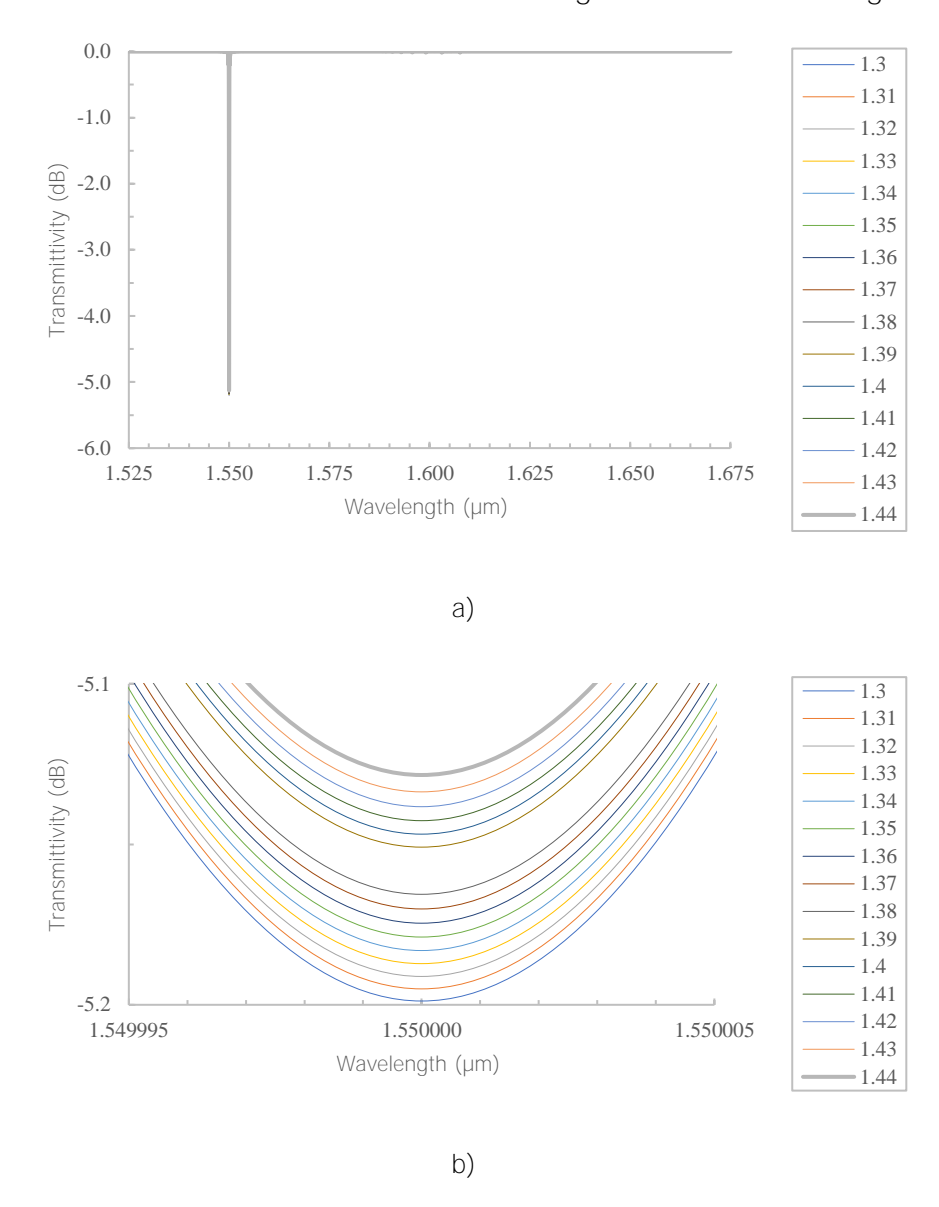


Figure 17. OptiGrating 4.2.3 simulation results from a 1.90RI Coated LPFG with 0.50μm overlay thickness showing the transmission spectral response (a) between 1.525-1.675μm wavelength (b) Closeup of the first attenuation band between 1.525-1.675μm wavelength.

Similarly to the 1.80RI Coated LPFG, the separations between each minima of the attenuation band from a 1.90RI Coated LPFG are quite even with a single separation larger observed within them. However, quite different to the 1.80RI Coated LPFG, the larger separation in the 1.90RI Coated LPFG is found to be between an SRI of 1.38-1.39RI instead. The particularly larger separation shown in Figure 17b, is also clearly outlined as a 'step' change in the linear correlation from Figure 18.

Simulation: Carbon Nanomaterial Coated Long Period Fibre Grating Sensor

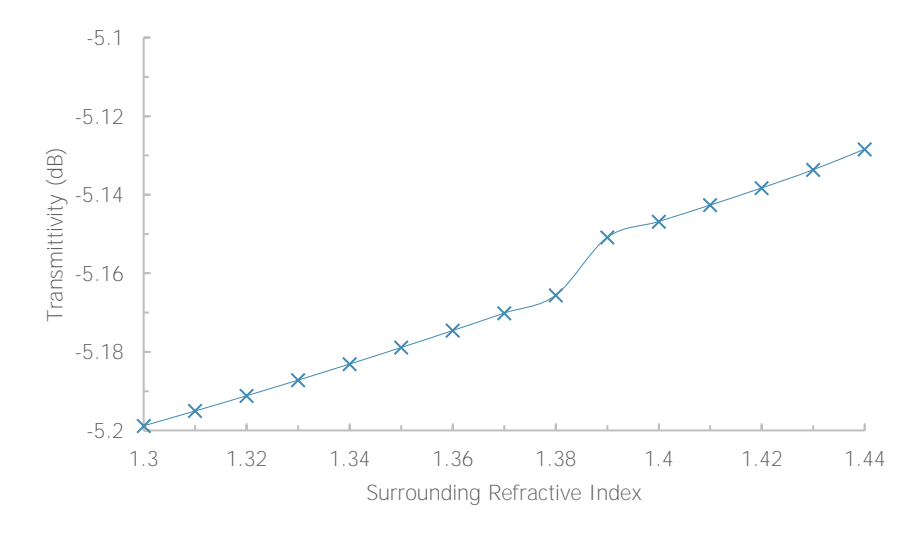


Figure 18 Results from a 1.80RI coated LPFG of 0.5µm thickness showing the transmittivity response of the first attenuation band located at 1.550µm wavelength against the SRI

4.5 Comparison: Results against Theory

To evaluate the theoretical expectations of a coated LPFG, various RI coatings have been simulated on an LPFG. The simulated results have shown to be consistent with the theoretical expectation of a coated LPFG.

For the results of a 1.50RI $0.5\mu m$ coated LPFG, three distinct attenuation bands were observed which confirms the expectation that multiple cladding modes remains to be phase-matched. The second and third bands exhibited greater shifts in the attenuation bands with the change in RI, suggesting greater sensitivity. This behaviour further aligns with the theory that the higher-order modes experience greater changes of external RI.

At a 1.60RI 0.5 µm coated LPFG, the behaviour shows only 1 single attenuation band, this further confirms the theory that the higher RI coating would induce stronger coupling that suppresses the higher-order cladding modes as they are no longer the phase matched. The remaining single attenuation bands correspond to the expected remaining low-order hybrid mode that is weakly

Simulation: Carbon Nanomaterial Coated Long Period Fibre Grating Sensor guided in the cladding but exhibits a much stronger interaction with the transmission spectrum, demonstrating deeper attenuation bands.

The 1.70RI 0.5 µm coated LPFG, similarly to the 1.60RI 0.5 µm coated LPFG, presents a single attenuation band but with reduced attenuation band depth and narrower bandwidth. This behaviour corresponds again to the theory, when the coating RI is much greater, the cladding modes are weakly guided and shift towards being coating-guided. The reduced attenuation depth and narrow bandwidth indicate weaker coupling between the core and cladding modes. This means that the hybrid mode for a 1.70RI 0.5 µm coated LPFG becomes more confined within the coating, reducing spatial overlap with the core mode field, causing attenuation band intensity to vary linearly with SRI changes. This linearity is consistent at even higher RI of 1.80-1.90R, and corresponds to the theory that the coupling is further reduced at higher coating Ris, which weakens the sensitivity to SRI changes.

4.6 Comparison: Amongst Various RI coatings

To compare the performance of the LPFGs, the transmittivity response against the change in SRI across all the simulated RI coatings are compiled together. From Figure 19a, there is a much greater change in transmittivity observed in a 1.60RI Coated LPFG than any other simulated refractive index coatings. In this configuration, a coating between 1.60-1.70RI may provide the most sensitivity against the change in SRI. However, if there was a linearity requirement in the results between the transmittivity against the SRI for the detection of a wide range of SRIs 1.30-1.44RI or beyond, then coatings with a refractive index of

Simulation: Carbon Nanomaterial Coated Long Period Fibre Grating Sensor 1.70RI, 1.80RI and 1.90RI maybe more suitable. Further in detail at the comparison between these three refractive indexes, as shown in Figure 19b, it is clear that a 1.70RI Coated LPFG exhibits greater sensitivity to the change in SRI. It can be summarized that some linearity, between the transmittivity against the SRI, can be obtained for specific SRI ranges at a coating RI higher than 1.60RI. However, with the increase in refractive index of the coatings above 1.70RI, there is a decrease in the coated LPFG's sensitivity against the change in SRI.

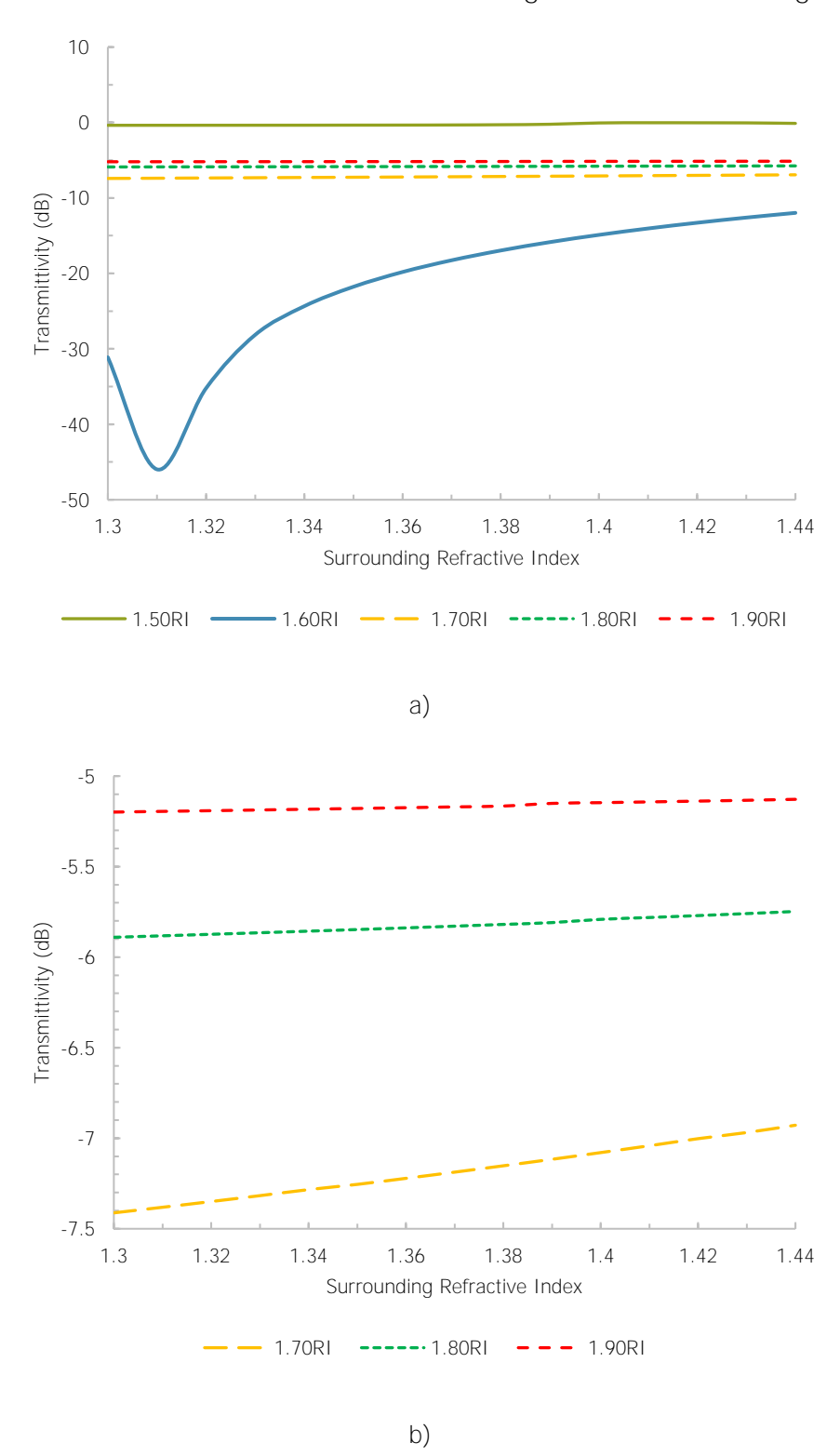


Figure 19 Comparison with Different Refractive Indexes of Coatings a) Between 1.50-1.90RI b) Between 1.70RI-2.90RI

4.7 Comparison: Coating Thickness

Under the same fibre and grating parameters outlined in Chapter 4.3 and used in Chapter 4.4.2, the coatings of different refractive index (1.50-1.90RI) are

Simulation: Carbon Nanomaterial Coated Long Period Fibre Grating Sensor simulated under an SRI between 1.30-1.44RI with variations to the coating's thickness of $0.50\,\mu\text{m}$, $0.52\,\mu\text{m}$ and $0.54\,\mu\text{m}$. Figure 20 displays the extracted transmittivity minima of the 1.550 μ m wavelength attenuation band (from various simulated parameters of different coating refractive indexes and coating thicknesses) plotted against the change in SRI.

For a slightly higher refractive index coating of 1.50RI than the cladding around the LPFG (Figure 20a), the variation of the coatings thickness did not appear to make any significant changes to the correlation between the transmittivity of the minima and the change of SRI. However, with the increase of coating thickness, a definite reduction in the intensity minima can be observed.

At a coating with 1.60RI refractive index, we can see that the variation of coating thickness has induced a stronger effect on the correlations (Figure 20b). The correlation demonstrating the highest sensitivity to the change of SRI is when the coating thickness is set to $0.50\mu m$. As we increase the coating thickness, the sensitivity of the correlations gradually decreases, with a coating thickness of $0.54\mu m$ demonstrating the least sensitivity.

At a coating of 1.70RI (Figure 20c), the LPFG seems to exhibit a linear correlation against the change in SRI and with the increase of coating thickness to $0.52\mu m$ and $0.54\mu m$ would result in a decrease the sensitivity of the LPFG.

Simulation: Carbon Nanomaterial Coated Long Period Fibre Grating Sensor

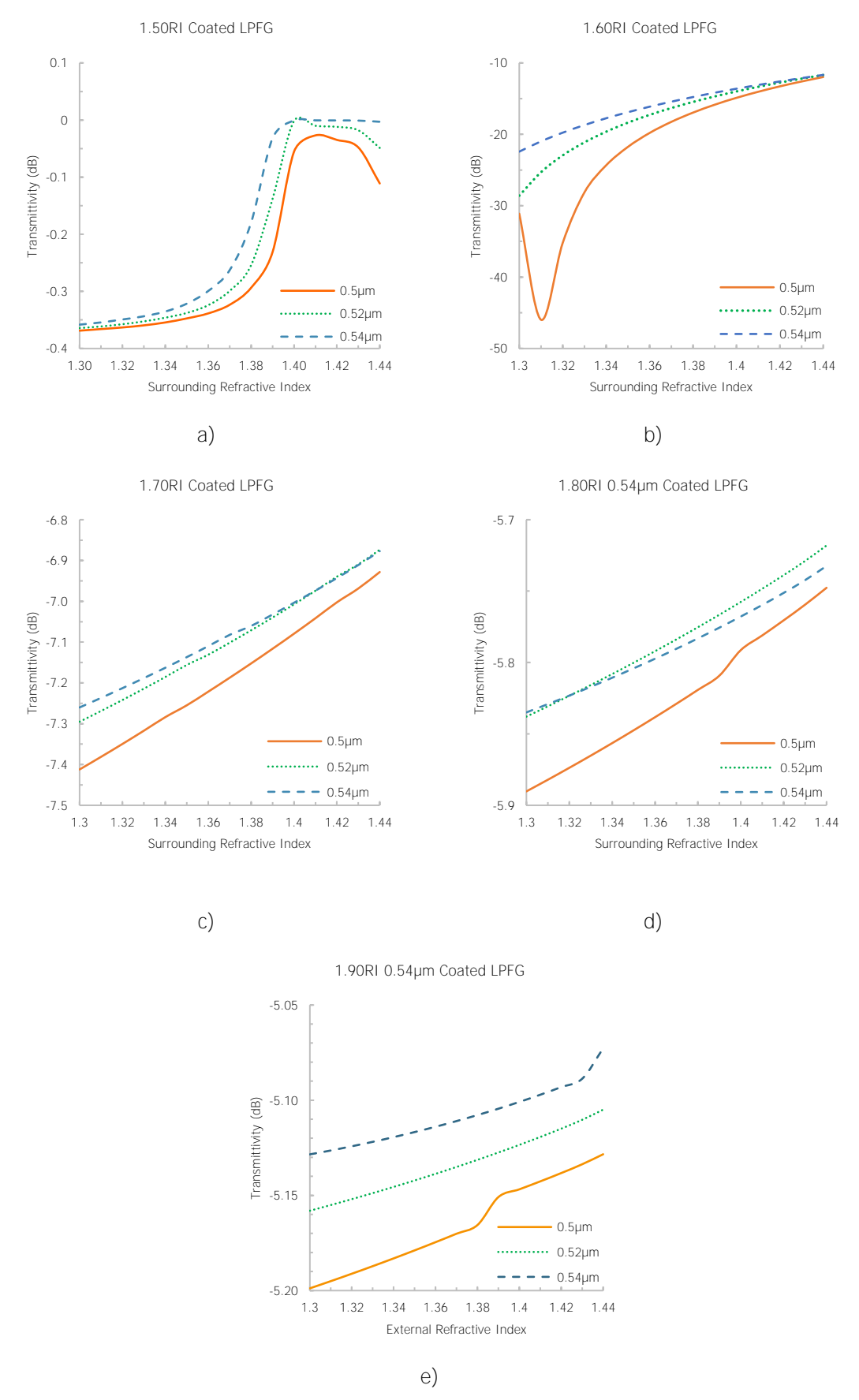


Figure 20 The transmittivity response of the intensity minima at the 1.550μm attenuation band against the SRI with variations of thickness (0.50μm, 0.52μm and 0.54μm) for a) 1.50RI Coated LPFG b) 1.60RI Coated LPFG c) 1.70RI Coated LPFG d) 1.80RI Coated LPFG e) 1.90RI Coated LPFG.

Simulation: Carbon Nanomaterial Coated Long Period Fibre Grating Sensor For a 1.80RI coated LPFG with a coating thickness of $0.50\mu m$, the correlation can be considered mostly linear with a 'step' change in the correlation as discussed in Chapter 4.4.2.4. Although the sensitivity of the LPFG decreases with the increase in coating thickness, the 'step' change found present in the correlation of a $0.5\mu m$ thick coating is not found from thicker coatings of $0.52\mu m$ and $0.54\mu m$. At a significantly higher refractive index coating of 1.90RI around the LPFG, the increase in the coating's thickness remains to reduce the sensitivity of the coated LPFG. Amongst all the simulated variations of coating thicknesses, a correlation with no "step' change is only found at a coating thickness of $0.52\mu m$.

4.8 Discussion

This section will discuss the key factors influencing the performance variations of the CNT-LPFG sensor, with a focus on the trade-offs between sensitivity versus linearity, the effects of the CNT coating thickness, abnormalities arising amongst the response due to mode transitions and comparison to existing literature.

4.8.1 Sensitivity vs Linearity

From the results, it can be observed that a coating of 1.60RI tends to have a significantly greater sensitivity in comparison with others RI coatings of the same coating thicknesses. Whilst coatings greater than 1.70RI provides linear correlations with reduced sensitivity due to weaker coupling between the core modes and the hybrid mode as mentioned in Chapter 4.2 and 4.5.

In reality, for any scalable reproductions, it is very difficult to ensure that every fabrication will have a consistent coating of 1.60RI and $0.5 \mu m$ thickness. As

Simulation: Carbon Nanomaterial Coated Long Period Fibre Grating Sensor shown in Figure 19, a $0.02\mu m$ variation of thickness can lead to a significant change in sensitivity and correlation pattern. This means that the manufacturing processes must be extremely accurate for reproducibility, or more complex and tailored calibrations must be necessary to facilitate the tolerable differences of each fabricated CNT-LPFG sensor. However, if there was an application that demands higher sensitivity and precise production is possible, then a coating towards 1.60RI and $0.5\mu m$ thickness will prove to be more beneficial.

Linearity in a correlation can be a critical factor for the design, performance and mass production of sensors as it can allow for simplified calibration and straightforward interpretations. In addition, the importance of linear correlations in sensors can also be further dependent on their application and detection parameters. For example, if there was a requirement for a large scale production of CNT-LPFG sensors with equipment that does not have much control over the coating technique, then a coating with higher RI between 1.70RI-1.90RI maybe necessary. The higher RI coating can allow for more tolerances to the variation of thickness from the coating, as it would only attenuate the sensitivity of the sensor without affecting the overall correlation. Alternatively, if more accurate deposition methodologies can be made available for larger-scale production, then the sensor can gradually be coated with carbon nanomaterials closer to 1.60RI to gain greater sensitivity.

4.8.2 Abnormalities and Mode Transitions

Throughout various RI coatings, between 1.50-1.90RI, the overall correlation relates to a stronger transmittivity response when the coating thickness is thinner. However, there are some abnormalities present within these results which

Simulation: Carbon Nanomaterial Coated Long Period Fibre Grating Sensor appears to shift the correlation abruptly. These abnormalities are particularly evident for LPFGs with CNT coatings of 0.50μm 1.60RI, 0.50μm 1.80RI 0.50μm 1.90RI, and 0.54 μm 1.90RI. Amongst these four particular conditions, the somewhat linear correlation appears to have a 'step' change. These abnormalities or 'step' changes can be explained by the theory of mode transitions as discussed in Chapter 4.2, in which mode transitions would occur when certain thickness of coating is reached. From the results, it can be observed by adjusting the coating thickness appropriately, the 'step' changes in the correlation can be mitigated. This knowledge would be particularly useful for designing the coating parameters of a CNT optical fibre sensor as having a correlation without any 'step' changes can allow for more straightforward analysis and calibrations. However, it should be noted that these 'step' changes in the correlation may not be within the required scope of detection and thickness adjustment may not be required due to their irrelevance.

4.8.3 Comparison to Literatures

Previous research on carbon nanomaterial coated LPFGs has been focused on demonstrating the effectiveness of the coating on LPFG sensors and how it has enhanced the sensor's performance without much consideration of the parameters of the coating layer. The results of the simulated CNT-LPFG sensor can be compared with existing studies to understand for any alignments and discrepancies.

Simulation: Carbon Nanomaterial Coated Long Period Fibre Grating Sensor

Coating RI	Coating Thickness (um)	RI Detecting Range	Sensitivity (dB/RIU)
1.50	0.50	1.30 - 1.35RI	0.44
		1.37 - 1.39RI	4.65
	0.52	1.30 - 1.35RI	0.52
		1.37 - 1.39RI	8.05
	0.54	1.30 - 1.35RI	0.92
		1.37 - 1.39RI	11.75
	0.50	1.31 - 1.33RI	891.50
		1.35 - 1.44RI	108.89
1.60	0.52	1.31 - 1.33RI	209.00
1.60	0.52	1.35 - 1.44RI	74.44
	0.54	1.31 - 1.33RI	114.50
		1.35 - 1.44RI	58.00
1.70	0.50	1.30 - 1.44RI	3.43
	0.52	1.30 - 1.44RI	3.07
	0.54	1.30 - 1.44RI	2.71
	0.50	1.30 - 1.39RI	0.89
1.80		1.40 - 1.44RI	1.00
	0.52	1.30 - 1.44RI	0.86
	0.54	1.30 - 1.44RI	0.71
1.90	0.50	1.30 - 1.38RI	0.38
		1.39 - 1.44RI	0.40
	0.52	1.30 - 1.44RI	0.43
	0.54	1.30 - 1.44RI	0.29

Table 4 The calculated sensitivities of the simulated CNT-LPFG sensor in correspondence to specific RI detecting ranges

Table 4 shows the calculated sensitivity of each simulated CNT-LPFG for specific RI detecting ranges. Amongst the simulated CNT-LPFG sensors, 1.60RI coatings exhibit the highest overall sensitivity and 1.70RI coatings was found to exhibit the highest sensitivity amongst the CNT-LPFGs with linear correlations.

Simulation: Carbon Nanomaterial Coated Long Period Fibre Grating Sensor

Intensity Modulated carbon nanomaterial	Coating	RI Detecting	Sensitivity
coated LPFG Sensors	Thickness	Range	(dB/RIU)
Carbon-nanotube-deposited long period fiber	Several micrometres	1.33 - 1.38RI	31
grating for continuous refractive index sensor applications (Tan et al., 2014a)		1.38 - 1.42RI	47
Layer-by-layer assembly of polyelectrolytes- wrapped multi-walled carbon nanotubes on long period fiber grating sensors (Ni et al., 2019)	11.421μm	1.3488 - 1.4337RI	85
Graphene oxide functionalized long period fiber grating for highly sensitive haemoglobin detection (C. Liu et al., 2018)	501.8 <i>n</i> m	1.33 - 1.38RI	76.5

Table 5 Sensitivity of Intensity Modulated carbon nanomaterial coated LPFG Sensors from existing literatures

Table 5 shows the sensitivities of intensity modulated carbon nanomaterial coated LPFG sensors from existing literatures. From the table, it can be seen that the coating thickness of the GO-LPFG sensor (C. Liu et al., 2018) is similar to the simulated coating thickness. It can also be noted that the RI of the coating layer is not identified in the literatures like many other carbon nanomaterial integrated optical sensors. As the RI of the coating can be dependent on many factors such as the optical density, layered structure and their structural arrangements, it can be difficult to identify the RI and absorption characteristics of the carbon nanomaterial (Zhao et al., 2004; M. Haque et al., 2006). In addition, if the carbon nanomaterial coating is not uniform structurally, there can also be significant variations to its effective RI. Furthermore, differences to the simulation can arise as the simulation considers the coating as a whole object which does not account for the actual complex structural deposition of the carbon nanomaterial around the LPFG. However, with comparison to the simulated CNT-LPFG, it can be approximated that the coating of the GO-LPFG (C. Liu et al., 2018) has a RI that falls within the region of 1.60-1.70RL

Simulation: Carbon Nanomaterial Coated Long Period Fibre Grating Sensor For comparison with a CNT-LPFG (Tan et al., 2014a) of similar structural setup to the simulation. It can be interpreted that the coating RI also falls within the regions of 1.60-1.70RI. However, quite unlike the GO-LPFG (C. Liu et al., 2018), the sensitivity of the CNT-LPFG (Tan et al., 2014a) is much lower, this can be due to the thickness being several fold thicker. This behaviour corresponds to the simulated CNT in which the sensitivity of the sensor is attenuated with the increase of the coating thickness.

4.9 Summary

In summary, a carbon nanomaterial coated LPFG gas sensor has been simulated using the OptiGrating 4.2.3 software and with the introduction of the carbon nanomaterial layer, an intensity modulated CNT-LPFG can be realised. The simulation has provided valuable insights into its potential for real-time chemical monitoring. The results have indicated that the integration of a carbon nanomaterial layer onto the optical fibre will significantly enhance the sensor's sensitivity, which is a key factor in improving the accuracy and responsiveness of the sensor to varying chemical concentrations. The simulations of various coating parameters demonstrates the interplay between sensitivity, linearity which highlights the potential trade-offs that must be carefully balanced in the sensor's for optimal performance according to its application.

The RI of the coating was found to influence the sensor's overall performance. A 1.5RI coating would still enable the LPFG to exhibit wavelength modulated behaviour. However, the sensitivity to SRI changes and is significantly enhanced in comparison to an uncoated LPFG. With RI coatings greater than 1.60RI, in which the characteristics of carbon nanomaterials come into play, the LPFG

Simulation: Carbon Nanomaterial Coated Long Period Fibre Grating Sensor sensor would begin to exhibit intensity modulated behaviour which can allow for more simplistic analysis and computation methodologies. Amongst the range of coating RI simulated, 1.60RI exhibits the greatest overall sensitivity across an SRI range of 1.30-1.44. However, dependent on the requirement, RI coatings between 1.70-1.90RI provides a linear correlation that can allow for more simplistic calibrations for mass manufacturing scenarios.

Overall, the simulated sensing scheme validates the potential of CNT-LPFG sensor for chemical sensing, whilst pointing out crucial areas for improvement in sensor design from optimisation of coating thickness to management of mode transition effects. These findings provide a strong foundation for future experimental work.

5 FABRICATION OF SWCNT-SMF SENSOR

5.1 Introduction

In this chapter, we propose a design, fabrication methodology and experimental evaluation of a single-walled carbon nanotube coated single mode fibre (SWCNT-SMF) sensor for chemical detection. Building upon the theoretical ground work and simulation studies in Chapter 2-4, the goal here is to realize a simplistic, compact and sensitive single point invasive optical fibre sensor for real-time continuous monitoring of chemical concentration based on the variation of RIs In Chapter 4, the simulations were conducted to investigate the transmission characteristics of a CNT coating and develop a theoretical foundation for understanding how the CNTs interact under widely studied fibre platforms such as the LPFGs. In addition, as LPFGs enhance the sensitivity of a fibre, it allows

more pronounced correlations to be analysed, making it more suitable for theoretical investigations of coating parameters such as refractive index (RI) and thickness that could be subtle in an SMF. The setup simulated a broadband light source connected to a coated LPFG and then a spectrometer. This configuration enabled the analysis of the transmission spectra across a range of SRI. Furthermore, the simulation was to address an experimental limitation, as the RI of the CNT coating on the SMF may not be directly measurable due to the nonuniformity of the spray-deposited layer. To accommodate this uncertainty, coatings with 1.50-1.90RI and thicknesses of 0.50-0.54 µm were simulated with comparison to existing literature. This allowed the simulation to provide a reference that can be used to interpret the experimental results, even when the actual coating RI is unknown and to hypothesise the effects on an SMF. The simulation also provided a coating thickness of 0.50 µm as an effective region that maximised the intensity modulation. These insights were directly applied in the experimental design, where a 0.50 mm coating thickness was targeted to verify that the effects would be similar on an SMF.

The experimental work in this chapter employs a reflection-based configuration. The setup consists of a broadband source connected to a circulator and an SWCNT-SMF that is immersed in a dextrose solution of varying concentrations. The fabricated SWCNT-SMF will primarily target a coating thickness of 0.50 μ m. The SWCNT-SMF sensor system intends to provide a proof-of-concept that the intensity modulated behaviour and optical enhancement properties from the SWCNT would remain effective on a SMF.

The SWCNT-SMF configuration offers several advantages compared to the simulated coated LPFG configuration. The SWCNT-SMF configuration would be a single-point reflective-based sensor allowing for minimally invasive, compact and easily deployable sensing, which is beneficial to restricted and confined environments. Furthermore, the simple structure of an SMF eliminates the need for complex grating fabrications to form an LPFG.

The following sections will outline the step-by-step procedures for the optical fibre preparation, deposition of CNT onto the fibre, and the sensor system assembly. The SWCNT-SMF sensor will be subjected to real-time detection of varying dextrose concentration levels, which will provide performance details for evaluation and comparison.

5.2 Experimental Methodologies

This section will detail the methodologies used for the fabrication of the fibre sensor probe, characterisation of the CNT deposition and the RI sensing experimentation of the fabricated SWCNT-SMF fibres.

5.2.1 Fibre Sensor Probe Fabrication Methodology

The sensor **probe's** fabrication can be broken into three primary stages: the preparation of the fibre, CNT coating solution synthesis and the spray coating.

5.2.1.1 SMF Preparation

The fundamental structure of the sensor probe is based on a Thorlabs SMF-28 Fibre with a core and cladding diameter of $8.2\mu m$ and $125\pm0.7\mu m$ respectively. A SMF will provide a simple yet robust platform with low susceptibility to

environmental perturbations compared to delicate structures such as LPFGs, FBGs, tapered fibres and side polished fibres. Additionally, the use of SMFs can allow the ease of deployment into existing optical infrastructures and telecommunication networks which can ultimately detect chemicals at multiple remote regions simultaneously.

Initially, a 0.5m length of fibre is cut from a reel of SMF-28 using Kevlar Cutting Shears. The jacket at both ends of the 0.5m SMF-28 is removed for a length of 6cm with a Fibre Stripper. As there is a buffer coating on this particular fibre, a Thorlabs T06S13 Fibre Buffer Stripper is used to remove the coating to expose the bare cladding of the fibre. To ensure, that the end face cross-section at both ends of the fibre is flat, a fibre cleave is used to cut the excess fibre down to the required exposed cladding length of 1cm/3cm. The Fibre is then cleaned with some Acetone and optical cleaning tissues. The final prepared fibre is then observed with a 10x magnification eye loupe to make sure there are no defects along the exposed fibre and end faces. If no defects are present, the fibre is now ready to be coated.



Figure 21 Schematic illustration of the prepared SMF

5.2.1.2 SWCNT Solution Preparation

The SWCNT solution is a very important aspect of the fibre sensor probe and as such there are also many factors that must be considered when making the preparations. As discussed in Chapter 3.4, the coating methodology adopted is

spray coating. Primarily, the amount of SWCNTs in the SWCNT solution must be carefully considered as it can have an impact on the latter coating stage. If there are too many SWCNTs they may not be well dispersed and if there are too little SWCNTs the fibre may not be coated sufficiently. The SWCNT chosen for creating this solution is a Merck SWCNT with a 0.78nm average diameter.

The base of the solution is first prepared with a 1:1 ratio of de-ionised water and Fischer Scientific 99.5% Isopropanol (IPA) by weight in a beaker. The desired amount of SWCNT would then be weighed out in a glass jar and the base solution would be added to the jar for it to be stirred with a magnetic stirrer for 5minutes at room temperature. A lid is placed on the jar of SWCNT solution to prevent any splattering and is then placed into an ultrasonic bath for 5minutes to help the dispersion of the SWCNTs into the solution. The prepared SWCNT solution is then filled into the tank of the spray gun and sprayed on plain paper to observe for any issues.

Further SWCNT solutions have been prepared with an aqueous dispersant from Alfa Aesar for comparison. Using a 3ml Pipette, a single drop of the dispersant was added for a 100g base solution of IPA-Water. Similarly, the SWCNTs would then be added to the IPA-Water-Dispersant (IWD) solution where it would be stirred for 5minutes and then sonicated for another 5minutes at room temperature. The prepared SWCNT solution with dispersant is then filled into the tank of the spray gun and sprayed on plain paper to observe for any issues.

CNT Aqueous Dispersant				
Chemical Component	Weight Composition %			
Polyethylene glycol branched nonylphenyl ether	50.00			
Water	39.50			
2,4,7,9-tetramethyl-5-Decyne-4,7-diol	10.00			
2-Butoxyethanol	0.50			

Table 6 Chemical Component and their corresponding weight percentages of the Aqueous CNT dispersant.

In both prepared SWCNT solutions, with and without dispersant, their dispersibility and stabilisation will be analysed.

5.2.1.3 Coating Stage

The coating stage can be commenced once the two core components, the SMF and SWCNT solution, are prepared. The platform in which the coating takes place consists of a hot plate placed flat vertically as the heated backboard with a glass plate adhered directly on top to act as the surface on which the coating occurs on. The SMF samples with the prepared coating end of the fibre would be sandwiched between two glass slides and secured with thermal tape. Up to 5 fibre samples can be placed on the glass slide at a time with each fibre sample separated by a fibre jacket width.

Once the samples are secured to the glass slides, it is placed on top of the glass plate and held down with some masking tape to lightly secure the position. A 0.28mm nozzle Harder & Steenbeck Evolution CRplus Two in One Airbrush is clamped into position 20cm perpendicularly away, producing a 4cm radii coating area around the prepared fibre samples. The airbrush is powered by a Fengda FD-186 compressor set to 5PSI for the entire duration of coating.



Figure 22 Example Coating Setup for the prepared SMF-28 Fibre with masking tape on the four corners of the glass plate platform for temperature measurements

The hot plate is then heated till the glass plate reaches 100°C. An infrared thermometer is used to measure the four checkpoints of the glass plate to ensure that the required temperature is met. The heat is to allow quick evaporation of the IPA and water in the SWCNT solution so the SWCNTs can be adhered to the cladding of the fibre samples. The airbrush trigger is pressed to allow the deposition of SWCNTs for 5seconds with a stopwatch. The sample is then left to dry for 5minutes before repeating for two additional deposition and drying procedures. The glass slide is then flipped to allow the uncoated side of the fibre's cladding to be deposited for a total of three times as well with 5minutes of drying in between. For this fabrication, the coated fibre would be classed as a SWCNT-SMF with a single coating procedure. SWCNT-SMF samples are then allowed to cool down to 30°C before it is removed from the coating platform and stored individually for the latter experimentation stages outlined in Chapter 5.2.3.

For the purpose of the experimentation and analysis outlined in Chapter 5.2.3.1 and 5.2.3.2, coated lengths of 1cm and 3cm SWCNT-SMF was fabricated with the methodology mentioned above to be analysed. As an alternative for comparison,

a different set of 1cm and 3cm SWCNT-SMF was created with doubled amount of coating durations and another set with quadruple the amount.

5.2.2 Characterisation Methodology

To analyse the surface topography of the fabricated SWCNT-SMFs, a Zeiss CrossBeam 350 Focused Ion Beam Scanning Electron Microscope (SEM) was used. The fabricated SWCNT-SMFs are initially mounted on an SEM specimen stub and then inserted into the sample holder.

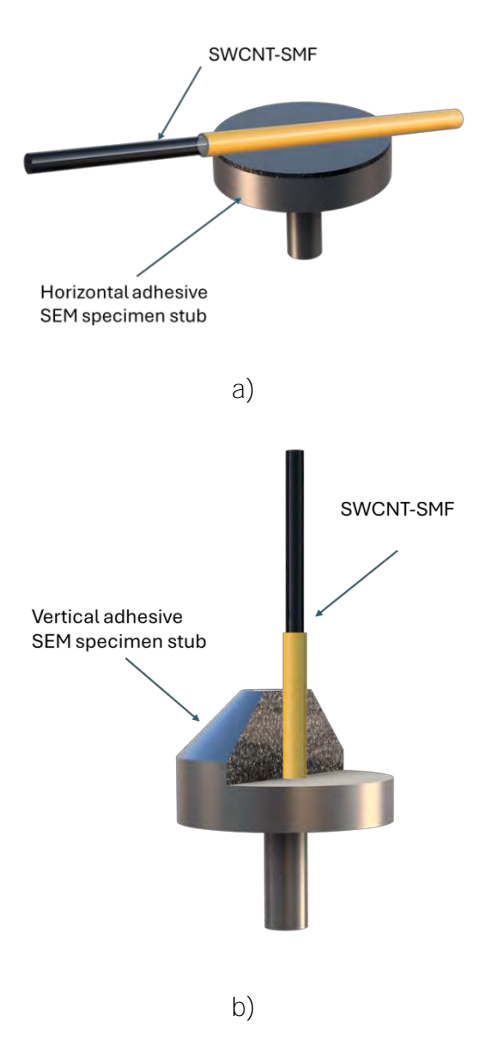


Figure 23 Schematic Illustration on SWCNT-SMFs mounted on a) a horizontal adhesive SEM specimen stub, b) a vertical adhesive specimen stub

The SWCNT-SMF samples are then placed into the SEM chamber which is then airlocked. The SEM is initially set at an approximate working distance of 6mm

and the focus was fine-tuned to achieve maximum clarity on the CNT deposited areas of the samples. SEM images are then captured at various magnifications for analysis.

5.2.3 RI Sensing Methodology

This section provides a detailed methodology to the RI sensing experimentation which consists of the preparation of the RI sensor setup and the RI sensing test solutions.

5.2.3.1 RI Sensor Setup

The RI sensor setup consists primarily of a Thorlabs 6015-3-FC SMF optical Circulator (OC) with Port 1 connected to a COMPTYCO AUA-MC-1315 portable optical Light Source (OLS) and an Ocean Optics Flame-NIR Spectrometer to Port 3. Port 2 of the OC is connected to a Thorlabs BFT1 Bare Fibre Terminator with a Thorlabs B30126C3 - FC/PC Single Mode Connector to allow the fabricated SWCNT-SMF to be connected.

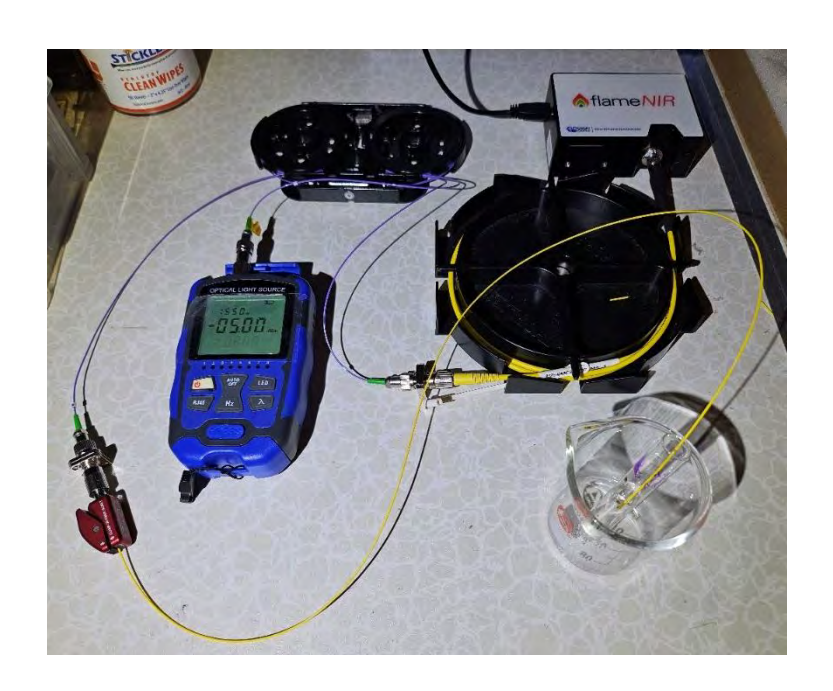


Figure 24 Image of the used equipment with the SWCNT-SMF integrated into the RI sensing setup

The theory behind this setup is that the propagating light from the OLS will travel down the circulator to the SWCNT-SMF in which the darker material coating of SWCNTs around the SMF cladding will enhance the light interaction between the ambient environment and the leaky modes of the SWCNT-SMF. The reflected light from the SWCNT-SMF would then travel back through the circulator to the spectrometer for analysis.

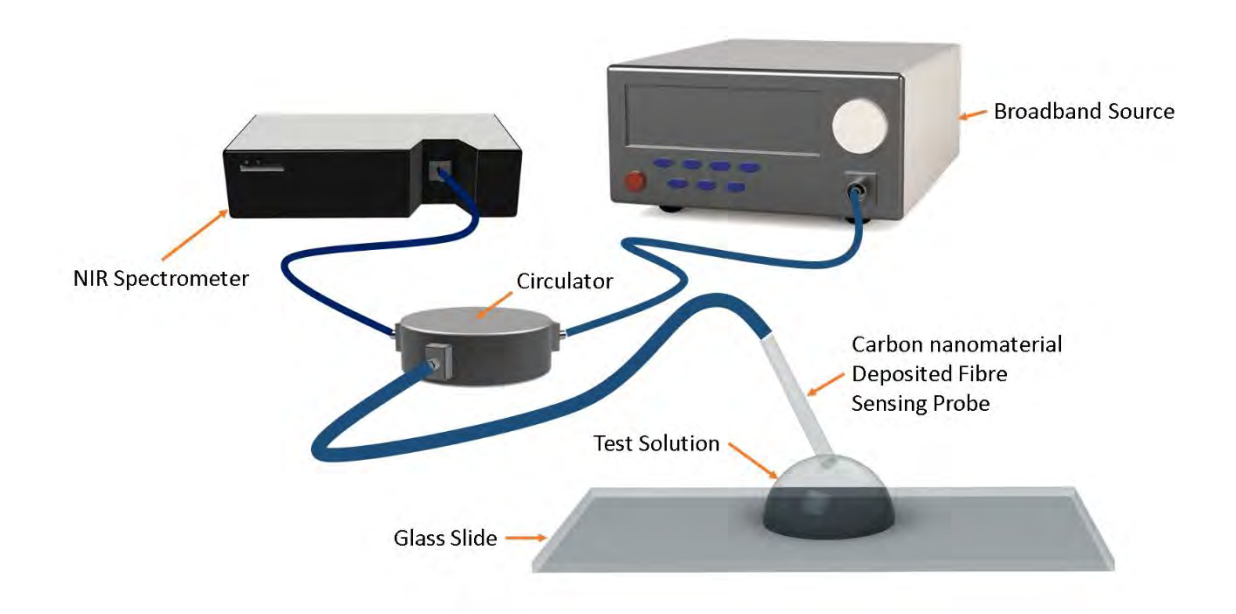


Figure 25 Illustration and model of the SWCNT-SMF sensing element integrated into the RI sensing setup. For the RI sensing experimentation, the coated end of the SWCNT-SMF will be dipped in a test tube filled with 6ml of test solution. The SWCNT-SMF will be dipped in de-ionized water for 10s and then allowed to dry for 1minute between each test.

5.2.3.2 RI Sensing Test Solution Preparation

The test solutions in which the SWCNT-SMF will be submerged in for analysis is made from a Sigma-Aldrich G8270 D-(+)-glucose (dextrose). A dextrose solution was chosen for its simplicity in adjusting the RI through dilution of an initial solution with de-ionised water. An initial 50% concentration (w/v) dextrose

solution is made by adding 250g dextrose to a 70°C 500ml de-ionized Water in which it is stirred with a magnetic stirrer and kept at a temperature of 70°C for 30minutes till all particles are dissolved. A 100ml of the 50% concentration dextrose solution is taken and diluted down to 40%, 30% 20% and 10% by the addition of de-ionized Water with a single channel pipettor. The diluted mixtures are stirred for 5minutes at a temperature of 40°C and then transferred to a glass jar for storage and later use. A 0% dextrose solution is made from pure de-ionized Water. Each concentration of dextrose solution is tested with a Kruss Optronic DR 201-95 to obtain their corresponding refractive indexes.

Concentration of Dextrose Solutions (w/v)	Surrounding Refractive Index	
0% (Pure De-ionized Water)	1.3335	
10%	1.3369	
20%	1.3451	
30%	1.3625	
40%	1.3679	
50%	1.3789	

Table 7 The RIs of the various synthesized concentrations of Dextrose solution

5.3 Experimental Results and Discussion

This section presents the results from the prepared SWCNT solution, characterisation of the fabricated SWCNT-SMF and the RI sensing experimentation.

5.3.1 Prepared SWCNT solution

Various concentrations of SWCNTs with and without dispersant have been synthesized for analysis. The chosen variation of SWCNT solution will be further discussed in this section

5.3.1.1 0.005% SWCNT Solution

A concentration of 0.005% (w/w) SWCNT solution was prepared as an initial attempt to observe its suitability to be used as the coating for the prepared fibre. The SWCNT solution was found that even after 5minutes of sonication, there remains large amount of SWCNTs that are not dispersed. From observation, large amounts of SWCNTs can be seen to adhere to the side of the glass jar and after the solution is left to stand for 120minutes, clumps of SWCNTs can be found at the base of the jar.



Figure 26 Image of an emptied jar of 0.005% concentration (w/w) SWCNT solution showing severe adherence of SWCNTs on the inside with huge clumps of SWCNTs at the base.

Due to these issues, the concentration will not be uniform throughout the entire solution. When the solution is loaded into the spray gun and the trigger is pulled in an attempt to spray, the spray gun is immediately clogged. In addition, two further sets of 5minute sonication was applied to the SWCNT solution but there were no improvements to the dispersion of the SWCNTs and the blockage to the spray gun.

5.3.1.2 0.0005% SWCNT Solution

For a concentration of 0.0005% (w/w) SWCNT solution, some SWCNTs can be visibly observed to be adhered to the insides of the glass jars instantly after

synthesis. Upon standing for 120minutes, the SWCNTs appear to split from the solution and the transparent base solution of IPA-Water can be observed in some areas of the glass jar. Despite the splitting of the SWCNT and base solution occurring, some SWCNT remains to be adhered to the insides of the glass jar. When the SWCNT solution is sprayed, persistent clogging of the spray gun is found to occur after between 3-5 seconds of continuous spraying.



Figure 27 Image of a jar of 0.0005% concentration (w/w) SWCNT solution showing some adherence of SWCNTs to the inside surface of the jar with splitting between the SWCNT and IPA-Water.

Two further sets of 5minute sonication were applied to the SWCNT solution but there was no easing of the blockage that occurs to the spray gun nozzle and remains to split upon standing over time.

5.3.1.3 0.00025% SWCNT Solution

For a concentration of 0.00025% (w/w) SWCNT solution, small amounts of SWCNTs can be visibly seen to adhere to the inside of the glass jar. Upon standing for just 120minutes the SWCNTs appear to have sunken to the bottom of the glass jar with minimal inner surface adhesion and have split itself from the solution where the top half of the SWCNT solution is purely the base solution of IPA-Water. When the CNT solution is sprayed, clogging of the gun is found to occur after 8-20 seconds of continuous spraying.



Figure 28 Image of a jar of 0.00025% concentration (w/w) CNT solution showing minor adherence of CNTs to the inside surface of the jar and splitting of the CNT and IPA-Water.

Two further sets of 5minute sonication were applied to the SWCNT solution but the solution remains to split upon standing over time and the occurrence of blockage remained the same.

5.3.1.4 0.005% SWCNT Solution with Dispersant

At a concentration (w/w) of 0.005% of SWCNTs, after 30minute of standing some adherence to the inside of the glass jar but no visual splitting of the SWCNTs from the IWD solution can be observed. From the naked eye, it is obvious that some particles in the SWCNT solution are much bigger than what can be passed through the nozzle of the spray gun.



Figure 29 Image of a 0.005% concentration (w/w) SWCNT solution with dispersant that is half-poured showing large clumps of SWCNT adherence to the inside of the jar

In addition, when the SWCNT solution fully poured to another beaker, some clumps of SWCNT can be seen at the bottom of the jar undispersed.



Figure 30 Image of the base of an emptied 0.001% concentration (w/w) SWCNT solution with dispersant showing giant clumps of CNTs at the base of the jar

When the SWCNT solution is loaded into the spray gun to spray, clogging of the spray gun begins in 7-15seconds of continuous spraying.

5.3.1.5 0.0005% SWCNT Solution with Dispersant

At a concentration (w/w) of 0.0005% of SWCNTs with dispersant, after 120minute of standing no visual splitting of the SWCNTs from the IWD solution can be observed. However, It is obvious that some particles in the SWCNT solution are much bigger than what can be passed through the nozzle of the spray gun. When the SWCNT solution is transferred to another beaker, there are no giant clumps of SWCNTs found undispersed at the bottom of the glass jar. Clogging of the spray gun is found to occur between 22-52seconds of continuous spraying.



Figure 31 Image of a 0.0005% concentration (w/w) SWCNT solution with dispersant showing minor adherence to the inside of the jar

5.3.1.6 0.00025% CNT Solution with Dispersant

At a concentration (w/w) of 0.00025% of SWCNTs, there is no splitting between the SWCNT and the IWD solution with no giant clumps found throughout the solution. When loaded in the spray gun, no clogging was found at a continuous spray time of 3minutes. Even with further standing of the SWCNT solution as long as 24 hours, the CNTs remains well dispersed without splitting and when loaded into the spray gun, no clogging was found under the same spraying durations



Figure 32 Image of a 0.00025% concentration (w/w) SWCNT solution with dispersant with minimal SWCNTs adhered to the inside of the jar.

5.3.1.7 SWCNT Solution: Choice and Discussion

Initially, a SWCNT solution composed of just IPA and water was created due to its simplicity. However at an SWCNT concentration (w/w) of 0.005%, the spray

gun had immediately failed due to large amounts of undispersed SWCNTs that has clumped together. In attempt to resolve this issue, reduced concentration of SWCNT was used to make the latter solutions. As a result, longer durations of spraying can be made with further reduction of SWCNTs. However, such reductions came with issues where the SWCNTs in the solution would split from the IPA-Water base solution over short amounts of time. This meant that although the spray gun could be used for longer continuous durations, the SWCNTs in the solution may not be uniformly dispersed which can lead to uneven deposition of SWCNTs from the spray gun.

To improve the SWCNT solution, an addition of an aqueous dispersant was explored. At the same initial SWCNT concentration (w/w) of 0.005%, there is slightly less adherence of the SWCNTs to the inside surface of the glass jar. Although there exist to be some clumps of undispersed SWCNTs that can be seen by the naked eye, the size of these clumps is much smaller than the clumps found in the SWCNT solution without dispersant. It was found that with a reduction of SWCNT concentration (w/w) down to 0.00025%, the solution is found to be more dispersed without splitting occurring with the IWD solution and continuous deposition can be achieved without any clogging of the spray gun for long durations.

The importance of a well dispersed SWCNT solution is to ensure that all the SWCNTs are uniformly dispersed initially throughout the entire solution and so that no giant clumps of SWCNTs will clog the spray gun nozzle. If the spray gun is clogged, it can take a long duration to clean and will interrupt the coating process which further leads to non-uniform coating of the fibres. A well stabilised

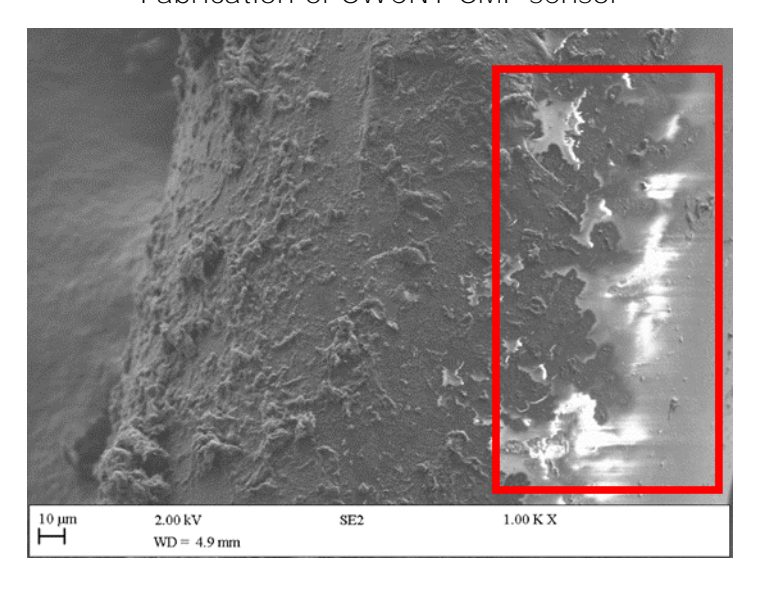
SWCNT solution is equally important as it will ensure that the initial dispersed concentration of SWCNTs remains uniform throughout the entire duration of the coating process. From the different variations of SWCNT solutions, the SWCNT solution with dispersant and a SWCNT concentration of 0.00025% fits both of these requirements and is therefore chosen as the one to be used in the later fabrication processes of the sensor element.

5.3.2 Characterisation of SWCNT-SMFs

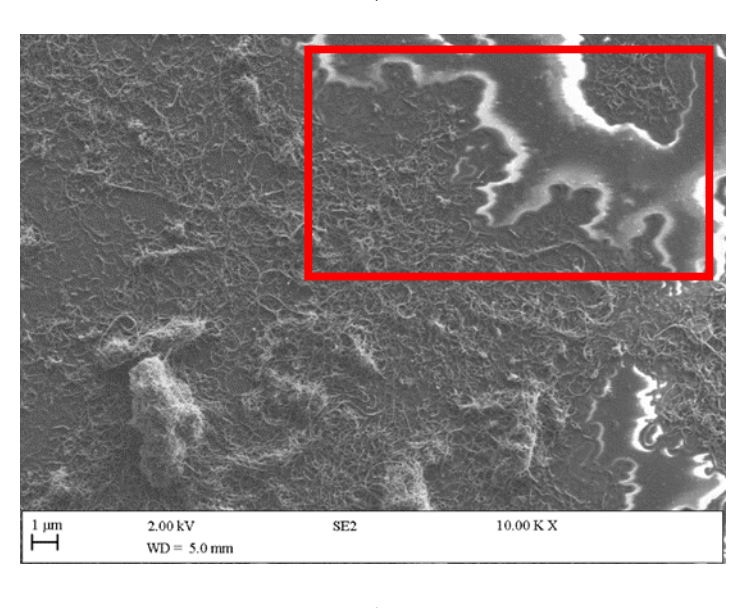
This section illustrates and discusses the SEM surface topography the SWCNT-SMFs.

5.3.2.1 Single Coated SMFs

For a $1\mu m$ length of SWCNT-SMF with a single set of coating applied to, there are some areas that can be seen to not have been coated entirely and uniformly. These uncoated areas appears under the SEM to be 'reflective' and is outlined in Figure 33. In addition, from the SEM it can be seen that there are large clumps of SWCNTs at various locations that are deposited around the fibre with some clumps greater than $10\mu m$ in width. Regardless, at 10000x magnification as shown in Figure 33b the SWCNT can be confirmed to be successfully deposited onto the SMF.



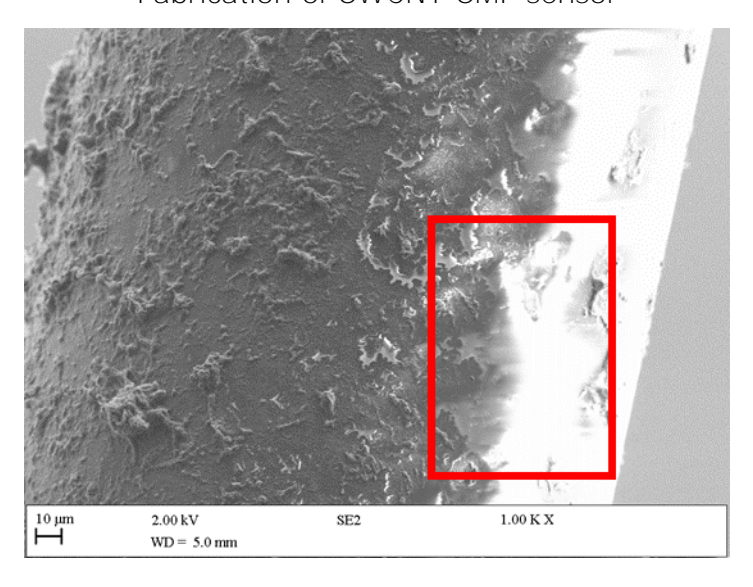
a)



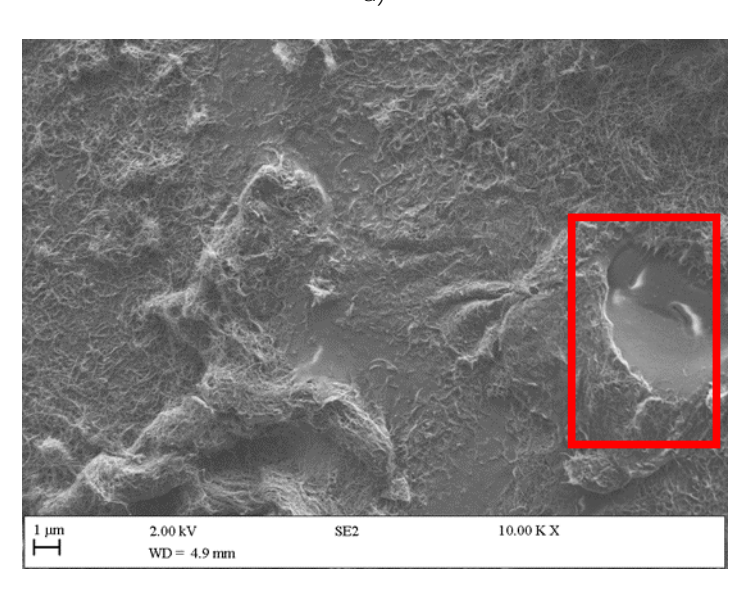
b)

Figure 33 SEM Imagery of a 1cm single coated SMF showing SWCNT deposits and uncoated areas (enclosed by the red outline) at a) 1000x magnification b) 10,000x magnification.

Similarly, for a 3cm length of SWCNT-SMF with a single coating, there are some areas, big and small, that remain uncoated. There are also clumps of SWCNT around various locations of the cladding but it can be confirmed that the SWCNTs have been successfully deposited onto the SMF.



a)



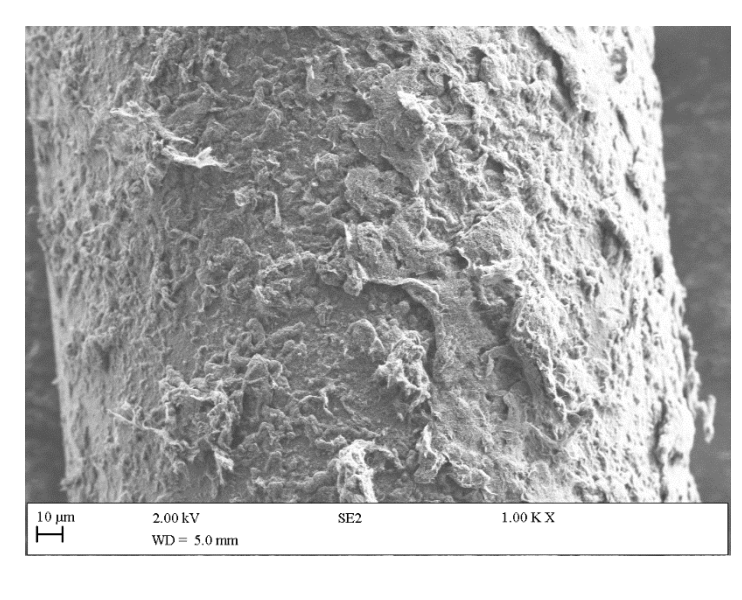
b)

Figure 34 SEM Imagery of a 3cm single coated SMF showing SWCNT deposits and uncoated areas (enclosed by the red outline) at a) 1000x magnification b) 10,000x magnification

5.3.2.2 Double Coated SMFs

For a $1\mu m$ length of SWCNT-SMF with double amount coating applied to, there are no longer any visible areas that can be seen to be uncoated under the SEM as shown in Figure 35. It is obvious that there is no clear uniformity in the coating and there are many visible large concentrations of deposits at various locations with some locations that can be seen to have more layers of SWCNT deposited than other areas. However, the SWCNTs have been successfully deposited and

remain adhered to the fibre and at 10,000x magnification we can successfully see the strands individual strands of SWCNTs.



a)

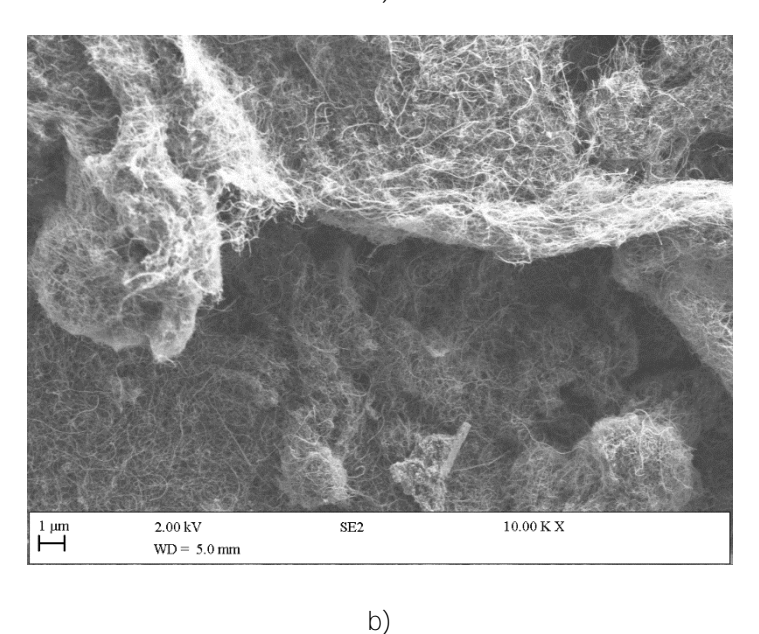
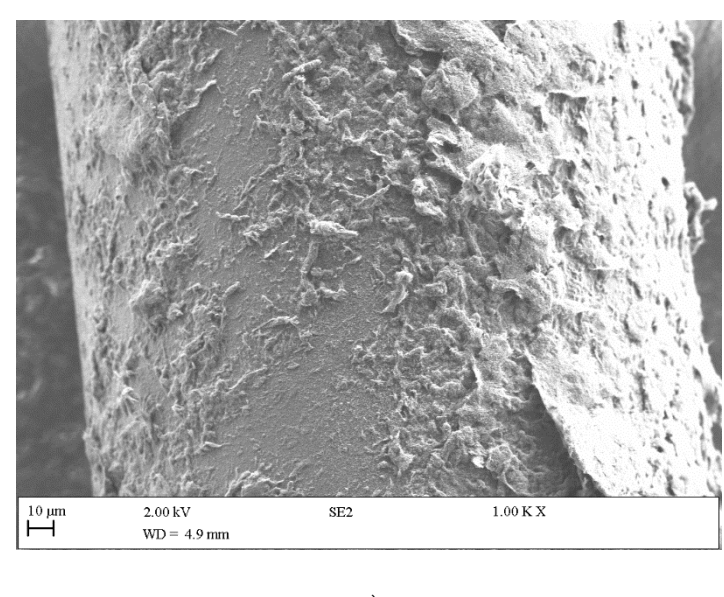


Figure 35 SEM Imagery of a 1µm double coated SMF showing SWCNT deposits at a) 1000x magnification b) 10,000x magnification

Likewise, for a 3cm length of SWCNT-SMF with double layer coating, there are no areas that can be seen to remain uncoated. In addition, there are no uniformity in the coating. As seen in Figure 35a, the right side of the fibre SEM image can be seen to have more SWCNT deposited and other higher concentration SWCNT deposits at various locations around the fibre. However,

Figure 36 confirms the successful deposition and adherence of SWCNTs to the fibre.



a)

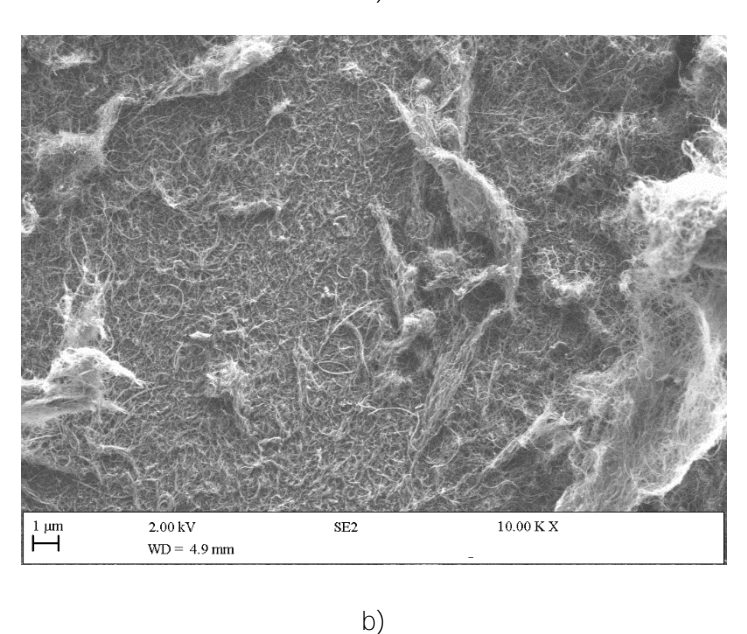
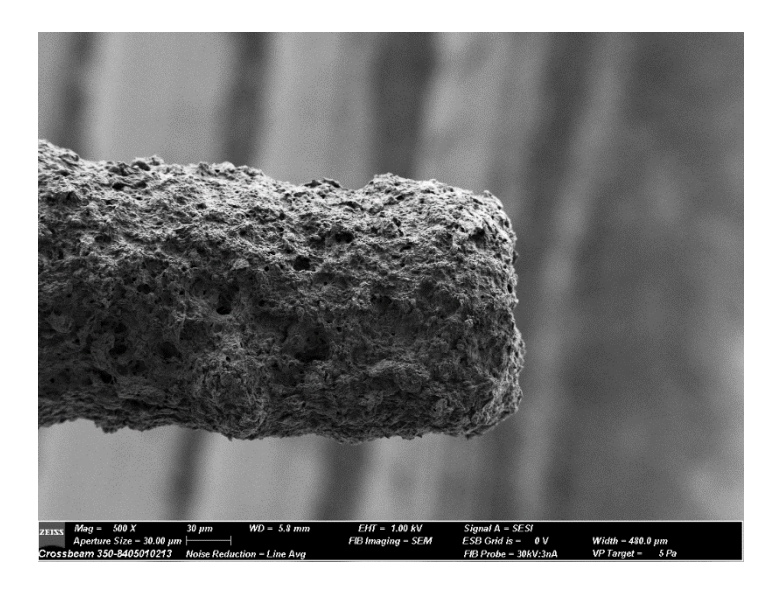


Figure 36 SEM Imagery of a 3μm double coated SMF showing SWCNT deposits at a) 1000x magnification b) 10,000x magnification

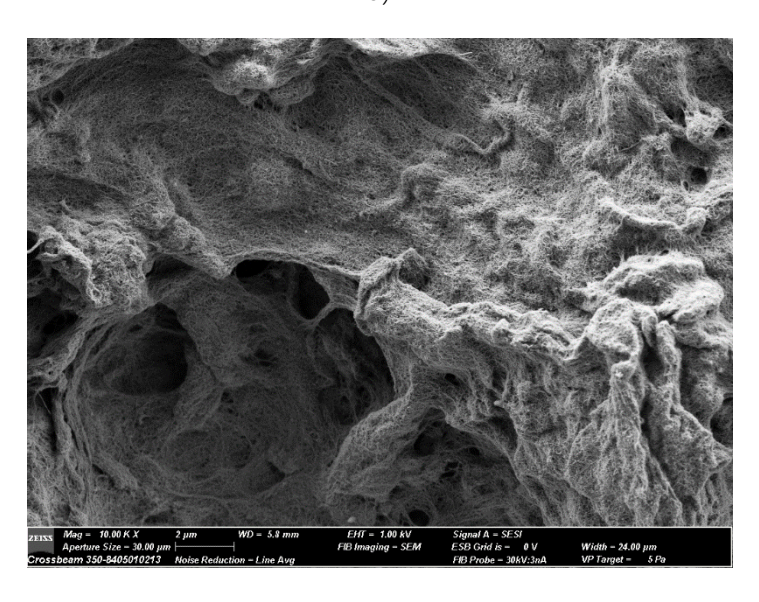
5.3.2.3 Quadruple Coating Layer SMFs

A quadruple coated SMF was fabricated to investigate their properties if an excess amount of SWCNTs were deposited on the SMF. The SWCNT coating shown in Figure 37a can be seen to not be uniform and there are areas of the coating where there are less SWCNT deposited. With such thickness of coating, there

appears to be 'caverns' in the coating which can be more clearly seen at 10,000x magnification in Figure 37b. Despite the non-uniformity and thickness of the coating, the SWCNTs have been successfully deposited and remain adhered to the fibre.



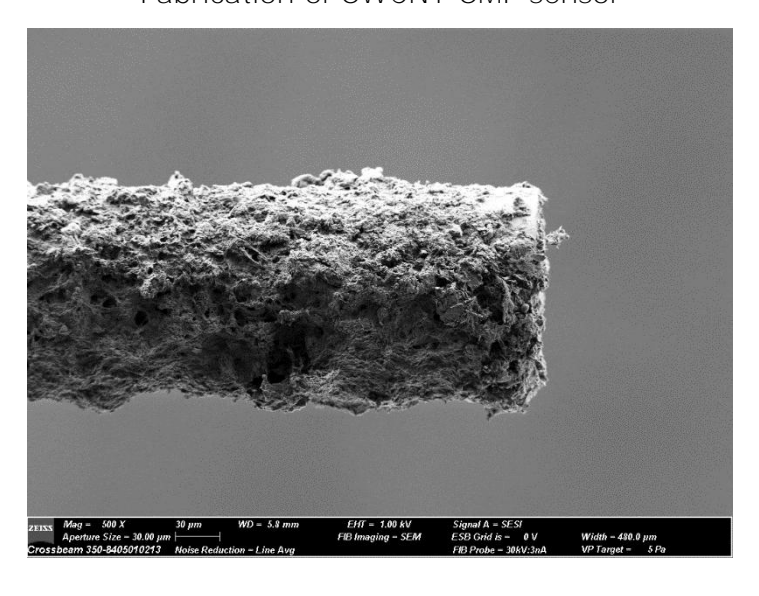
a)



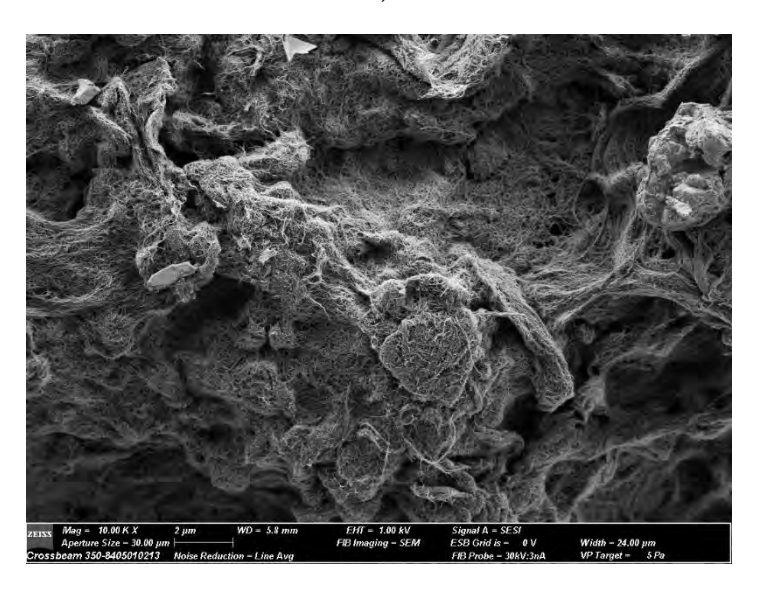
b)

Figure 37 SEM Imagery of a 1cm quadruple coated SMF showing heavy deposits of SWCNTs

Even with a 3cm length of SMF, a quadruple layer of Coating can be seen to be successfully deposited and remains adhered to the SMF as shown in Figure 38. However, it is obvious that there are holes in the coating on the fibre which unfortunately leads to less deposited areas of the fibre at various locations.



a)



b)

Figure 38 SEM Imagery of a 3cm quadruple coated SMF showing heavy deposits of SWCNTs

5.3.3 RI-Sensing of SWCNT-SMF

This section presents the results obtained from the RI sensing experimentation of the fabricated SWCNT-SMF with analysis on repeatability, comparison and discussion.

5.3.3.1 3cm Non-Coated Fibre

To serve as a reference for the SWCNT-SMFs, a 3cm length of uncoated SMF was tested under the RI sensing setup. From Figure 39, it can be seen that there are some changes in the intensity spectra from the spectrometer when the bare SMF is dipped in different concentrations of dextrose solution, with more obvious attenuation band shifts at the response with 0-30% dextrose concentration tests. Most of the intensity spectra peak is found to lie between 1560.552-1577.355nm for all tests. If we take a set of intensity data points situated at 1571.757nm across the different SRI test solutions then we can observe the changes of RI against the intensity spectra as shown in Figure 40.

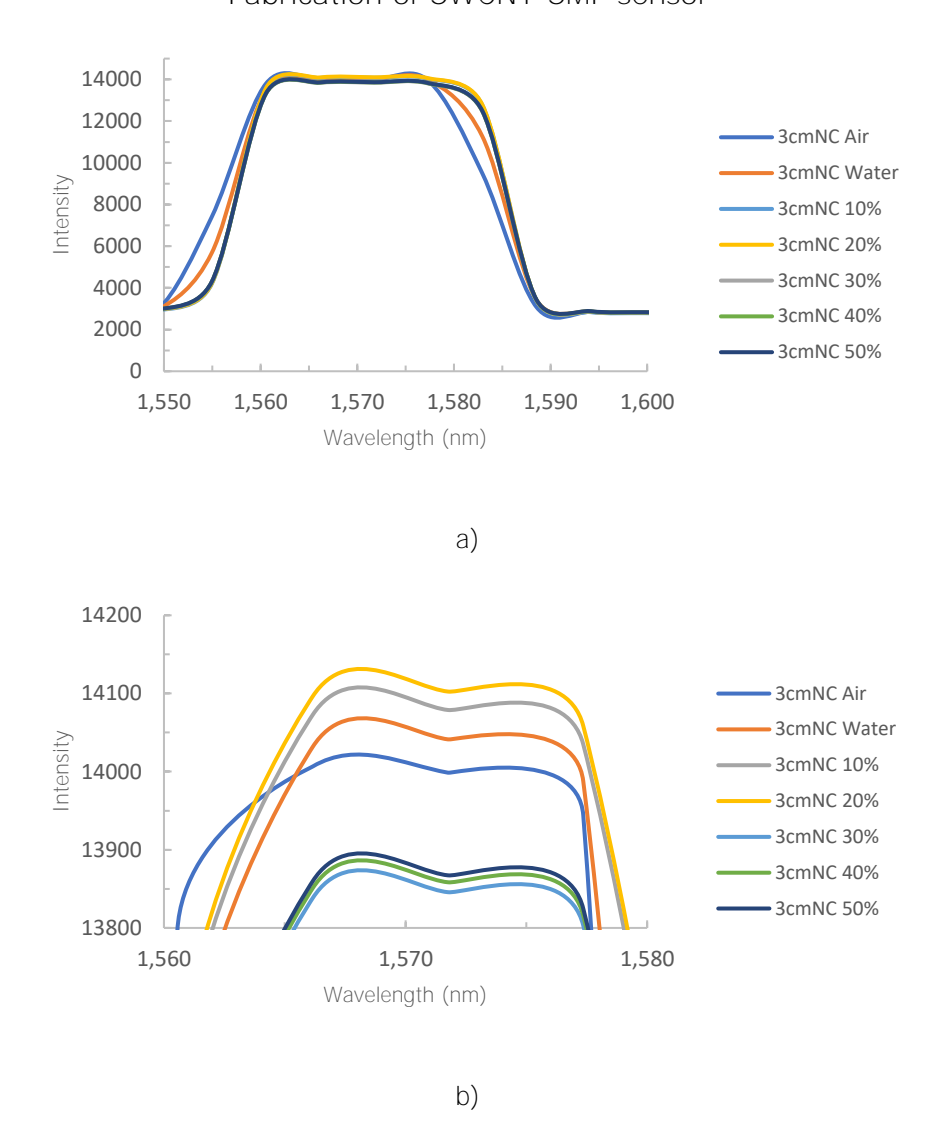
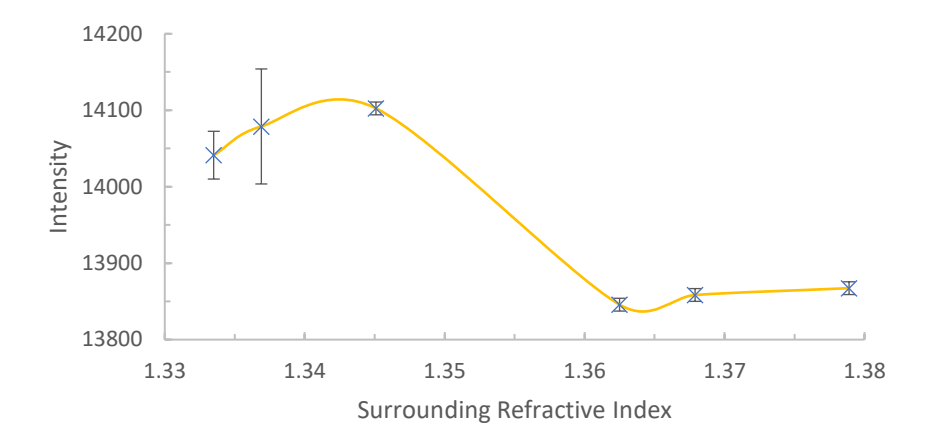


Figure 39 Optical Response from the uncoated SMF when subjected to test solutions of various RIs with a) showing the whole peak b) zoomed into the peak

It can be seen that there are two sets of correlation with the first set found between 1.3335-1.3451RI and the second set of correlation between 1.3625-1.3789RI.

An initial reference spectra was taken based on the ambient air environment and it was found to have an optical power intensity count of 13998.62units. However, it is unexpected that with an increase of SRI from Air to 20% Concentration of Dextrose solution there would be a gain in the response. In addition, it can be noticed that the initial response from Air exhibits a slightly larger bandwidth than the latter results which can be due modal dispersion as the increase in SIR

weakens the light confinement in the fibre. At 1.3451- 1.3625RI, there is also a greater loss of optical power in comparison before a gradual gain is made again at the second set of correlations with the increase of SRI.



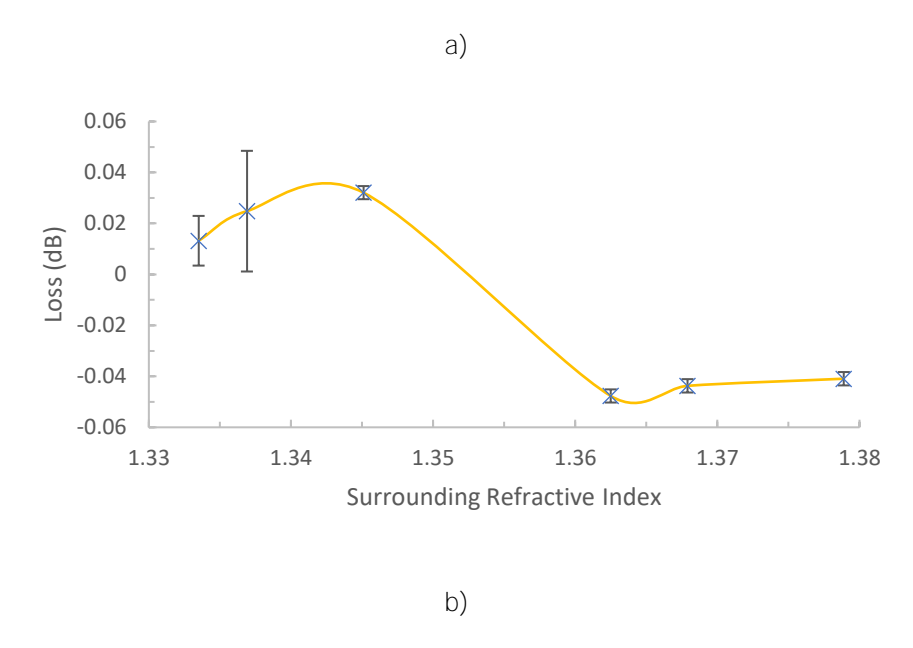


Figure 40 Intensity Response of the non-coated SMF against SRI at the wavelength point of 1571.757nm with error bars based on standard error across 19 samples a) intensity (units) against SRI b) Loss (dB) against SRI

As mentioned in Chapter 4.2 and from simulation, a reason for this can be suggested from the theory of mode transitions where it can occur depending on the effective refractive index and thickness of the surrounding medium around the cladding. Nonetheless, it can be concluded that even for an non-coated exposed cladding SMF, there are both intensity and wavelength modulated spectral response against the change in SRI.

5.3.3.2 1cm Single Coated SWCNT-SMF

The first sample to be tested is a 1cm single coated SWCNT-SMF and it is clear that there is an observable intensity change between the response of the ambient air in comparison to the rest of the test solution as shown in Figure 41. The peak of these responses is found to all lie between a wavelength of 1543.719-1594.128nm.

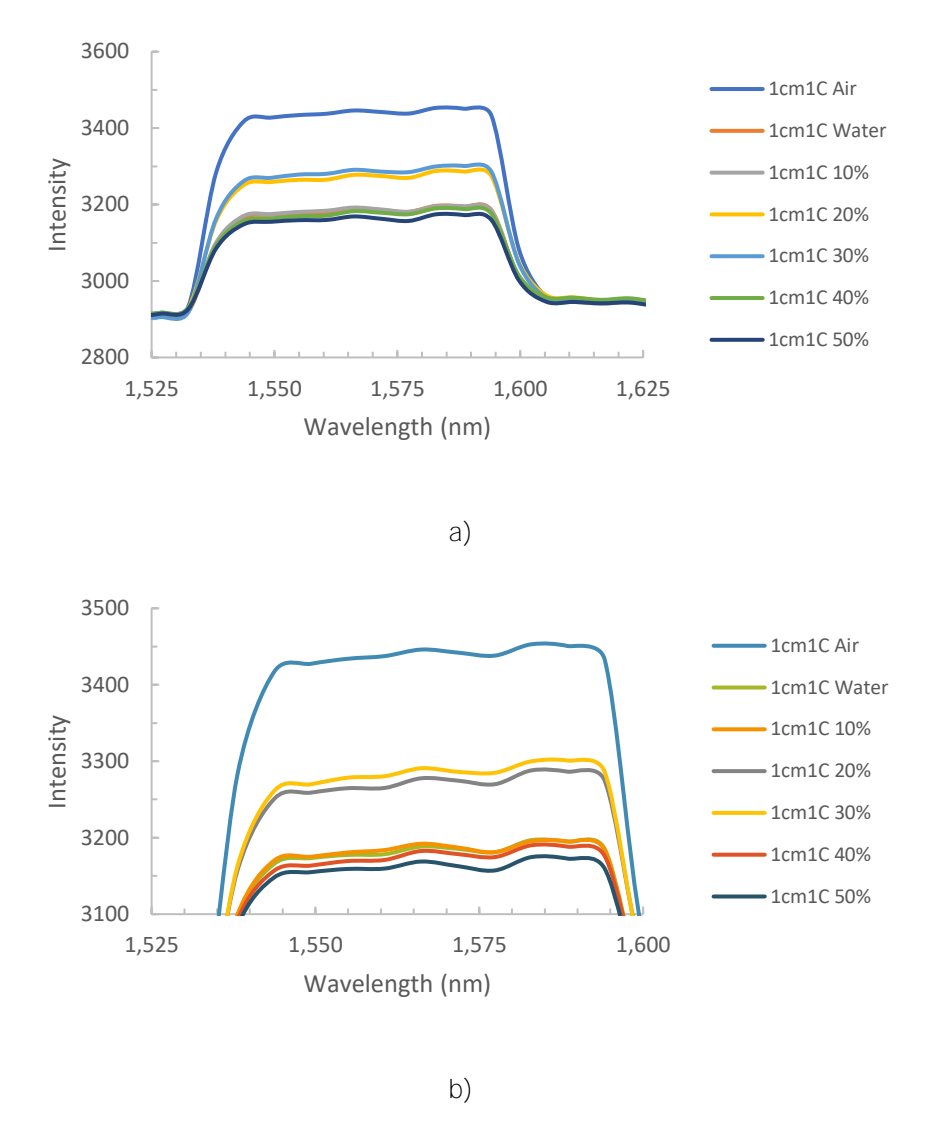
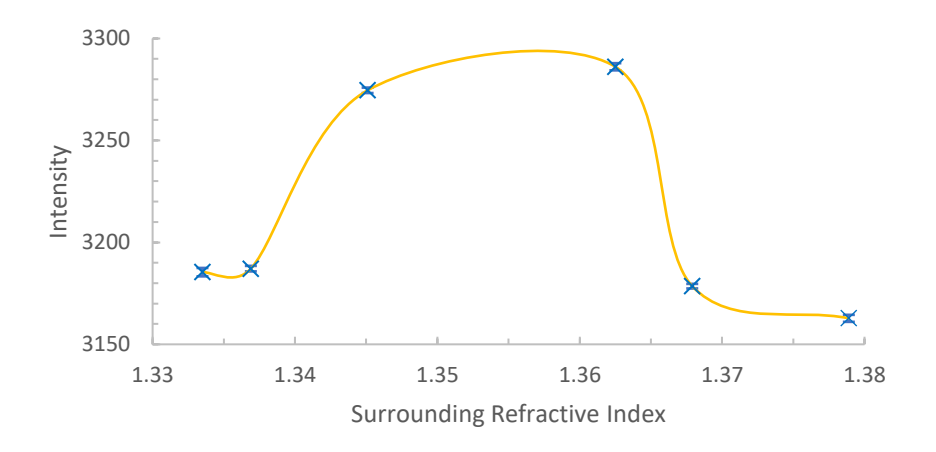


Figure 41 Optical Response from a 1cm single coated SWCNT-SMF when subjected to test solutions of various RIs with a) showing the whole peak b) zoomed into the peak

When subjected to the ambient environment of air, the intensity response is found to be at an initial 3442.01units at 1571.757nm. By taking the intensity data points situated at 1571.757nm across the different RI tests, there seems to be

some sort of non-linear gain initially against the increase in SRI but no clear correlation can be concluded as shown from Figure 42.



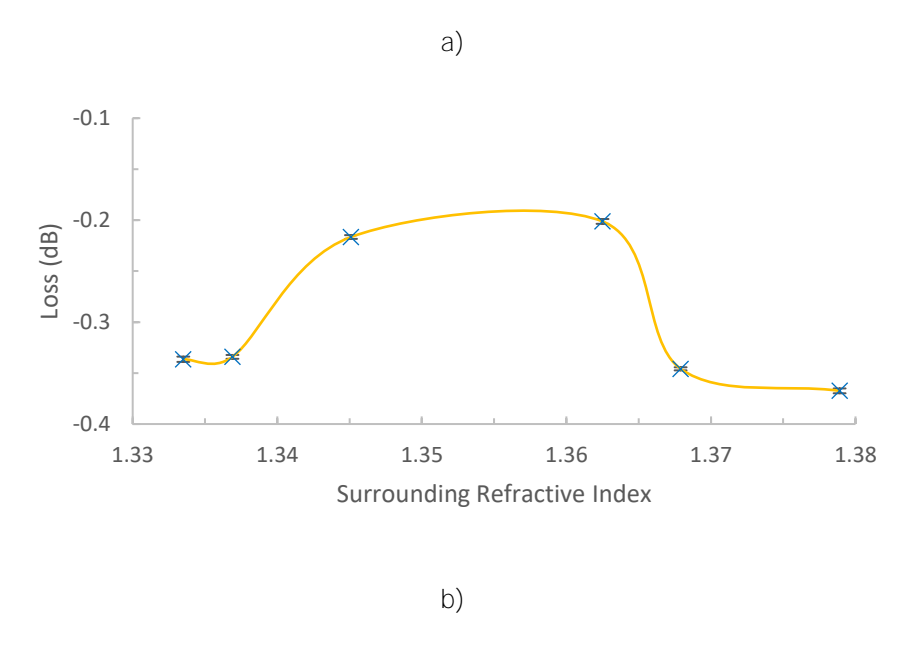


Figure 42 Intensity Response of the 1cm single coated SWCNT-SMF against SRI at the wavelength point of 1571.757nm with error bars based on standard error across 19 samples a) intensity (units) against SRI b)

Loss (dB) against SRI

5.3.3.3 3cm Single Coated SWCNT-SMF

With a 3cm single coated SWCNT-SMF, the effects of the layer of SWCNT is noticeable and there is a notable change in the intensity response between the reference response from air against the rest of the responses as shown in Figure 43a. It can also be seen that the rest of the responses from 0%-50% Dextrose are tightly around each other with some minor changes in their response. All the

peaks of these responses were found to lie between a wavelength of 1543.719-1594.128nm.

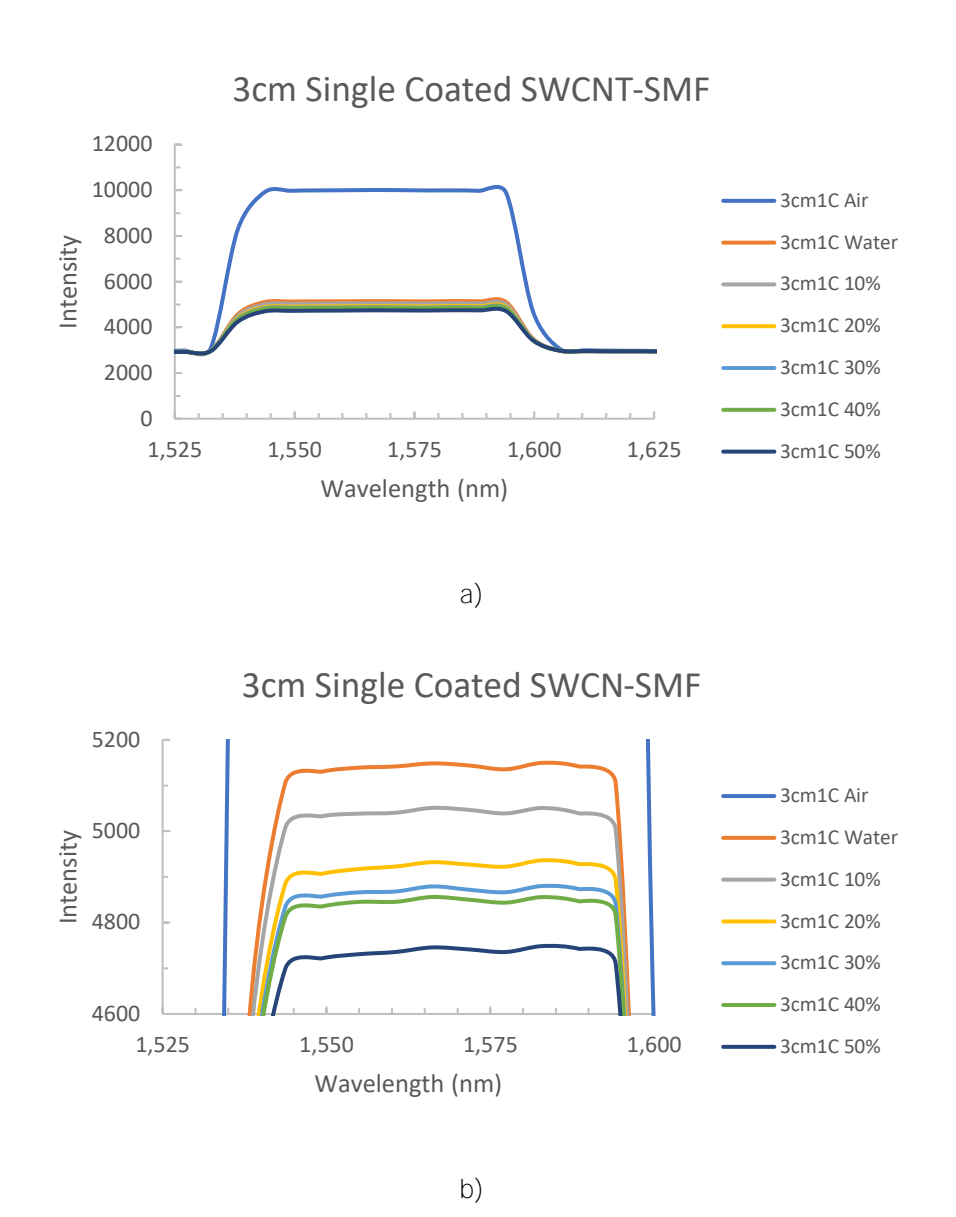
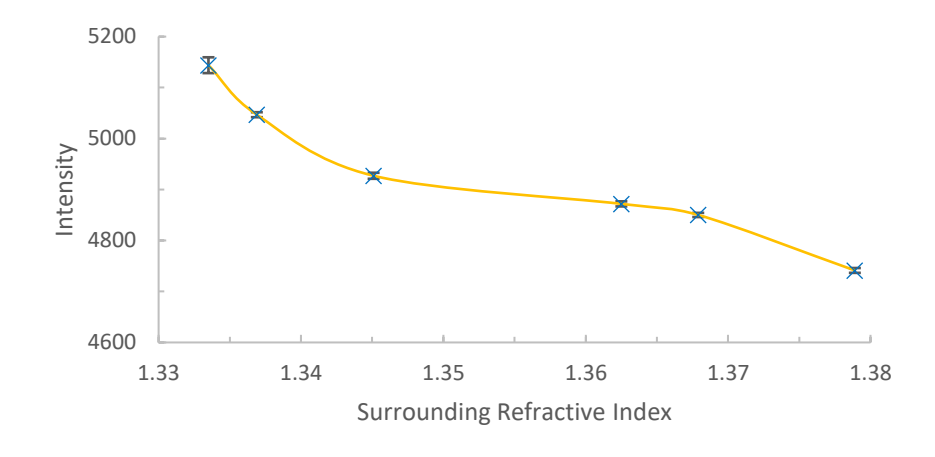


Figure 43 Optical Response from a 3nm single coated SWCNT-SMF when subjected to test solutions of various RIs with a) showing the whole peak b) zoomed into the peaks

If we take a closer look at a specific wavelength of data points at 1571.757nm, the initial reference intensity response of air is found to be 10006.8units as shown in Figure 44. However, once submerged in a 0% Dextrose solution (de-ionised water) there is an immediate 48.6% drop in intensity. From Figure 44b, a correlation can be noticed that with the increase of SRI, there is non-linear loss of intensity from the response of the SWCNT-SMF.



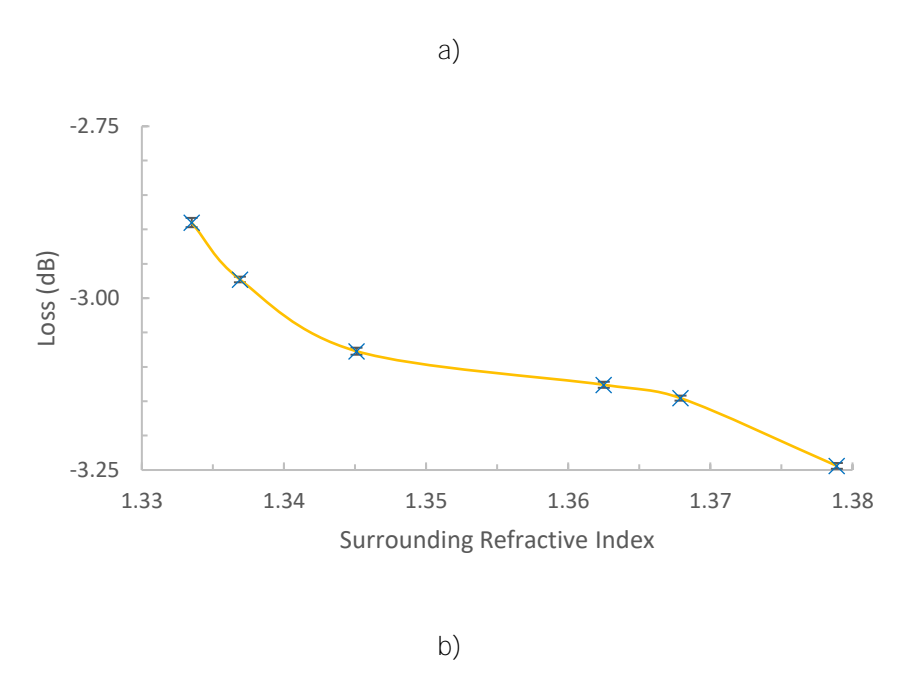


Figure 44 Intensity Response of the 3cm single coated SWCNT-SMF against SRI at the wavelength point of 1571.757nm with error bars based on standard error across 19 samples a) intensity (units) against SRI b)

Loss (dB) against SRI

5.3.3.4 1cm Double Coated SWCNT-SMF

The peaks of the responses for a 1cm double coated SWCNT-SMF were all found to lie between a wavelength of 1543.719-1594.128nm. At a glance, Figure 45a shows some responses to having a significant drop in intensity with the change of SRI but there lies an anomaly in which a 10% dextrose solution seem to lead to a gain in the intensity response against the reference response of air.

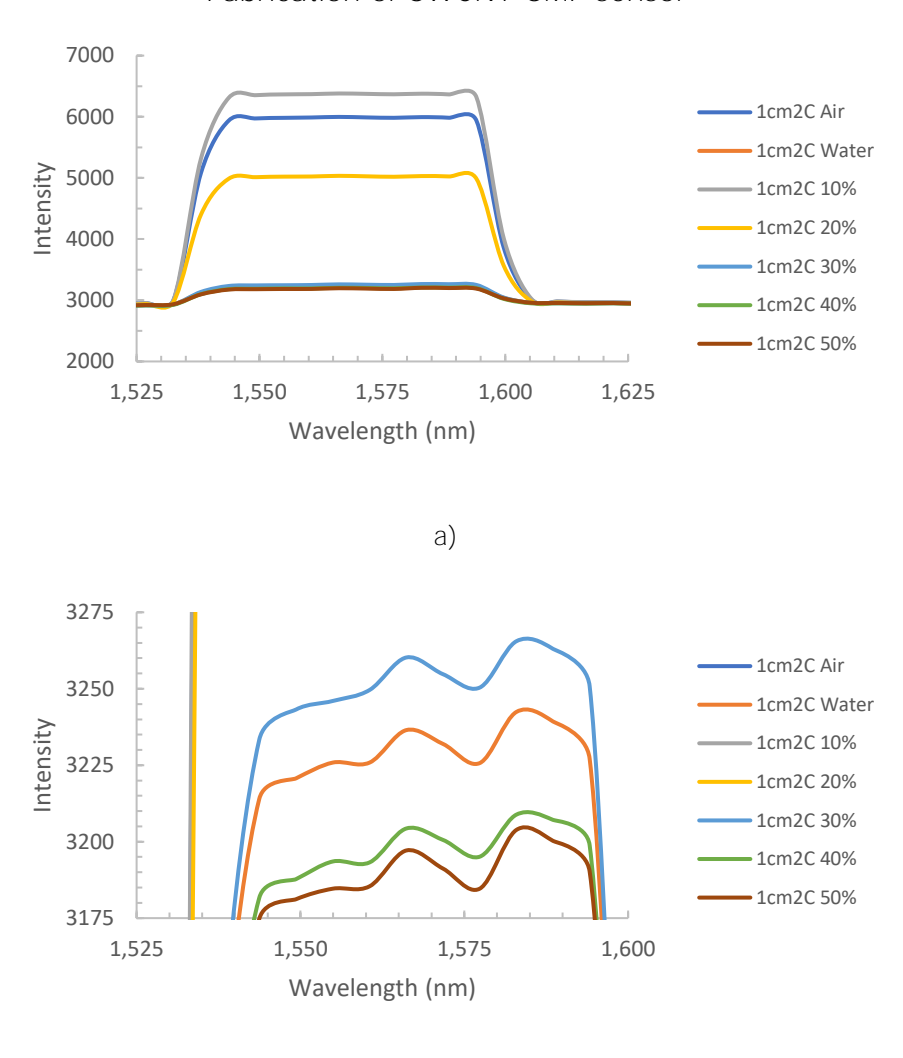
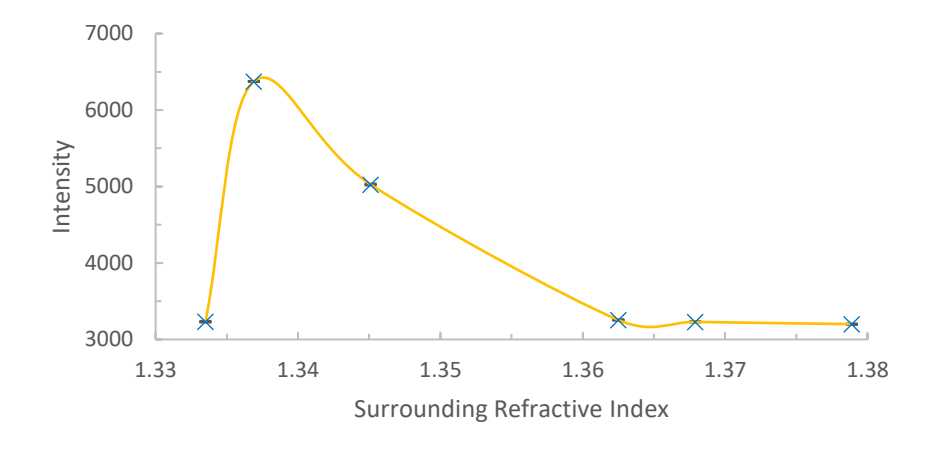


Figure 45 Optical Response from a 1cm double coated SWCNT-SMF when subjected to test solutions of various RIs with a) showing the whole peak b) zoomed into the peak

b)

At the specific wavelength of datapoints at 1571.757nm, the initial reference intensity response of air was 5989.43units. As seen in Figure 46, there is an initial loss in intensity but immediately at a concentration of 10%, there is a massive gain in intensity that exceeds the initial reference intensity from the ambient environment air before. From 10% dextrose concentration onwards, the increase in concentration and RI leads to a non-linear loss of intensity from the SWCNT-SMF.



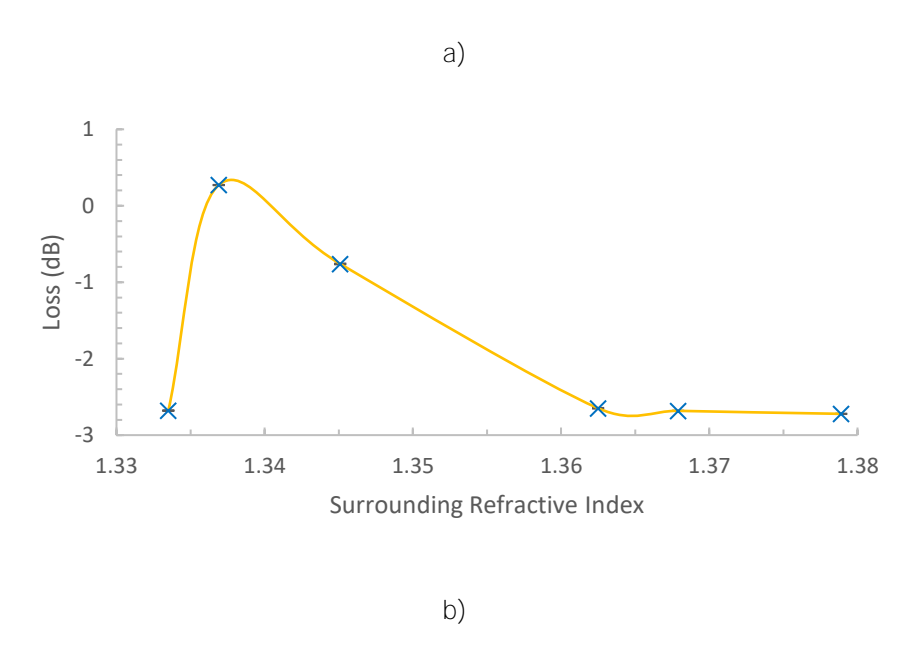


Figure 46 Intensity Response of the 1cm double coated SWCNT-SMF against ERI at the wavelength point of 1571.757nm with error bars based on standard error across 19 samples a) intensity (units) against SRI b) Loss (dB) against SRI

5.3.3.5 3cm Double Coated SWCNT-SMF

For a 3cm double coated SWCNT-SMF, it can be observed immediately from Figure 47a that there is a great amount of intensity change against the change in SRI from the initial reference response of air. There are no anomalies found within this particular set of results and the peaks of all responses were found to lie between wavelength of 1543.719-1594.128nm.

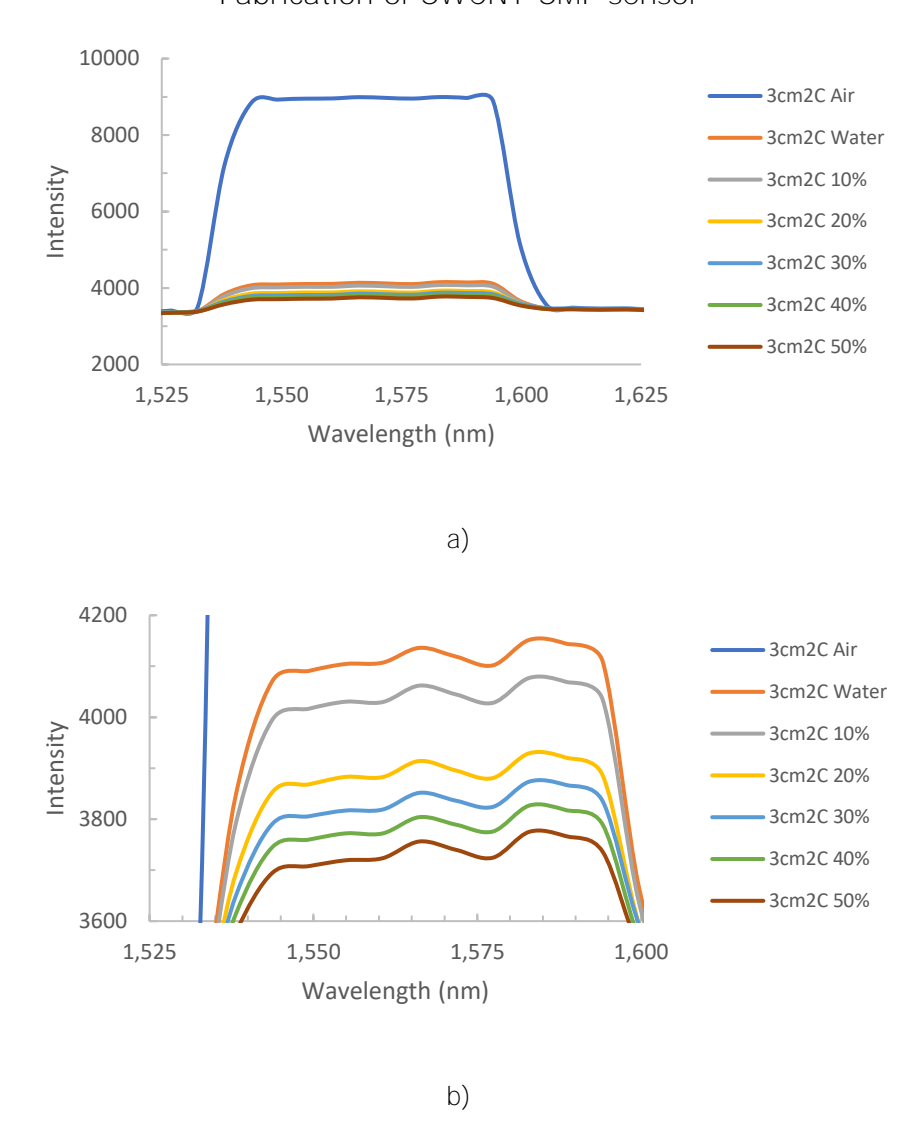
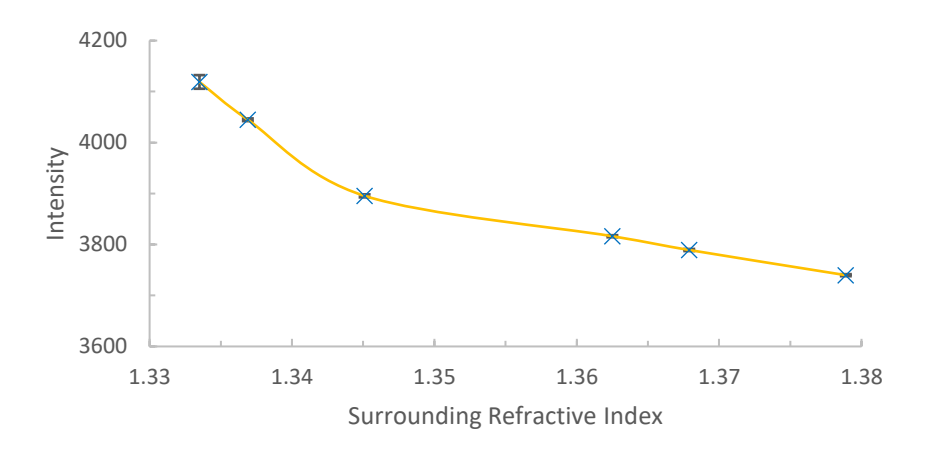


Figure 47 Optical Response from a 3cm double coated SWCNT-SMF when subjected to test solutions of various RIs with a) showing the whole peak b) zoomed into the peak

Taking an in depth analysis of the changes of the peaks at the wavelength of 1571.757nm, the initial intensity response from air as reference was found to have an intensity value of 8972.12units as shown in Figure 48a. Overall, this particular fibre was found to have a non-linear reduction in intensity response with the increase in SRI.



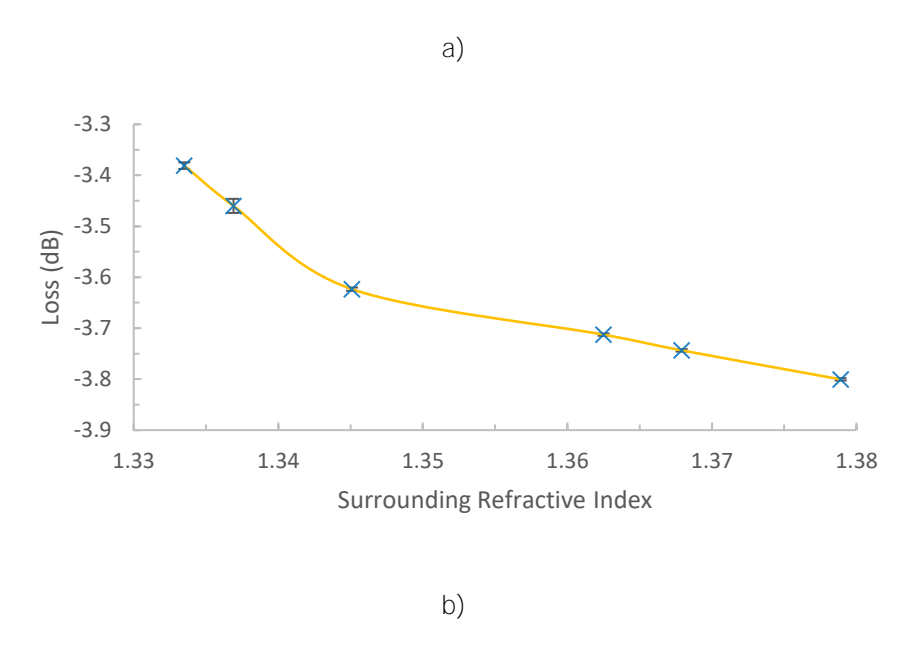


Figure 48 Intensity Response of the 3cm double coated SWCNT-SMF against SRI at the wavelength point of 1571.757nm with error bars based on standard error across 19 samples a) intensity (units) against SRI b) Loss (dB) against SRI

5.3.3.6 Quadruple Coated SWCNT-SMF

For quadruple Coated SWCNT-SMF, it has been found that for both 1cm and 3cm length of coating, no response was obtained across the various concentrations of Dextrose solution nor from the reference air. Figure 49 shows a sample of the static noise level response received from the spectrometer across all test solutions and air for both lengths of quadruple coated SWCNT-SMFs.

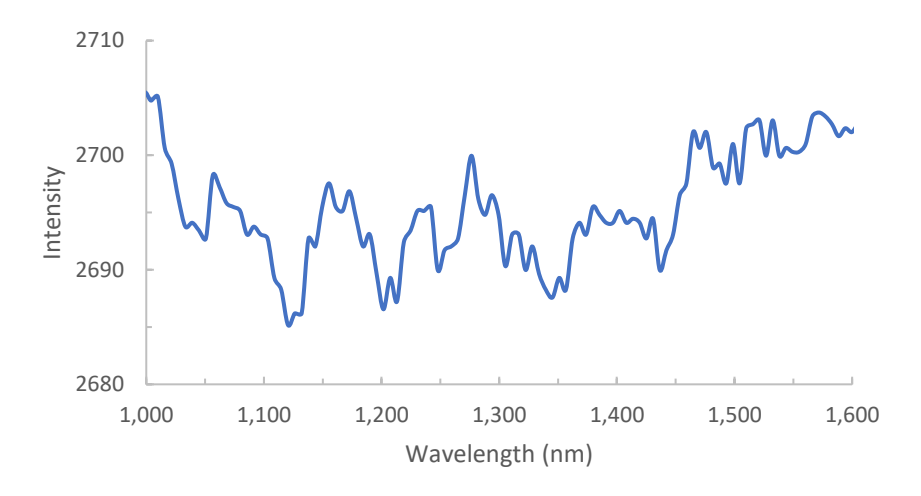


Figure 49 Quadruple coated SWCNT-SMFs demonstrating no response and only background noise

5.3.3.7 Repeatability

To analyse and understand the overall repeatability of the fabrication and tests, 3cm double coated fibres were subjected under the same RI tests with results shown in Figure 50.

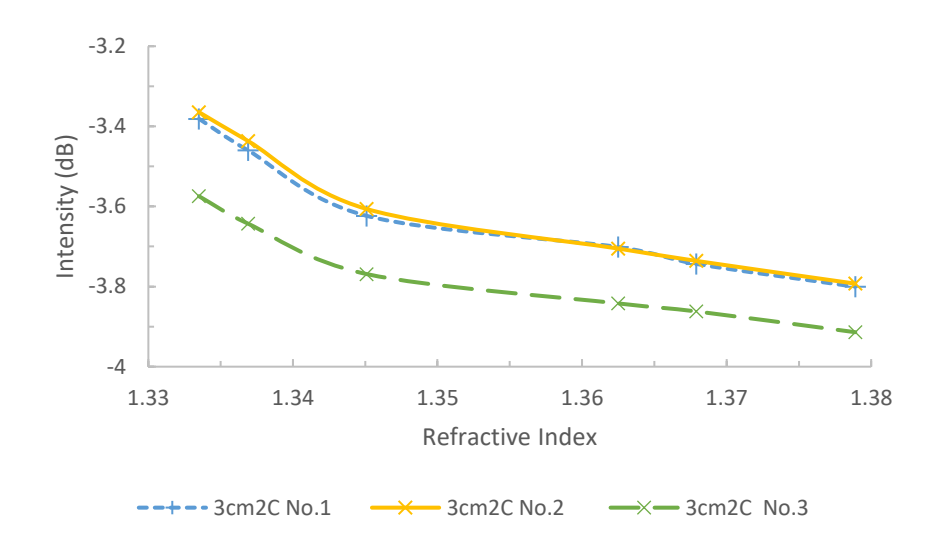


Figure 50 Results depicting repeated RI tests for 3cm Double Coated SWCNT-SMFs

Under similar fabrication parameters and test conditions, it can be seen that fibre No.1 and No.2 show closely related results in comparison to fibre No.3. Fibre No.1 has a sensitivity of approximately -20.886 dB/RIU and -5.236 dB/RIU between the ranges 1.3335-1.3451RI and 1.3451RI-1.3789RI respectively.

Similarly, Fibre No.2 has a sensitivity of approximately -20.842dB/RIU and -5.514dB/RIU between the ranges 1.3335-1.3451RI and 1.3451RI-1.3789RI respectively. Despite similar results observed for No.1 and No.2, it does not necessarily imply that the two fibres have similar coating thickness, coating structure nor uniformity. However, it can suggest that the cumulative effect of the coating and its overall thickness is similar. Hence, it can suggest that Fibre No.3 has greater cumulative effect and thickness which leads to reduced sensitivity in comparison. Fibre No.3 is found to have a reduced sensitivity of approximately -16.755dB/RIU and -5.236dB/RIU between the ranges 1.3335-1.3451RI and 1.3451RI-1.3789RI respectively. Although, the fabrication parameters and conditions are the same but due to the nature of spray coating there are expected inconsistencies in the thickness of the coating across each fabricated SWCNT-SMF. These inconsistencies can lead to greater overall thicknesses that can attenuate the sensitivity as shown in fibre No.3.

The repeated fabrication and their tests do not reflect to be exactly identical, in particularly with fibre No.3. However, all fabricated fibres are able to function effectively with largely similar correlation pattern and sensitivities. Overall, the results suggest good repeatability even with a spray coating methodology.

5.3.3.8 Comparison and Discussion

In this section, the collective performance of the fabricated SWCNT-SMF and uncoated SMF will be put in comparison amongst the simulated LPFG results, other fabricated SWCNT-SMF, and against other novel sensing schemes from existing literatures. By comparing the differences sensors, we can gain insight on the effects of the coating, thickness, length and different sensor systems.

5.3.3.8.1 Uncoated SMF vs Simulated Uncoated LPFG

The initial RI sensing experimentation of a plain uncoated SMF with jacket stripped and cladding exposed has shown results similar to the uncoated LPFG simulated and discussed in Chapter 4.4.1. The response of the uncoated SMF around the 1550 nm wavelength has confirmed intensity and wavelength modulated response variations against the change in SRI. Although there is a large difference in RI between air and water, both intensity response remains locally around a loss of OdB. This suggests that the uncoated SMF is not sensitive to change in SRI. In addition, this factor is particularly more true when put in comparison with the simulated uncoated LPFG. An uncoated SMF is expected to have minimal interactions with the surrounding environment, due to its nature in confining the guided light within the core of the fibre. However, LPFGs behave otherwise, the gratings that induce 'leaky' modes allows greater interactions between the fibre and the surrounding environment. Therefore, although the intensity and wavelength modulated behaviour of the uncoated SMF is found to be similar to the uncoated LPFG in simulation, the sensitivity is significantly lower as expected.

5.3.3.8.2 SWCNT-SMF

With the addition of a single set of SWCNT coating around the SMF the effects of the SWCNTs can immediately be noticed. When the SWCNT-SMF is subjected to varying concentrations of dextrose solution for testing, no wavelength modulations were found between the output spectra of all tests. The intensity modulated aspect remains similar for both single and double coated fibre at all lengths. Furthermore, there is now a discernible amount of intensity change with

the change of SRI from air to water. This change highlights the effects of the SWCNT that enhances interaction between the surrounding environment and their potential for sensitive detection of chemicals. Furthermore, the effects show alignment to the theory of mode transitions discussed in Chapter 4.2, where by depending on the refractive index and thickness of the coating, the cladding modes can 'leak' into the coating for enhanced interactions with the surrounding environment.

The double coated SWCNT-SMFs were found to exhibit even greater intensity drops from the initial air to water test solution. In particular, the fabricated 3cm double coated SWCNT-SMF was found to exhibit a sensitivity of -20.82dB/RIU and -5.24dB/RIU between the RI ranges 1.3335-1.3451RI and 1.3451-1.3789RI respectively.

When the effective RI of the coating and thickness of the coating far exceeds the evanescent field penetration depth, the field cannot effectively interact with the surrounding environment beyond the coating. In some cases, the evanescent field may only interact with the excess coating material itself. As shown from a quadruple coated SWCNT-SMF, there is an upper limitation in the coating thickness, in which an over-coated fibre can lead to no response and the sensor failing.

The effects of the SWCNT coating can be observed even at a small coating length of 1cm around the cladding of the SMF where there is an discernible amount of intensity change from air to water. Despite such sensitivity, there are some instabilities observed in the results for a short SWCNT coating length of 1cm. As mentioned in Chapter 3.4, the overall performance of a coated evanescent field

sensor is dependent on the cumulative interaction effects of the SWCNT coating. With the spray coating methodology adopted, the instabilities in the correlation can arise due to non-uniform deposition of SWCNT. At such short lengths of SWCNT coatings, any inconsistencies can dominate the response of the sensor and lead to more noticeable effects from mode transitions which disrupts the correlations in the results. However, at an increased SWCNT coating length of 3cm, which may not always be true, the sudden inconsistencies have a greater chance of being mediated by the longer length of consistent coating. Thus, the fabricated 3cm double coated SWCNT-SMF have no sudden large gains nor losses observed.

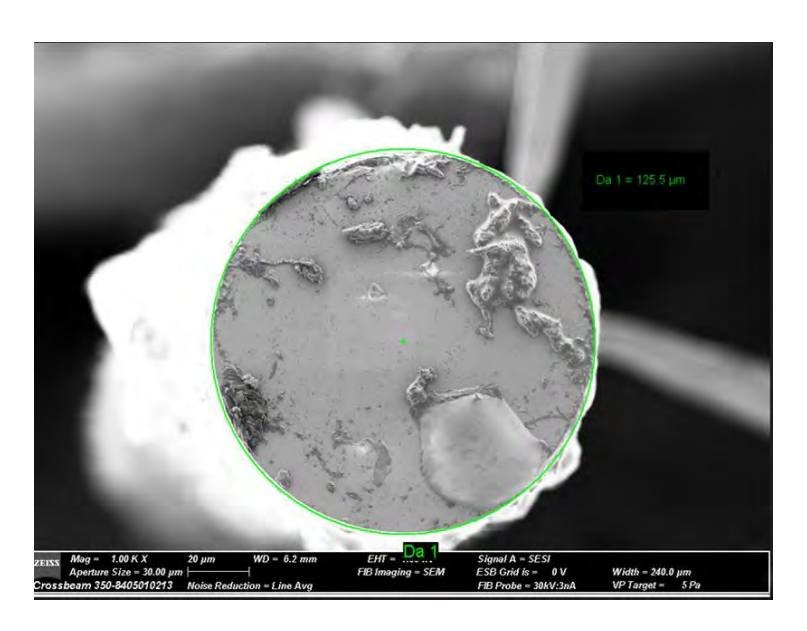


Figure 51 SEM imagery of the 3cm double coated SWCNT-SMF cross-section showing an approximate 0.5 μ m thick SWCNT coating around the 125 \pm 0.7 μ m cladding diameter of the SMF-28

From Figure 51, we can see that there is an approximate SWCNT coating thickness of 0.5 µm. This is an approximation to the thickness of the coating, as at certain areas down the length of fibre, the coating thickness can suddenly exceed 0.5 µm with some areas also less than that. However, despite the non-unform coating, the 3 cm double coated SWCNT-SMF has demonstrated the sensitive detection of varying dextrose concentrations. This can suggest that the

effects from the non-uniform spray coating can be offset through greater lengths of SWCNT-coating due to the increased cumulative effects from the overall coating.

Overall, amongst the fabricated SWCNT-SMF, the 3cm double coated SWCNT-SMF has demonstrated the most excellent characteristics for chemical detection based on SRI changes.

5.3.3.8.3 3cm Double Coated SWCNT-SMF vs Simulation

From all the fabricated fibre, a 3cm doubled coated SWCNT-SMF demonstrates the most enhanced and most stable correlation in intensity change against the change in RI from the test solutions. The 3cm doubled coated SWCNT-SMF is found to have an approximate thickness of $0.5\mu m$ and exhibit an approximate sensitivity of $20.886\,dB/RIU$ and $5.236\,dB/RIU$ between the ranges 1.3335-1.3451RI and 1.3451RI-1.3789RI respectively. This is slightly greater than the simulated 1.70RI $0.5\mu m$ LPFG from Chapter 4.4.2.3 with a sensitivity of approximately 3.4571dB/RIU for the ranges 1.33-1.44RI but significantly less than the simulated 1.60RI $0.50\mu m$ LPFG from Chapter 4.4.2.2 with a sensitivity of approximately 119.73dB/RIU for the same ranges.

1.70RI to have gradually attenuated sensitivity of lower dB/RIU ranges.

Therefore, it is likely that the effective refractive index of the SWCNT coating on the fabricated 3cm double coated SWCNT-SMF to fall within the ranges of 1.60-1.70RI. The primary remaining factor that can lead to the difference in sensitivity is the presence of a LPFG in the simulation that enhances the evanescent field.

In addition, the length of the simulated LPFG was 9cm compared to the 1cm and 3cm lengths of the fabricated SWCNT-SMF. Longer lengths of coating can have varying effects between the evanescent field and the cumulative effects coating which can lead to further differences in sensitivity.

5.3.3.8.4 3cm Double Coated SWCNT-SMF vs Literature.

In comparison with similar Optical fibre sensors, a previous paper on a fabricated CNT deposited LPFG has reported to achieved an approximate sensitivity of 31 dB/RIU and 47 dB/RIU for the ranges 1.33-1.38RI and 1.38-1.42RI respectively (Tan et al., 2014a), which is significant greater amount of sensitivity than our fabricated 3cm SWCNT-SMF. The fundamental purpose of an SMF is just to transmit light over long distances with minimal loss and dispersion quite. In contrast, the purpose of LPFGs is to couple light from the core mode of an optical fibre to its cladding mode to enable sensitive sensing. With the sensitivity enhancements from both the LPFGs and a CNT coating, it is expected that a CNT deposited LPFG would provide greater sensitivity than our fabricated SWCNT-SMF. This contrast would be similar to the Layer-by-layer assembly of polyelectrolytes-wrapped multi-walled carbon nanotubes on long period fibre grating sensors (Ni et al., 2019) which was found to exhibit a greater sensitivity of 103dB/RIU for the ranges 1.37-1.43RI.

In an alternative approach to RI sensing, a graphene-deposited photonic crystal fibre in a fibre-based Mach-Zehnder Interferometer has reported to exhibit a sensitivity similar to our fabricated SWCNT-SMF of approximately 9.4dB/RIU and 17.5dB/RIU for the ranges 1.33-1.38RI and 1.38-1.43RI respectively (Tan et al., 2015). However, it should be noted that for this approach, the intensity variation

from the output spectra was taken from an interference dip at 1577.68 nm without regards to the wavelength shift that were present.

5.4 Limitations

This research has taken a simple yet cost effective approach with high production scalability towards the fabrication of a SWCNT-SMF for sensing applications. There are some limitations that can be identified from the preparation of the fibre, to the synthesis of solution, the spray coating and the RI sensing equipment assembly. The first limitation lies in the preparation process of the SMF where the outer jacket was removed with a standard mechanical three hole fibre stripper. Although these strippers are widely used for their straightforward consistent operations, the stripping quality is highly dependent on the operator's skill and applying incorrect pressure can damage the fibre. Due to the damages being unnoticeable to the naked eye when stripping the jacket, the fragility of the damaged fibre surfaces during the coating stages when they break under the air pressure of the depositing spray gun. An alternative to this tool could be the use of thermal strippers in which they soften the jacket with heat provide uniform stripping of the jacket with less requirement on the manual effort of the operator. The spray coating methodology is based on short burst depositions of SWCNT solution along with rapid evaporation of the DIW base solution to quickly adhere the SWCNTs around the cladding of the fibre. As the SWCNTs are randomly deposited without alignment through a spray gun nozzle, it is unavoidable that there is minimal control over the deposition volume and thickness of SWCNT. The short burst deposition of the SWCNT is manually controlled and timed with a stop

watch which can cause minor variations to the actual coated time. Electronically timed and activated spray gun system can be implemented to increase the overall accuracies in the spray coating duration. In cohesion with the theory of cumulative effects in evanescent field sensor, a greater tolerance in the non-uniform coating has been allowed. However, if greater uniformity coatings can be achieved, it can provide further in depth insights to the effects from varying precise thickness of coatings.

In the design of our sensor system for this research, we have chosen to utilise a temporal connector to integrate the fabricated SWCNT-SMF. The use of a temporal connector was to provide quick and simple integration of the fabricated SWCNT-SMF without the need of epoxy and polishing. In addition, they could be constantly reused with various other fabricated SWCNT-SMF to ensure cost effective experimentations. As a result, they create higher insertion losses and are more sensitive to the environmental conditions. Furthermore, in the RI sensing experimentation, it has caused some mild disconnection throughout the continuous monitoring of the test solutions due to loose alignments and fibre tensions. However, this would not be the case for most industrial and commercial Optical fibre systems as a fixed fibre connector would be utilised instead.

5.5 Summary

In this chapter, the theoretical concept from Chapters 2 and 3 is used to fabricate a SWCNT-SMF chemical sensor to detect varying concentrations of dextrose solution based on RI changes with real-time continuous monitoring capabilities

Initially, two sets of SWCNT solutions, with and without dispersant was investigated to ensure the uniform dispersion of CNTs with stability over time whilst also meeting the requirements restricted by the spray gun. A SWCNT concentration of 0.00025% with dispersant was found to fit the requirements of the coating setup and was used for the latter stages. The chosen SWCNT solution was then deposited under three different amounts of coatings at coating lengths of 1cm and 3cm to assess the effects. The dextrose concentration tests has confirmed the enhancements can made through the deposition of SWCNTs with upper enhancement limitations restricted by an excess of coating. In particular, a 3cm double coated SWCNT-SMF has demonstrated the most stable correlation between the intensity response of the spectrometer and the change in RI/dextrose concentration which further suggests that, an optimal coating thickness and length can be found.

In conclusion, SWCNT-SMFs with a selective variation of coating parameters was successfully fabricated and investigated. The fabricated SWCNTs has confirmed intensity modulated RI sensing capabilities with enhanced optical interactions without the presence of wavelengths shifts in the output spectra. In addition, for all variations of SWCNT-SMF, measurements could be made monitored continuously and instantaneously in real-time with the SWCNT-SMFs recovering in air at room temperature within 10seconds after being dipped into de-ionized water for cleansing.

6 CONCLUSION AND FURTHER WORKS

Real-time and accurate measurements are key factors in chemical sensor designs. The research presented by this thesis has performed simulations and experimental work as a proof of concept for a SWCNT-SMF for chemical detection based on RI variations. The novelty and importance of this research have been introduced and detailed. This chapter concludes this thesis with various potential future research work outlined.

6.1 Conclusion

This thesis has demonstrated a clear proof-of-concept for intensity modulated SWCNT-SMF sensors with real-time continuous monitoring capabilities for chemical detection utilising simplistic, cost effective yet reproducible methodologies without speciality fibres. By avoiding complex wavelength-shift

Conclusion and Further works

analysis, instantaneous response and rapid recovery is realized, the research lays the groundwork for a chemical sensor platform that can be integrated into existing optical networks for remote detections with functionalisation and multiplexing capabilities.

The simulation studies in Chapter 4 has verified RI sensing capabilities through intensity modulated behaviour without any wavelength shifts through the application of a coating above 1.60RI. The results suggests that a 0.5μm CNT coating with RI between 1.60-1.70RI would offer a maximal sensitivity for detecting a SRI range between 1.30-1.44RI. Chapter 5 applies the theoretical expectations of the CNT coating onto a SMF. A stabilized 0.00025% (w/w) SWCNT coating solution was developed to allow for the deposition on bare SMFs. Amongst all variants of fabricated SWCNT-SMFs, the 3cm double coated SWCNT-SMF has demonstrated the most excellent performance with 20.886dB/RIU and 5.236 dB/RIU between the ranges 1.3335-1.3451RI and 1.3451RI-1.3789RI respectively. Furthermore, across all trials, the SWCNT-SMFs have shown instantaneous response to liquid RI changes with baseline recovery to air within 10seconds after rinsing. The fabricated 3cm double coated SWCNT has been characterized with coating thickness closely matching to the simulated parameters which has shown highly detectable and repeatable correlations with SRI changes. Given the intensity modulated nature of the sensor and its application, environmental factors such as temperature and pressure would have insignificant effect on the effective RIs of the optic fibre and the sensor's performance.

Conclusion and Further works

By demonstrating intensity modulated behaviour, this thesis has eliminated the need for speciality fibres, spectrally resolved detection methodologies and more complex computational requirements, paving the way for a passive, band-pass-filter read out systems. The spray-coating methodology developed requires minimal specialized equipment whilst fabricating reproducible CNT coatings, making it accessible to a wide range of laboratories of all sizes. Moreover, the CNT layer can be functionalized with receptor molecules whereby the same platform can be tailored to selectively detect a large range of chemicals and industrial pollutants at various locations. Thus, the overall sensor platform can offer a versatile toolkit for multiplexed sensing networks free from electromagnetic interferences.

6.2 Further Works

This section discusses the possible future research and developments of CNT optical fibre sensors. This includes branching further based on existing work or building and scaling up the present sensor design.

6.2.1 Future Research

The research conducted so far has provided a robust framework for CNT optical fibre sensors. To develop the current portable sensor design, functionalisation of the CNT solutions can allow specific analyte CNT Fibres to be fabricated for selective chemical detection which is the core motivation of this thesis. The CNTs can be functionalized with carboxylic acid groups (CNT-COOH). In such a form, the CNT-COOH can then coordinate the metalloporphyrins to form a square pyramidal metal complex where a vacant site is opened for the acceptance of

Conclusion and Further works

chemicals allowing the sensing capabilities. In addition, the porphyrin ring can be modified to achieve different selectivity. With the functionalisation, further tests can be experimented with the functionalized CNT fibres tested under various liquid conditions and ultimately gaseous conditions can be made possible.

The fibre base used in Chapter 4 was an SMF due to the simplicity, however, for optimization and enhancements the fibre base can explore a single point invasive LPFG setup. In addition, further fibre platforms such as Fibre Bragg Gratings, Photonic Crystal Fibres, Side-polish Fibres etc. can be further explored for their individual advantageous properties.

To branch out the existing methodologies in the fabrication of CNT fibres, more controlled deposition of CNTs can be explored with chemical vapour deposition of the CNTs. With greater control, optimum coating thickness can be achieved for more enhanced optical properties and stable correlations between SRI and analyte concentrations. For greater novelty, vertically aligned CNT deposited fibres can be explored for any enhancements to the optical sensitivities. Ultimately, the design can be scaled up and integrated into a multi-channel system where multiple analytes can be remotely monitored in real-time continuously.

6.3 Summary

Overall, the aims and objectives is achieved in fabricating a sensor for liquid contaminants with sensitivities of around 20.886 dB/RIU and 5.26 dB/RIU between the ranges 1.3335-1.3451RI and 1.3451RI-1.3789RI respectively. Ultimately, the design can be functionalised, scaled up and integrated into a

Conclusion and Further works

multi-channel system where multiple selective analytes can be remotely monitored in real-time continuously.

7 REFERENCES

Abdel-Karim, R. (2024) 'Nanotechnology-enabled biosensors: a review of fundamentals, materials, applications, challenges, and future scope.' *Biomedical Materials & Devices*, 2(2) pp. 759-777.

Abeywardena, C., Zhang, Q., Korposh, S., Morgan, S., Bull, S. and Correia, R. (2024) 'Highly sensitive optical fibre Bragg grating contact pressure sensor embedded in a polymer layer: Modelling and experimental validation.' *Results in Optics*, 14 p. 100604.

Acharya, A. and Kogure, T. (2024) 'Advances in fibre-optic-based slope reinforcement monitoring: A review.' *Journal of Rock Mechanics and Geotechnical Engineering*,

Adam, J.-L. and Zhang, X. (2014) *Chalcogenide glasses: preparation, properties and applications.* Woodhead publishing.

Ahmed, U., Mumtaz, R., Anwar, H., Mumtaz, S. and Qamar, A. M. (2020) 'Water quality monitoring: from conventional to emerging technologies.' *Water Supply*, 20(1) pp. 28-45.

Ahsani, V., Ahmed, F., Jun, M. B. and Bradley, C. (2019) 'Tapered fiber-optic Mach-Zehnder interferometer for ultra-high sensitivity measurement of refractive index.' *Sensors*, 19(7) p. 1652.

- Al-Azzawi, A. (2017) Fiber optics: principles and practices. CRC Press.
- Al-Sanea, M. M. and Gamal, M. (2022) 'Critical analytical review: Rare and recent applications of refractive index detector in HPLC chromatographic drug analysis.' *Microchemical Journal*, 178 p. 107339.
- Alam, S. N., Sharma, N. and Kumar, L. (2017) 'Synthesis of graphene oxide (GO) by modified hummers method and its thermal reduction to obtain reduced graphene oxide (rGO).' *Graphene*, 6(1) pp. 1-18.
- Alhussein, A. N., Qaid, M. R., Agliullin, T., Valeev, B., Morozov, O. and Sakhabutdinov, A. (2025) 'Fiber Bragg Grating Sensors: Design, Applications, and Comparison with Other Sensing Technologies.' *Sensors*, 25(7) p. 2289.
- Ali, A. H. (2022) 'High-performance liquid chromatography (HPLC): A review.' *Annals of advances in chemistry*, 6(1) pp. 010-020.
- Ali, N. M., Khan, M. K., Mazhar, B. and Mustafa, M. (2025) 'Impact of Water Pollution on Waterborne Infections: Emphasizing Microbial Contamination and Associated Health Hazards in Humans.' *Discover Water*, 5(1) p. 19.
- Ameen, S. S. M., Omer, K. M., Mansour, F. R., Bedair, A. and Hamed, M. (2025) 'Non-invasive wearable electrochemical sensors for continuous glucose monitoring.' *Electrochemistry Communications*, p. 107894.
- Anjana, K., Herath, M. and Epaarachchi, J. (2024) 'Optical fibre sensors for geohazard monitoring—A review.' *Measurement*, p. 114846.
- Anjana, K., Herath, M., Epaarachchi, J. and Priyankara, N. H. (2025) 'Development of an optical fibre sensor system for ground displacement and pore water pressure monitoring.' *Measurement*, p. 117770.
- Ara, A. and Usmani, J. A. (2015) 'Lead toxicity: a review.' *Interdisciplinary toxicology*, 8(2) p. 55.
- Ayanda, O. S., Mmuoegbulam, A. O., Okezie, O., Durumin Iya, N. I., Mohammed, S. a. E., James, P. H., Muhammad, A. B., Unimke, A. A., et al. (2024) 'Recent progress in carbon-based nanomaterials: critical review.' *Journal of Nanoparticle Research*, 26(5) p. 106.

Baracu, A. M. and Gugoasa, L. A. D. (2021) 'Recent advances in microfabrication, design and applications of amperometric sensors and biosensors.' *Journal of The Electrochemical Society*, 168(3) p. 037503.

BASHARAT, R., KOTRA, V., LEAN, Y. L., MATHEWS, A., KANAKAL, M., DEVI, C. B. P., NYAMATHULLA, S., VARALA, R., et al. (2021) 'Ultra Performance Liquid Chromatography (Mini-Review).' *Oriental Journal of Chemistry*, 37(4)

Berkel, C. and Özbek, O. (2024) 'Green electrochemical sensors, their applications and greenness metrics used: A review.' *Electroanalysis*, 36(11) p. e202400286.

Bochynska, S., Duszewska, A., Maciejewska-Jeske, M., Wrona, M., Szeliga, A., Budzik, M., Szczesnowicz, A., Bala, G., et al. (2024) 'The impact of water pollution on the health of older people.' *Maturitas*, 185 p. 107981.

Bollella, P., Fusco, G., Tortolini, C., Sanzò, G., Favero, G., Gorton, L. and Antiochia, R. (2017) 'Beyond graphene: electrochemical sensors and biosensors for biomarkers detection.' *Biosensors and Bioelectronics*, 89 pp. 152-166.

Butt, M., Degtyarev, S., Khonina, S. and Kazanskiy, N. (2017) 'An evanescent field absorption gas sensor at mid-IR 3.39 μ m wavelength.' *Journal of Modern Optics*, 64(18) pp. 1892-1897.

Butt, M. A., Voronkov, G. S., Grakhova, E. P., Kutluyarov, R. V., Kazanskiy, N. L. and Khonina, S. N. (2022) 'Environmental monitoring: A comprehensive review on optical waveguide and fiber-based sensors.' *Biosensors*, 12(11) p. 1038.

Chapalo, I., Stylianou, A., Mégret, P. and Theodosiou, A. (2024) *Advances in optical fiber speckle sensing: A comprehensive review.* Vol. 11: MDPI.

Chen, H. and Gu, Z. (2012) 'Design optimization of an intensity-interrogated long-period fibre grating film sensor operating near the phase-matching turning point.' *Measurement Science and Technology*, 23(3) p. 035105.

Cole, M., Hiralal, P., Ying, K., Li, C., Zhang, Y., Teo, K., Ferrari, A. and Milne, W. (2012) 'Dry-Transfer of Aligned Multiwalled Carbon Nanotubes for Flexible Transparent Thin Films.' *Journal of Nanomaterials*, 2012(1) p. 272960.

De Waele, W., Degrieck, J., Taerwe, W. M. L. and Baets, R. (2025) 'Non-destructive monitoring of composite elements by means of embedded optical fibre Bragg-sensors.' *WIT Transactions on Engineering Sciences*, 28

Del Villar, I., Matias, I. R. and Arregui, F. J. (2006) 'Influence on cladding mode distribution of overlay deposition on long-period fiber gratings.' *JOSA A*, 23(3) pp. 651-658.

Demon, S. Z. N., Kamisan, A. I., Abdullah, N., Noor, S. A. M., Khim, O. K., Kasim, N. A. M., Yahya, M. Z. A., Manaf, N. A. A., et al. (2020) 'Graphene-based Materials in Gas Sensor Applications: A Review.' *Sensors & Materials*, 32

Deng, Y. and Jiang, J. (2022) 'Optical fiber sensors in extreme temperature and radiation environments: A review.' *IEEE Sensors Journal*, 22(14) pp. 13811-13834.

Dong, M. (2013) 'The essence of modern HPLC: advantages, limitations, fundamentals, and opportunities.'

Dresselhaus, M. S. and Avouris, P. (2001) 'Introduction to carbon materials research.' *In Carbon nanotubes: synthesis, structure, properties, and applications.* Springer, pp. 1-9.

Eguchi, K. (1992) 'Optical gas sensors.' In Gas Sensors. Springer, pp. 307-328.

Elsherif, M., Salih, A. E., Muñoz, M. G., Alam, F., AlQattan, B., Antonysamy, D. S., Zaki, M. F., Yetisen, A. K., et al. (2022) 'Optical fiber sensors: Working principle, applications, and limitations.' *Advanced Photonics Research*, 3(11) p. 2100371.

Essamlali, I., Nhaila, H. and El Khaili, M. (2024) 'Advances in machine learning and IoT for water quality monitoring: A comprehensive review.' *Heliyon*,

Fan, X., Deng, S., Wei, Z., Wang, F., Tan, C. and Meng, H. (2021) 'Ammonia gas sensor based on graphene oxide-coated mach-zehnder interferometer with hybrid fiber structure.' *Sensors*, 21(11) p. 3886.

Fang, M., Xiong, X., Hao, Y., Zhang, T., Wang, H., Cheng, H.-M. and Zeng, Y. (2019) 'Preparation of highly conductive graphene-coated glass fibers by sol-gel and dip-coating method.' *Journal of Materials Science & Technology*, 35(9) pp. 1989-1995.

Fenjan, D. A., Mahdi, B. R. and Yusr, H. A. (2023) 'Graphene Oxide-Coated Mach-Zehnder Interferometer Based Ammonia Gas Sensor.' *Nexo Revista Científica*, 36(06) pp. 1132-1140.

- Ferrier, D. C. and Honeychurch, K. C. (2021) 'Carbon nanotube (CNT)-based biosensors.' *Biosensors*, 11(12) p. 486.
- Fu, R., Chen, X., Yan, X., Li, H., Hu, T., Wei, L., Qu, Y. and Cheng, T. (2024) 'Optical fiber sensors for heavy metal ion sensing.' *Journal of materials science & technology*, 189 pp. 110-131.
- Gojny, F. H., Wichmann, M. H. G., Köpke, U., Fiedler, B. and Schulte, K. (2004) 'Carbon nanotube-reinforced epoxy-composites: enhanced stiffness and fracture toughness at low nanotube content.' *Composites science and technology*, 64(15) pp. 2363-2371.
- Golnabi, H. (2012) 'Carbon nanotube research developments in terms of published papers and patents, synthesis and production.' *Scientia Iranica*, 19(6)
- Gómez-Galdós, C., Fernández-Manteca, M. G., García-García, B., Perez-Asensio, A., Algorri, J. F., López-Higuera, J. M., Cobo, A. and Rodríguez-Cobo, L. (2025) *Silica microlenses for extrinsic optical fibre sensors.* Vol. 13639: SPIE.
- González-Morales, D., Valencia, A., Díaz-Nuñez, A., Fuentes-Estrada, M., López-Santos, O. and García-Beltrán, O. (2020) 'Development of a low-cost UV-Vis spectrophotometer and its application for the detection of mercuric ions assisted by chemosensors.' *Sensors*, 20(3) p. 906.
- Gope, E. R., Begum, S. M., Anisetti, P. P., Kasa, G. G., Eedarada, V. G., Nalli, J. and Thummidi, R. S. (2024) 'A Review of Principles, Applications, and Recent Developments in HPTLC and HPLC.' *Journal of Pharma Insights and Research*, 2(6) pp. 056-064.
- Götz, A., Nikzad-Langerodi, R., Staedler, Y., Bellaire, A. and Saukel, J. (2020) 'Apparent penetration depth in attenuated total reflection Fourier-transform infrared (ATR-FTIR) spectroscopy of Allium cepa L. epidermis and cuticle.' *Spectrochimica Acta Part A: Molecular and Biomolecular Spectroscopy*, 224 p. 117460.
- Goyer, R. A. (1993) 'Lead toxicity: current concerns.' *Environmental health perspectives*, 100 pp. 177-187.
- Guan, L., Zhou, Y. and Yang, S. (2024) 'An improved prediction model for COD measurements using UV-Vis spectroscopy.' *RSC advances*, 14(1) pp. 193-205.
- Guo, F., Zeng, P., Liu, J., Hu, H., Zhu, W., Wang, Y. and Cheng, H. (2024) 'Simultaneous preconcentration and quantification of ultra-trace tin and lead

species in seawater by online SPE coupled with HPLC-ICP-MS.' *Analytica Chimica Acta*, 1294 p. 342294.

Guo, Y., Liu, C., Ye, R. and Duan, Q. (2020) 'Advances on water quality detection by uv-vis spectroscopy.' *Applied Sciences*, 10(19) p. 6874.

Hamada, N., Sawada, S.-i. and Oshiyama, A. (1992) 'New one-dimensional conductors: Graphitic microtubules.' *Physical review letters*, 68(10) p. 1579.

Hao, T. and Chiang, K. S. (2017) 'Graphene-based ammonia-gas sensor using infiber Mach-Zehnder interferometer.' *IEEE Photonics Technology Letters*, 29(23) pp. 2035-2038.

Haque, F., Bubli, S. Y. and Khan, M. S. (2021) 'UV-Vis spectroscopy for food analysis.' *Techniques to Measure Food Safety and Quality: Microbial, Chemical, and Sensory*, pp. 169-193.

Haque, M., Marinelli, C., Udrea, F. and Milne, W. (2006) *Absorption characteristics of single wall carbon nanotubes.* Vol. 1: Citeseer.

Huang, X., Li, X., Yang, J., Tao, C., Guo, X., Bao, H., Yin, Y., Chen, H., et al. (2017) 'An in-line Mach-Zehnder interferometer using thin-core fiber for ammonia gas sensing with high sensitivity.' *Scientific reports*, 7(1) pp. 1-8.

Ibrahim, K. S. (2013) 'Carbon nanotubes-properties and applications: a review.' *Carbon letters*, 14(3) pp. 131-144.

lijima, S. and Ichihashi, T. (1993) 'Single-shell carbon nanotubes of 1-nm diameter.' *nature*, 363(6430) pp. 603-605.

Jang, E. Y., Kang, T. J., Im, H. W., Kim, D. W. and Kim, Y. H. (2008) 'Single-walled carbon-nanotube networks on large-area glass substrate by the dipcoating method.' *Small*, 4(12) pp. 2255-2261.

Jiang, B., Xue, M., Zhao, C., Mao, D., Zhou, K., Zhang, L. and Zhao, J. (2016) 'Refractometer probe based on a reflective carbon nanotube-modified microfiber Bragg grating.' *Applied Optics*, 55(25) pp. 7037-7041.

Johny, J., Amos, S. and Prabhu, R. (2021) 'Optical fibre-based sensors for oil and gas applications.' *Sensors*, 21(18) p. 6047.

- Justino, C. I., Gomes, A. R., Freitas, A. C., Duarte, A. C. and Rocha-Santos, T. A. (2017) 'Graphene based sensors and biosensors.' *TrAC Trends in Analytical Chemistry*, 91 pp. 53-66.
- Karimian, S., Ali, M. M., McAfee, M., Saleem, W., Duraibabu, D., Memon, S. F. and Lewis, E. (2025) 'Challenges in Adapting Fibre Optic Sensors for Biomedical Applications.' *Biosensors*, 15(5) p. 312.
- Kataura, H., Kumazawa, Y., Maniwa, Y., Umezu, I., Suzuki, S., Ohtsuka, Y. and Achiba, Y. (1999) 'Optical properties of single-wall carbon nanotubes.' *Synthetic metals*, 103(1-3) pp. 2555-2558.
- Kazakevich, Y. V. and Lobrutto, R. (2006) *HPLC for pharmaceutical scientists.* John Wiley & Sons.
- Khalid, K., Ishak, R. and Chowdhury, Z. Z. (2024) 'UV-Vis spectroscopy in non-destructive testing.' *In Non-destructive material characterization methods*. Elsevier, pp. 391-416.
- Khijwania, S. K., Srinivasan, K. L. and Singh, J. P. (2005) 'An evanescent-wave optical fiber relative humidity sensor with enhanced sensitivity.' *Sensors and Actuators B: Chemical*, 104(2) pp. 217-222.
- Khonina, S. N., Kazanskiy, N. L. and Butt, M. A. (2023) 'Optical fibre-based sensors—an assessment of current innovations.' *Biosensors*, 13(9) p. 835.
- Kim, S., Yim, J., Wang, X., Bradley, D. D., Lee, S. and DeMello, J. C. (2010) 'Spin-and spray-deposited single-walled carbon-nanotube electrodes for organic solar cells.' *Advanced Functional Materials*, 20(14) pp. 2310-2316.
- Kim, S., Han, J., Choi, J. M., Nam, J. S., Lee, I. H., Lee, Y., Novikov, I. V., Kauppinen, E. I., et al. (2024) 'Aerosol-Synthesized Surfactant-Free Single-Walled Carbon Nanotube-Based NO2 Sensors: Unprecedentedly High Sensitivity and Fast Recovery.' *Advanced Materials*, 36(24) p. 2313830.
- Kim, Y., Jeon, Y., Na, M., Hwang, S.-J. and Yoon, Y. (2024) 'Recent Trends in Chemical Sensors for Detecting Toxic Materials.' *Sensors*, 24(2) p. 431.
- Kirsanov, D., Rudnitskaya, A., Legin, A. and Babain, V. (2017) 'UV-Vis spectroscopy with chemometric data treatment: an option for on-line control in nuclear industry.' *Journal of Radioanalytical and Nuclear Chemistry*, 312 pp. 461-470.

- Kohli, K., Kedia, J., Gupta, N. and Vijaykumar, P. (2025) *Optical fibre sensors with LSPR sensing: A comprehensive review.* Vol. 3227: AIP Publishing.
- Kuila, T., Bose, S., Mishra, A. K., Khanra, P., Kim, N. H. and Lee, J. H. (2012) 'Chemical functionalization of graphene and its applications.' *Progress in Materials Science*, 57(7) pp. 1061-1105.
- Kumar, M. and Ando, Y. (2010) 'Chemical vapor deposition of carbon nanotubes: a review on growth mechanism and mass production.' *Journal of nanoscience and nanotechnology*, 10(6) pp. 3739-3758.
- Kumar, M., Khamis, K., Stevens, R., Hannah, D. M. and Bradley, C. (2024) 'Insitu optical water quality monitoring sensors—applications, challenges, and future opportunities.' *Frontiers in Water*, 6 p. 1380133.
- Kumar, P., Kumar, S., Kumar, J., Purbia, G., Prakash, O. and Dixit, S. (2019) 'Graphene-oxide-coated fiber Bragg grating sensor for ethanol detection in petrol.' *Measurement Science and Technology*, 31(2) p. 025109.
- Kunaraj, A., Chelvanathan, P., Bakar, A. A. A. and Yahya, I. (2023) 'Single-Walled Carbon Nanotube (SWCNT) thin films via automatic spray coating and nitric acid vapor treatment.' *Journal of Engineering Research*,
- Lee, B. (2003) 'Review of the present status of optical fiber sensors.' *Optical fiber technology*, 9(2) pp. 57-79.
- Lee, C., Wei, X., Kysar, J. W. and Hone, J. (2008) 'Measurement of the elastic properties and intrinsic strength of monolayer graphene.' *science*, 321(5887) pp. 385-388.
- Leveque, G. and Villachon-Renard, Y. (1990) 'Determination of optical constants of thin film from reflectance spectra.' *Applied optics*, 29(22) pp. 3207-3212.
- Li, C., Tong, X., Huang, W., Wang, Y., Zeng, F., Chen, L., Shi, X. and Zeng, C. (2024) 'Development of a fast response, high accuracy, and miniaturized fiber Bragg grating (FBG) sensor for fluid temperature measurement.' *IEEE Sensors Journal*, 24(6) pp. 8746-8753.
- Li, D. and Kaner, R. B. (2008) 'Graphene-based materials.' *Science*, 320(5880) pp. 1170-1171.

- Li, M., Yu, Y., Lu, Y., Hu, X., Wang, Y., Qin, S., Lu, J., Yang, J., et al. (2021) 'Optical microfiber all-optical phase modulator for fiber optic hydrophone.' *Nanomaterials*, 11(9) p. 2215.
- Liauw, M. A., Baylor, L. C. and O'Rourke, P. E. (2010) 'UV-Visible Spectroscopy for On-Line Analysis.' *Process analytical technology: Spectroscopic tools and implementation strategies for the chemical and pharmaceutical industries*, pp. 81-106.
- Ligler, F. S. and Taitt, C. R. (2011) *Optical biosensors: today and tomorrow.* Elsevier.
- Lindon, J. C., Nicholson, J. K. and Wilson, I. D. (2021) 'The development and application of coupled HPLC-NMR spectroscopy.' *Advances in chromatography*, pp. 315-382.
- Liu, C., Cai, Q., Sun, Z., Xu, B., Zhao, J., Zhang, L. and Chen, X. (2016) *Fibre optic chemical sensor based on graphene oxide-coated long period grating.* Vol. 9916: International Society for Optics and Photonics.
- Liu, C., Xu, B., Zhou, L., Sun, Z., Mao, H., Zhao, J., Zhang, L. and Chen, X. (2018) 'Graphene oxide functionalized long period fiber grating for highly sensitive hemoglobin detection.' *Sensors and Actuators B: Chemical*, 261 pp. 91-96.
- Liu, T., Song, Z., Reeves, R., Wang, M., Doyle, C. T., Booth, M. J. and Fells, J. A. (2024) '3D Structured Optical Fiber Pressure Sensors.' *Journal of Lightwave Technology*,
- Liu, X. (2006) *Synthesis, devices and applications of carbon nanotubes.* University of Southern California.
- Lu, H., Wang, M. R., Wang, J. and Shen, M. (2014) 'Tear film measurement by optical reflectometry technique.' *Journal of biomedical optics*, 19(2) p. 027001.
- Luo, K., Peng, H., Zhang, B., Chen, L., Zhang, P., Peng, Z. and Fu, X. (2024) 'Advances in carbon nanotube-based gas sensors: Exploring the path to the future.' *Coordination Chemistry Reviews*, 518 p. 216049.
- Lv, Z., Zhu, B., Lu, L., Yuan, P., Lou, X., Dong, M. and Zhu, L. (2025) 'Miniature and low-power high-precision FBG interrogator with self-temperature compensation.' *Optics Express*, 33(5) pp. 10289-10301.

Lyu, D., Huang, Q., Wu, X., Nie, Y. and Yang, M. (2024) 'Optical fiber sensors for water and air quality monitoring: a review.' *Optical Engineering*, 63(3) pp. 031004-031004.

Ma, S., Xu, Y., Pang, Y., Zhao, X., Li, Y., Qin, Z., Liu, Z., Lu, P., et al. (2022) 'Optical fiber sensors for high-temperature monitoring: a review.' *Sensors*, 22(15) p. 5722.

Madou, M. J. (2011) *Manufacturing techniques for microfabrication and nanotechnology.* CRC press.

Mäntele, W. and Deniz, E. (2017) UV–VIS absorption spectroscopy: Lambert-Beer reloaded. Vol. 173, pp. 965-968. Elsevier.

Marcuse, D. (2012) Principles of optical fiber measurements. Elsevier.

Memon, S. F., Wang, R., Strunz, B., Chowdhry, B. S., Pembroke, J. T. and Lewis, E. (2022) 'A review of optical fibre ethanol sensors: Current state and future prospects.' *Sensors*, 22(3) p. 950.

Meng, L., Liu, G. and Feng, Z. (2025) 'Highly sensitive evanescent wave SERS probe based on exposed-core optical fibers and its application.' *RSC advances*, 15(10) pp. 7987-7994.

Meyyappan, M. (2004) Carbon nanotubes: science and applications. CRC press.

Mirchin, N., Lapsker, I., Tannous, E. and Peled, A. (2013) 'Palladium Ultra Thin Layer Profiles Evaluation by Evanescent Light.'

Mohan, S. and Negi, M. S. (2024) 'Carbon nanotube-based Optical Fiber Sensor with Rapid Response for Human Breath Monitoring and Voiceprint Recognition.' *IEEE Sensors Letters*,

Moonen, N. N. and Diederich, F. (2004) 'Limitations on the use of UV/Vis spectroscopy for the evaluation of conjugation effectiveness.' *Organic & biomolecular chemistry*, 2(16) pp. 2263-2266.

Morawska, K. and Wardak, C. (2024) 'Application of ionic liquids in ion-selective electrodes and reference electrodes: A review.' *ChemPhysChem*, 25(7) p. e202300818.

- Ni, Y.-Q., Ding, S., Han, B. and Wang, H. (2019) 'Layer-by-layer assembly of polyelectrolytes-wrapped multi-walled carbon nanotubes on long period fiber grating sensors.' *Sensors and Actuators B: Chemical*, 301 p. 127120.
- Nor, M. S. M., Khan, A. A., Mohamad, S. and Thirunavakkarasu, P. (2023) 'Development of Optical Fiber Sensor for Water Salinity Detection.' *Development*, 14(6)
- Ochoa, M., Algorri, J. F., Roldán-Varona, P., Rodríguez-Cobo, L. and López-Higuera, J. M. (2021) 'Recent advances in biomedical photonic sensors: A focus on optical-fibre-based sensing.' *Sensors*, 21(19) p. 6469.
- Pal, S., Shukla, S., Sharma, S., Khandelwal, V., Rizwan, A. and Yadav, S. (2024) 'RECENT TRENDS IN HPLC TECHNIQUES FOR DRUG DEVELOPMENT REVIEW.'
- Pant, M., Singh, R., Negi, P., Tiwari, K. and Singh, Y. (2021) 'A comprehensive review on carbon nano-tube synthesis using chemical vapor deposition.' *Materials Today: Proceedings*, 46 pp. 11250-11253.
- Papp, L. A., Szabó, Z. I., Hancu, G., Farczádi, L. and Mircia, E. (2024) 'Comprehensive review on chiral stationary phases in single-column simultaneous chiral—achiral HPLC separation methods.' *Molecules*, 29(6) p. 1346.
- Paramasivam, G., Palem, V. V., Meenakshy, S., Suresh, L. K., Gangopadhyay, M., Antherjanam, S. and Sundramoorthy, A. K. (2024) 'Advances on carbon nanomaterials and their applications in medical diagnosis and drug delivery.' *Colloids and Surfaces B: Biointerfaces*, p. 114032.
- Patil, K. P., Patil, D. M., Patil, S. A. and Pawar, S. P. (2023) 'A Review on Development and validation of HPLC method.' *International Journal of Research in Pharmacy and Allied Science*, 2(2) pp. 90-98.
- Pena-Pereira, F., Costas-Mora, I., Romero, V., Lavilla, I. and Bendicho, C. (2011) 'Advances in miniaturized UV-Vis spectrometric systems.' *TrAC Trends in Analytical Chemistry*, 30(10) pp. 1637-1648.
- Pietrzak, K. and Wardak, C. (2021) 'Comparative study of nitrate all solid state ion-selective electrode based on multiwalled carbon nanotubes-ionic liquid nanocomposite.' *Sensors and Actuators B: Chemical*, 348 p. 130720.
- Punjabi, N., Satija, J. and Mukherji, S. (2015) 'Evanescent wave absorption based fiber-optic sensor-cascading of bend and tapered geometry for enhanced sensitivity.' *In Sensing Technology: Current Status and Future Trends III.* Springer, pp. 25-45.

Qi, X., Lian, Y., Xie, L., Wang, Y. and Lu, Z. (2024) 'Water quality detection based on UV-Vis and NIR spectroscopy: a review.' *Applied Spectroscopy Reviews*, 59(8) pp. 1036-1060.

Rao, R. K., Gautham, S. and Sasmal, S. (2024) 'A comprehensive review on carbon nanotubes based smart nanocomposites sensors for various novel sensing applications.' *Polymer Reviews*, 64(2) pp. 575-638.

Reynoso-Noverón, N., Santibáñez-Andrade, M., Torres, J., Bautista-Ocampo, Y., Sánchez-Pérez, Y. and García-Cuellar, C. M. (2024) 'Benzene exposure and pediatric leukemia: From molecular clues to epidemiological insights.' *Toxicology Letters*,

Ríos-Reina, R. and Azcarate, S. M. (2022) 'How chemometrics revives the UV-Vis spectroscopy applications as an analytical sensor for spectralprint (nontargeted) analysis.' *Chemosensors*, 11(1) p. 8.

Rivero, P. J., Goicoechea, J. and Arregui, F. J. (2019) 'Layer-by-layer nano-assembly: A powerful tool for optical fiber sensing applications.' *Sensors*, 19(3) p. 683.

Safira, P. (2025) 'Analysis of fiber optic evanescent wave sensor for the rapid detection of organic pollutants in drinking water sources: A review.' *Journal of Opto-Electro-Medic Science*, 1(1) pp. 9-14.

Selvarajan, A., Kar, S. and Srinivas, T. (2003) *Optical fiber communication:* principles and systems. Tata McGraw-Hill Education.

Shadab, A. and Raghuwanshi, S. K. (2022) 'Development and sensitivity analysis of rGO-TiO₂ coated eFBG sensor for the detection of ethanol in petrochemicals.' *IEEE Sensors Journal*, 22(13) pp. 12913-12920.

Shi, Z., Chow, C. W., Fabris, R., Liu, J. and Jin, B. (2022) 'Applications of online UV-Vis spectrophotometer for drinking water quality monitoring and process control: a review.' *Sensors*, 22(8) p. 2987.

Shivananju, B., Yamdagni, S., Fazuldeen, R., Sarin Kumar, A., Hegde, G., Varma, M. and Asokan, S. (2013) 'CO2 sensing at room temperature using carbon nanotubes coated core fiber Bragg grating.' *Review of scientific instruments*, 84(6)

Shivananju, B. N., Yamdagni, S., Fazuldeen, R., Kumar, A. K. S., Nithin, S. P., Varma, M. M. and Asokan, S. (2014) 'Highly sensitive carbon nanotubes coated

etched fiber Bragg grating sensor for humidity sensing.' *IEEE Sensors Journal*, 14(8) pp. 2615-2619.

Shoukat, R. and Khan, M. I. (2021) 'Carbon nanotubes: a review on properties, synthesis methods and applications in micro and nanotechnology.' *Microsystem Technologies*, pp. 1-10.

Singh, R., Gupta, R., Bansal, D., Bhateria, R. and Sharma, M. (2024) 'A review on recent trends and future developments in electrochemical sensing.' *ACS omega*, 9(7) pp. 7336-7356.

Snyder, L. R., Kirkland, J. J. and Dolan, J. W. (2011) *Introduction to modern liquid chromatography.* John Wiley & Sons.

Spotnitz, M. E., Ryan, D. and Stone, H. A. (2004) 'Dip coating for the alignment of carbon nanotubes on curved surfaces.' *Journal of Materials Chemistry*, 14(8) pp. 1299-1302.

Sridevi, S., Vasu, K., Bhat, N., Asokan, S. and Sood, A. (2016) 'Ultra sensitive NO2 gas detection using the reduced graphene oxide coated etched fiber Bragg gratings.' *Sensors and Actuators B: Chemical*, 223 pp. 481-486.

Stradiotto, N. R., Yamanaka, H. and Zanoni, M. V. B. (2003) 'Electrochemical sensors: a powerful tool in analytical chemistry.' *Journal of the Brazilian Chemical Society*, 14(2) pp. 159-173.

Sudharshan, N. and Swetha, V. (2023) 'UV-VISIBLE SPECTROSCOPY: A COMPREHENSIVE REVIEW ON INSTRUMENTATION.' *World J. Pharm. Res*, 12(19) pp. 1342-1363.

Suk, J. W., Kitt, A., Magnuson, C. W., Hao, Y., Ahmed, S., An, J., Swan, A. K., Goldberg, B. B., et al. (2011) 'Transfer of CVD-grown monolayer graphene onto arbitrary substrates.' *ACS nano*, 5(9) pp. 6916-6924.

Sun, D., Mao, J., Liu, M., Liu, H., Zhang, S., Li, B., Jiang, X. and Ma, J. (2025) 'A fiber Bragg grating (FBG)-strain sensing tube for deep displacement measurement.' *Optics & Laser Technology*, 188 p. 112938.

Sun, S., Ma, F., He, Y., Niu, B., Wang, C., Dai, L. and Zhao, Z. (2025) 'An Optimized PZT-FBG Voltage/Temperature Sensor.' *Micromachines*, 16(2) p. 235.

- Sundari, C. S. and Edayadulla, N. (2024) 'Advancement of optical fibre in the medical field.' *In Glass-based Materials: Advances in energy, environment and health.* IOP Publishing Bristol, UK, pp. 3-1-3-19.
- Szulczyński, B. and Gębicki, J. (2017) 'Currently commercially available chemical sensors employed for detection of volatile organic compounds in outdoor and indoor air.' *Environments*, 4(1) p. 21.
- Tan, Y., Tou, Z., Chow, K. and Chan, C. (2015) 'Graphene-deposited photonic crystal fibers for continuous refractive index sensing applications.' *Optics express*, 23(24) pp. 31286-31294.
- Tan, Y., Ji, W., Mamidala, V., Chow, K. and Tjin, S. (2014a) 'Carbon-nanotube-deposited long period fiber grating for continuous refractive index sensor applications.' *Sensors and Actuators B: Chemical*, 196 pp. 260-264.
- Tan, Y., Tou, Z., Mamidala, V., Chow, K. and Chan, C. (2014b) 'Continuous refractive index sensing based on carbon-nanotube-deposited photonic crystal fibers.' *Sensors and Actuators B: Chemical*, 202 pp. 1097-1102.
- Tang, D.-M., Cretu, O., Ishihara, S., Zheng, Y., Otsuka, K., Xiang, R., Maruyama, S., Cheng, H.-M., et al. (2024) 'Chirality engineering for carbon nanotube electronics.' *Nature Reviews Electrical Engineering*, 1(3) pp. 149-162.
- Teng, C., Min, R., Zheng, J., Deng, S., Li, M., Hou, L. and Yuan, L. (2021) 'Intensity-modulated polymer optical fiber-based refractive index sensor: a review.' *Sensors*, 22(1) p. 81.
- Thakur, A. and Devi, P. (2024) 'A comprehensive review on water quality monitoring devices: materials advances, current status, and future perspective.' *Critical reviews in analytical chemistry*, 54(2) pp. 193-218.
- Thomas, S. N., French, D., Jannetto, P. J., Rappold, B. A. and Clarke, W. A. (2022) 'Liquid chromatography—tandem mass spectrometry for clinical diagnostics.' *Nature Reviews Methods Primers*, 2(1) p. 96.
- Toala, S. N., Sun, Z., Yue, Y., Gonski, S. F. and Cai, W.-J. (2024) 'Recent developments in ionophore-based potentiometric electrochemical sensors for oceanic carbonate detection.' *Sensors & Diagnostics*, 3(4) pp. 599-622.
- Van Den Broeke, J., Langergraber, G. and Weingartner, A. (2006) 'On-line and in-situ UV/vis spectroscopy for multi-parameter measurements: a brief review.' *Spectroscopy europe*, 18(4) pp. 15-18.

- Villatoro, J., Luna-Moreno, D. and Monzón-Hernández, D. (2005) 'Optical fiber hydrogen sensor for concentrations below the lower explosive limit.' *Sensors and Actuators B: Chemical*, 110(1) pp. 23-27.
- Wang, H., Wu, J. and Li, H. (2025) 'Strain measurement of CFRP-Steel bonded joints using distributed optical fibre sensors.' *The Journal of Adhesion*, 101(7) pp. 891-908.
- Wang, J., Wang, J. and Rogers, K. (1995) *Electrochemical sensors for environmental monitoring: a review of recent technology.* US Environmental Protection Agency, Office of Research and Development
- Wang, L., Wang, P., Gao, C., Zhao, X., Dong, Q., Chu, D., Bai, W., Li, Q., et al. (2025) 'A comprehensive review of FCCVD for carbon nanotubes growth.' *Journal of Materials Science*, pp. 1-26.
- Wang, Q., Kong, L., Dang, Y., Xia, F., Zhang, Y., Zhao, Y., Hu, H. and Li, J. (2016) 'High sensitivity refractive index sensor based on splicing points tapered SMF-PCF-SMF structure Mach-Zehnder mode interferometer.' *Sensors and Actuators B: Chemical*, 225 pp. 213-220.
- Wang, W.-S., Kuo, W.-T., Huang, H.-Y. and Luo, C.-H. (2010) 'Wide dynamic range CMOS potentiostat for amperometric chemical sensor.' *Sensors*, 10(3) pp. 1782-1797.
- Wang, X., Xiao, Y., Rans, C., Benedictus, R. and Groves, R. M. (2024) 'Enhanced Strain Measurement Sensitivity with Gold Nanoparticle-Doped Distributed Optical Fibre Sensing.' *Structural Control and Health Monitoring*, 2024(1) p. 2716156.
- Wei, T.-s. (1988) 'Polymer Materials for Optical Fiber Coatings.' *In Adhesives, Sealants, and Coatings for Space and Harsh Environments*. Springer, pp. 455-466.
- Whittaker, N. S., Nguyen, T. H., Fabian, M., Sun, T., Grattan, K. T., Khan, K., Parker, A. and Holt, A. (2025) 'Detection of codeine using a molecularly imprinted polymer-coated optical fibre sensor.' *Optics Communications*, 578 p. 131427.
- Willsch, M. and Bosselmann, T. (2002) Optical current sensor application in the harsh environment of a 120 MVA power generator. IEEE.
- Wójcik, G. and Przystalka, P. (2022) 'Experimental investigation of factors influencing the transmission capabilities of a low cost, side-polished evanescent

- wave absorption plastic optical fiber sensors.' *Procedia Structural Integrity*, 37 pp. 179-186.
- Wu, Z., Zhao, Y., You, T., Kou, Z., Xu, Y., Xia, M., Guo, H., Zhang, X., et al. (2025) 'In Situ Infared Optical Fiber Sensor Monitoring Reactants and Products Changes during Photocatalytic Reaction.' *Analytical Chemistry*,
- Wulandari, R., Iswara, A. P., Qadafi, M., Prayogo, W., Astuti, R. D. P., Utami, R. R., Jayanti, M., Awfa, D., et al. (2024) 'Water pollution and sanitation in Indonesia: a review on water quality, health and environmental impacts, management, and future challenges.' *Environmental Science and Pollution Research*, pp. 1-26.
- Xia, F. and Zhao, Y. (2020) 'RI sensing system with high sensitivity and large measurement range using a microfiber MZI and a photonic crystal fiber MZI.' *Measurement*, 156 p. 107603.
- Yao, B., Wu, Y., Cheng, Y., Zhang, A., Gong, Y., Rao, Y.-J., Wang, Z. and Chen, Y. (2014) 'All-optical Mach–Zehnder interferometric NH3 gas sensor based on graphene/microfiber hybrid waveguide.' *Sensors and Actuators B: Chemical*, 194 pp. 142-148.
- Yeung, K. K., Huang, T., Hua, Y., Zhang, K., Yuen, M. M. and Gao, Z. (2021) 'Recent advances in electrochemical sensors for wearable sweat monitoring: A review.' *IEEE Sensors Journal*, 21(13) pp. 14522-14539.
- You, T., Zhao, Y., Xu, Y., Guo, H., Zhu, J., Tao, H., Zhang, X. and Xu, Y. (2024) 'An infrared evanescent wave sensor for detection of ascorbic acid in food and drugs.' *Journal of Lightwave Technology*, 42(9) pp. 3494-3500.
- Yu, Q., Zhang, Y. n., Jiang, L., Li, L., Li, X. and Zhao, J. (2025) 'Flexible Optical Fiber Sensor for Non-Invasive Continuous Monitoring of Human Physiological Signals.' *Small Methods*, p. 2401368.
- Zainurin, S. N., Wan Ismail, W. Z., Mahamud, S. N. I., Ismail, I., Jamaludin, J., Ariffin, K. N. Z. and Wan Ahmad Kamil, W. M. (2022) 'Advancements in monitoring water quality based on various sensing methods: a systematic review.' *International Journal of Environmental Research and Public Health*, 19(21) p. 14080.
- Zhang, S.-q., Zhao, Y., Peng, Y. and Zhao, J.-C. (2024) 'High-sensitivity optical fiber SPR sensor with cascaded biconical fiber and hetero-core structure for simultaneous measurement of seawater salinity and temperature.' *Optics & Laser Technology*, 170 p. 110275.

- Zhang, Z., Zhang, H., Hou, L., Jia, D., Yao, K., Meng, Q., Qu, J., Yan, B., et al. (2024) 'Highly sensitive fiber-optic chemical pH sensor based on surface modification of optical fiber with ZnCdSe/ZnS quantum dots.' *Analytica Chimica Acta*, 1294 p. 342281.
- Zhao, B., Itkis, M., Niyogi, S., Hu, H., Zhang, J. and Haddon, R. (2004) 'Study of the extinction coefficients of single-walled carbon nanotubes and related carbon materials.' *The Journal of Physical Chemistry B*, 108(24) pp. 8136-8141.
- Zhou, J., Wang, Y., Liao, C., Sun, B., He, J., Yin, G., Liu, S., Li, Z., et al. (2015) 'Intensity modulated refractive index sensor based on optical fiber Michelson interferometer.' *Sensors and Actuators B: Chemical*, 208 pp. 315-319.
- Zhu, C., Zheng, H., Ma, L., Yao, Z., Liu, B., Huang, J. and Rao, Y. (2023) 'Advances in fiber-optic extrinsic Fabry—Perot interferometric physical and mechanical sensors: A review.' *IEEE Sensors Journal*, 23(7) pp. 6406-6426.
- Zubair, H., Bradley, D., Khairina, M., Oresegun, A., Basaif, A., Othman, J., Rifiat, R., Hamidi, F., et al. (2023) 'An extendable optical fibre probe survey meter for naturally occurring radioactive material (NORM) and other weak emitters.' *Scientific reports*, 13(1) p. 11918.

APPENDIX



Keywords:

Research article
Optical environmental sensing in wireless smart meter network
Minglong Zhang ¹ , Iek Cheong Lam ² , Arun Kumar ³ , Kin Kee Chow ² ,* and Peter Han Joo Chong ¹
1
2
3
* Correspondence:
Abstract:

1. Introduction

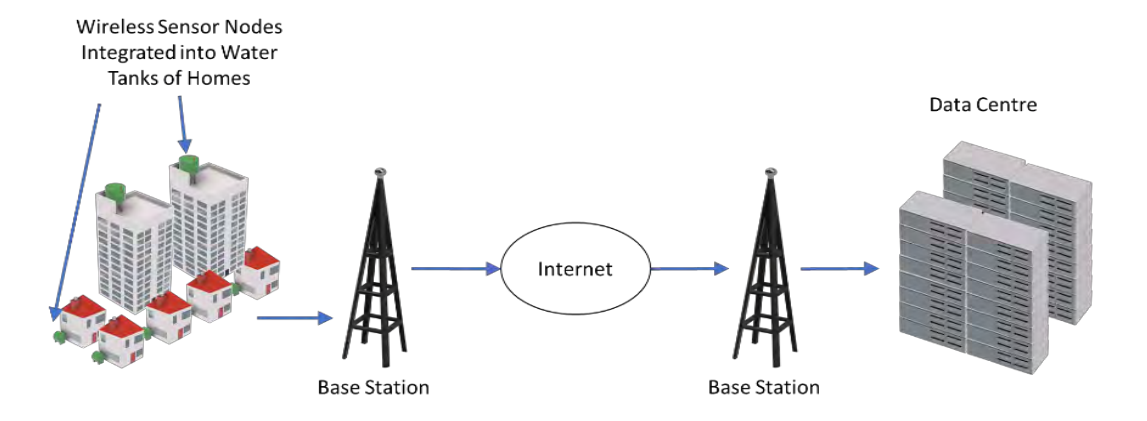


Figure 1.

2.	Comparison of sensors
2	
3.	Fabrication of sensing probe

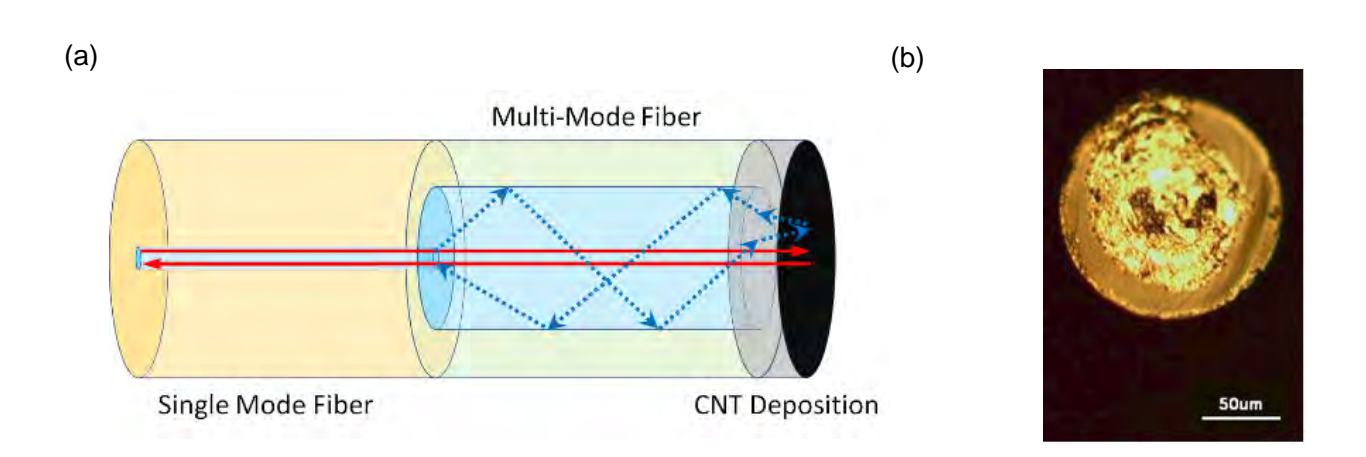


Figure 2

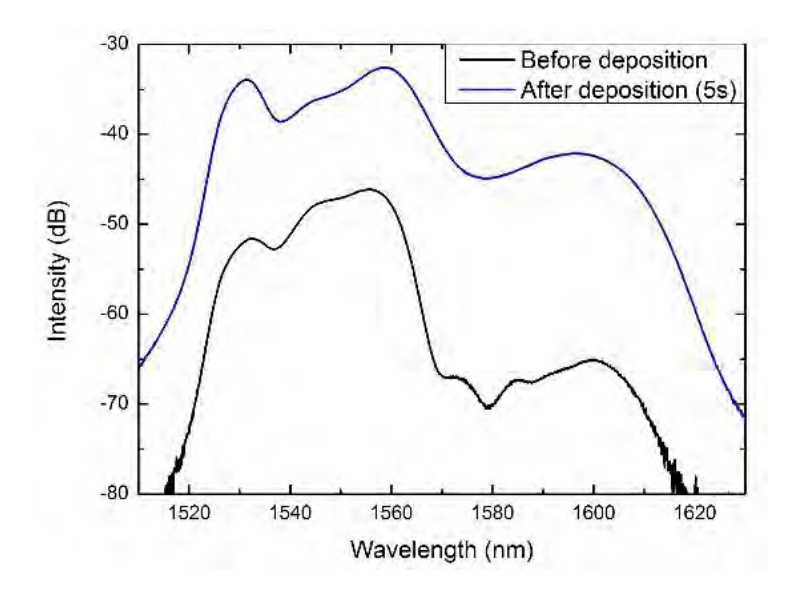


Figure 3.

4. Measurement results of sensing probe

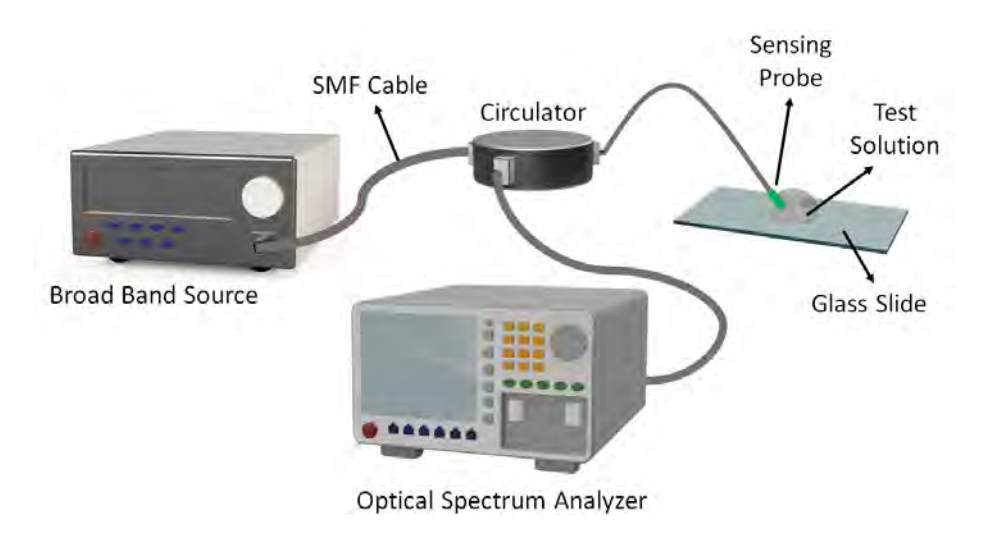


Figure 4.

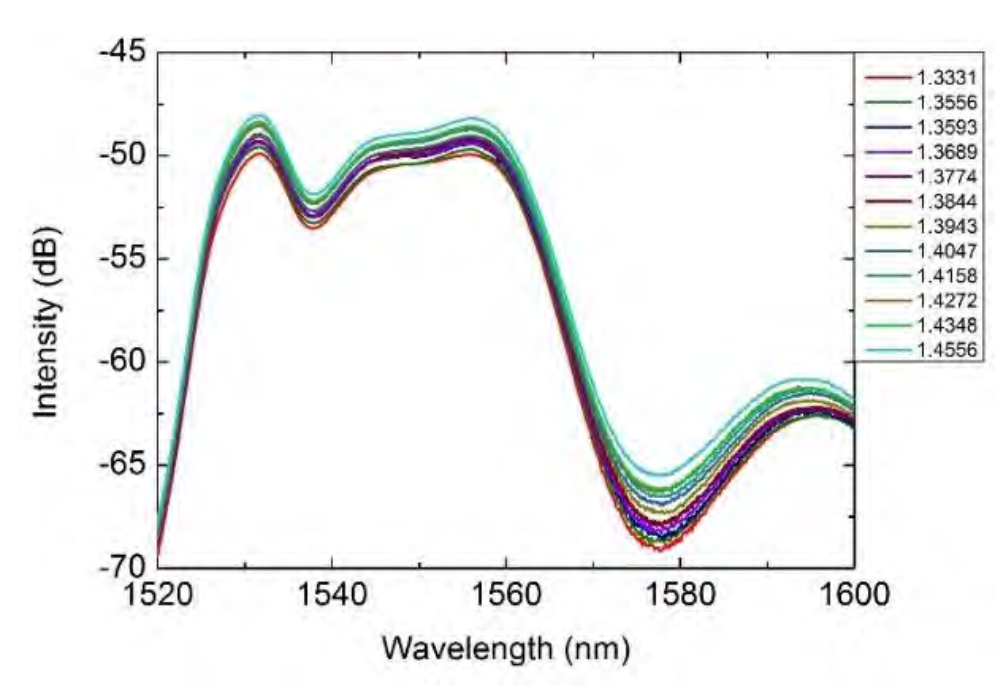


Figure 5.

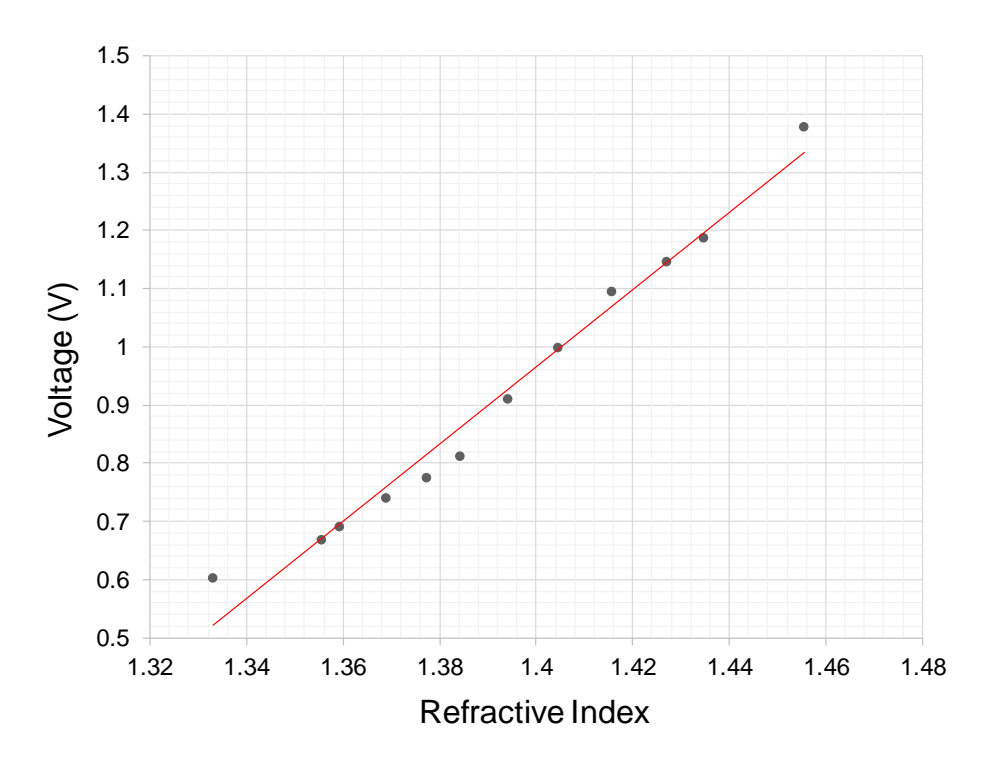


Figure 6.

5. Wireless sensor network and performance analysis

5.1. System model

$$PDR = \frac{t_p P}{TN_s}$$

Table 1

5.2. Simulation setup

5.3. Simulation results

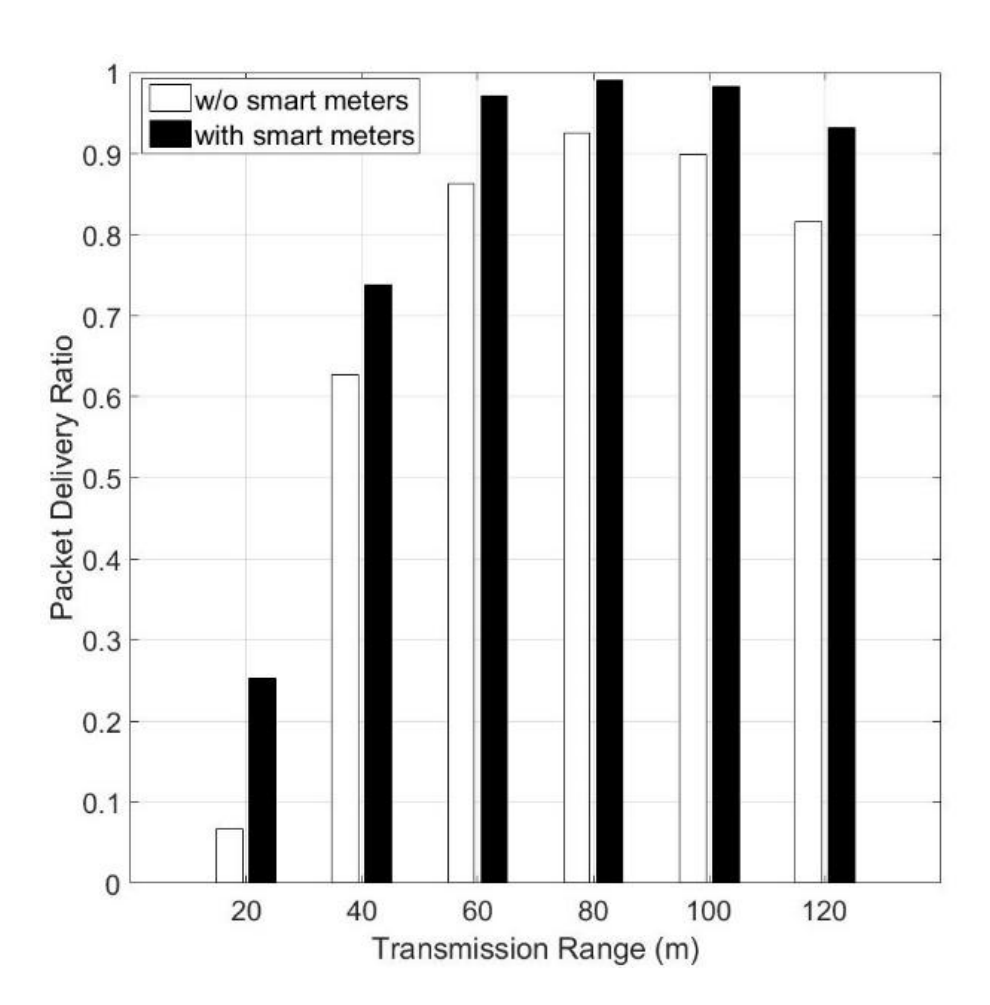


Figure 7.

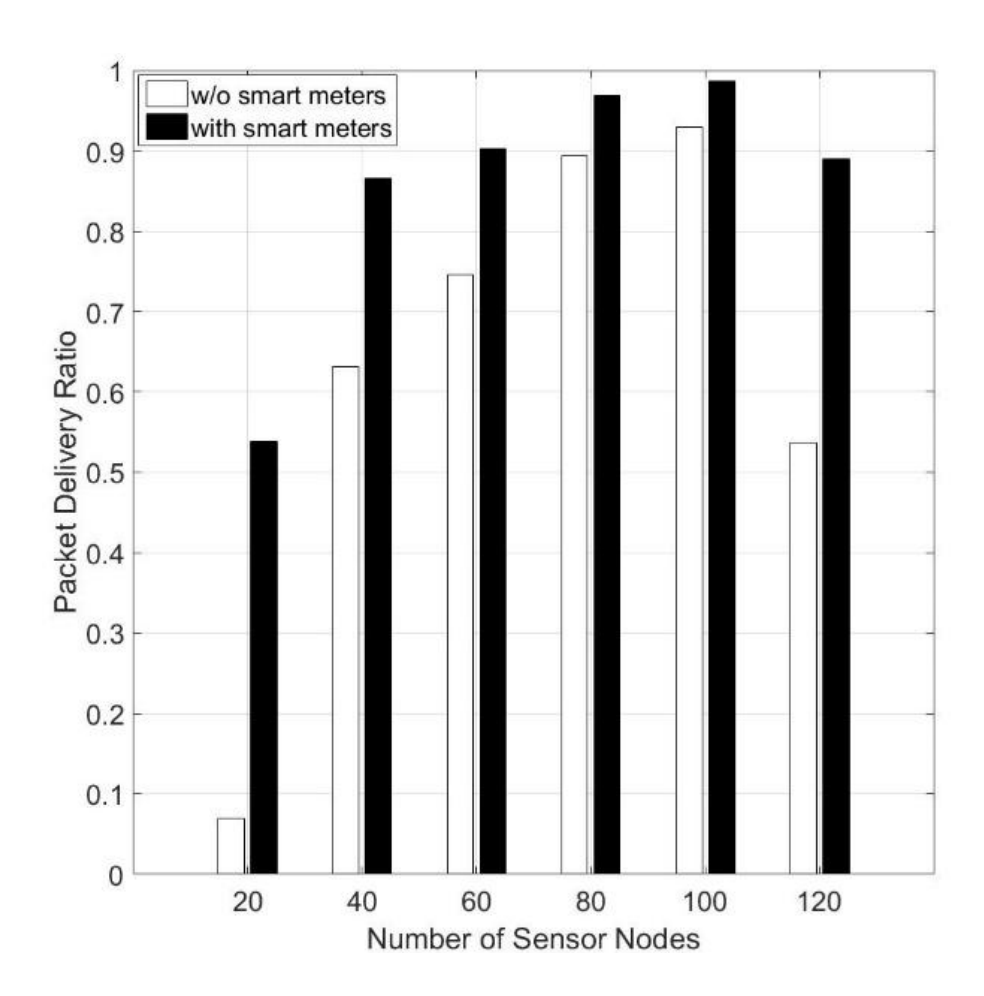


Figure 8.

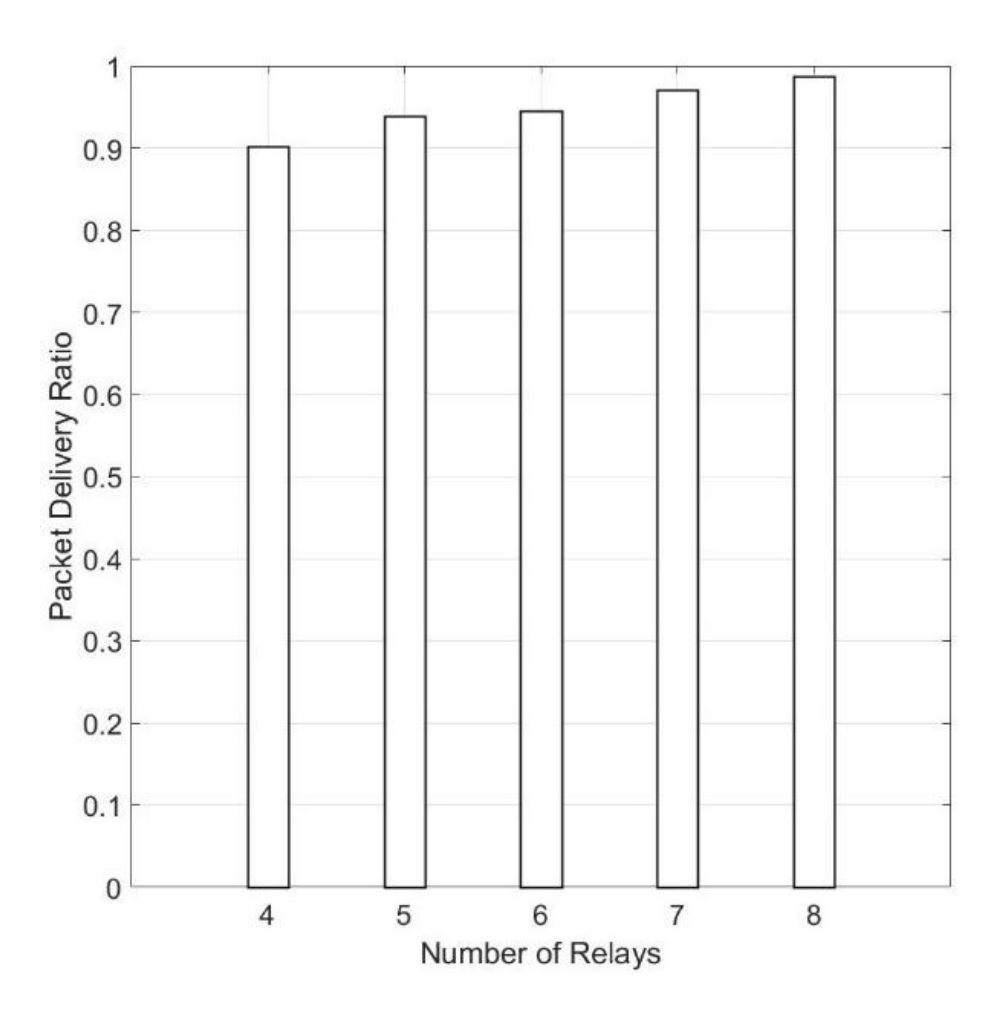


Figure 9.

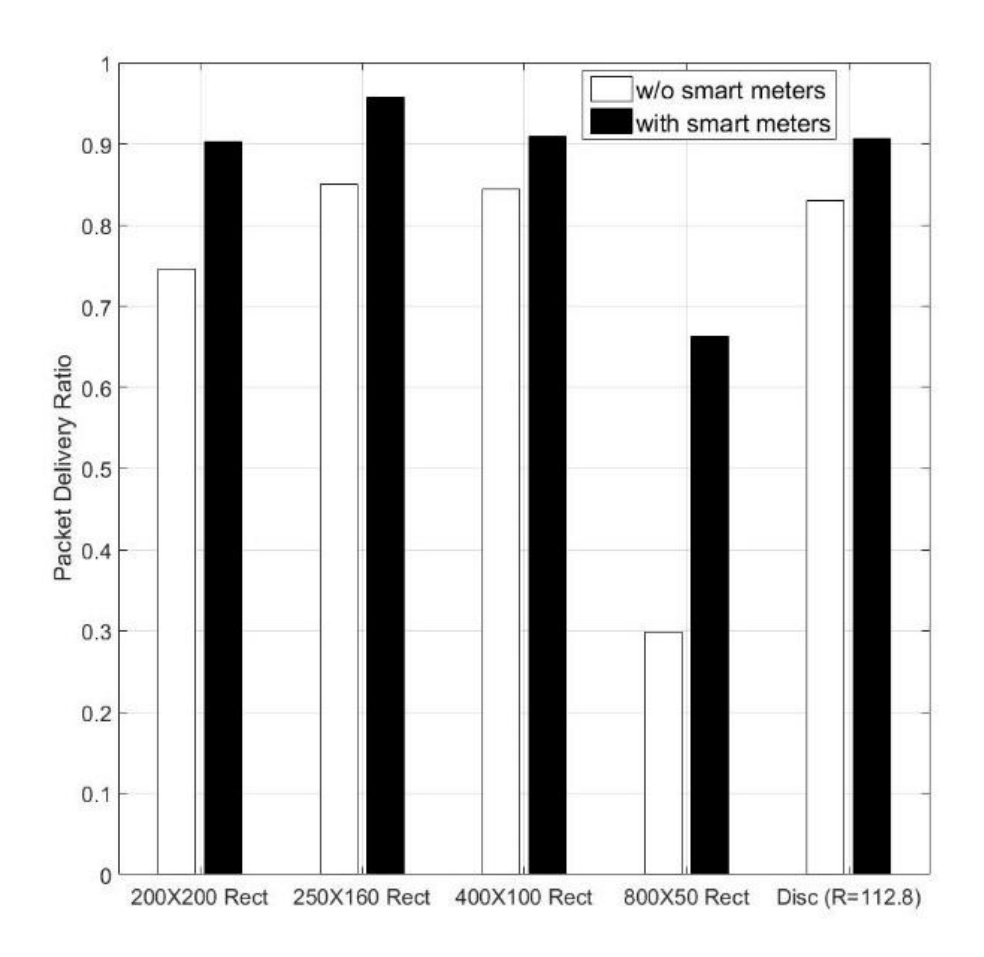


Figure 10.

6. Conclusion

Conflict of interest

References

Renew Sust Energ Rev

Comput Netw

J Infrastruct Syst

Sensors

Sensor Actuat A-Phys

J

Lightwave Technol

IEEE Sens J

Rev Sci Instrum

Sensor Actuat A-Phys

Sensor Actuat

A-Phys

Sensor Actuat B-Chem

Sensor Actuat B-Chem

Opt Express

Opt Express

Opt Express

J Lightwave Technol

IEEE T Microw Theory

AIMS Electronics and Electrical Engineering

Adv Drug Deliver Rev



Carbon Nanotubes Deposited Optical Fibers for Continuous Refractive Index Sensing Applications

Kin Kee Chow
School of Engineering
Manchester Metropolitan University
Manchester, United Kingdom
k chow@mmu ac uk

Iek Cheong Lam
School of Engineering
Manchester Metropolitan University
Manchester, United Kingdom
iek.c.lam@stu.mmu.ac.uk

Abstract—An optical fiber-based refractive index (RI) sensing probe fabricated through optical deposition of carbon nanotubes (CNTs) onto the cleaved end face of a multimode fiber (MMF) segment, fusion spliced at one end to a single mode fiber (SMF), is presented. The interference of the excited higher order modes in the MMF segment with the fundamental mode led to the formation of various spectral features in the resulting output spectrum which were then used as reference points for RI measurements. RI perturbations in the external environment of the sensing probe could then be characterized by variations in intensity of these spectral features with little wavelength dependence. The deposited CNTs extended the continuous measurement range of the sensor and the achievable sensitivity was calculated to be approximately 35.8 dB/RIU for the RI range of 1.33-1.40 and approximately 98.8 dB/RIU for the RI range of 1.40-1.46. The sensing probe also exhibited good stability with little fluctuations in intensity of the output spectrum for a constant RI.

Keywords—carbon nanotubes, optical fiber sensing, optical fiber devices, optical materials

I. INTRODUCTION

Refractive index (RI) sensing of a liquid medium has many important industrial applications especially in those involving water purification. These industries require low cost, easy to fabricate, and sensitive sensors which would enable them to detect RI changes within a suitable range of RIs. In recent years, optical fibers have been the subject of much research not only for their applications in the telecommunications industry but also for their applications in RI sensing. Optical fibers have been shown to be ideal RI sensors due to their compactibility, fast response, immunity to electromagnetic interference and ability to carry large amounts of information over long distances. Many types of fiber sensors for RI sensing have been proposed over the years. These fiber sensors usually consist of sensing probes fabricated through the inscription of a grating in various types of fibers [1-3], splicing fibers of different core dimensions together [4-9], depositing a plasmon supporting material onto the exposed fiber core [10-13] and tapering the fiber [14-18]. The sensing set up would usually require a light source and a spectrometer to monitor the transmitted or reflected spectrum. The change in RI of the external environment would usually be characterized by a shift in the wavelength or variation in intensity levels of any spectral features in the output spectrum. In recent years, many groups have managed to enhance these sensing probes further by depositing a thin layer of dielectric or polymer material onto the region of the sensing probe [19-26]. The deposited material would have a variety of functions including enhancing the sensitivity of the sensor, modifying the sensing scheme for wider sensing capabilities or improving the specificity of the sensor towards certain chemical compounds.

In this paper, a RI sensing probe working in the reflection configuration is proposed. The sensing probe was fabricated by first fusion splicing a multimode fiber (MMF) segment to a single mode fiber (SMF). The other end of the MMF segment is then cleaved to a certain length to form a joint fiber segment. Carbon nanotubes (CNTs) were then deposited onto the cleaved end face of the MMF segment using an optical deposition procedure whose process and mechanics have been extensively discussed in [28] and [29]. The behavior of the sensing probe to RI perturbations in the external environment was then characterized by a variation in intensity of the spectral features in the output spectrum with little fluctuations in their wavelengths. The deposited CNTs which are known to be a material with unique optical properties, such as a high RI [30], enabled the sensing probe to continuously measure a wide range of RIs and the achievable sensitivity was calculated to be approximately 35.8 dB/RIU for the RI range of 1.33-1.40 and approximately 98.8 dB/RIU for the RI range of 1.40-1.46. The sensing probe also displayed little variation in intensity when it was immersed in a solution of fixed RI over a period of time and can be concluded to exhibit good stability.

II. DESIGN AND FABRICATION OF SENSING PROBE

A schematic of the joint fiber segment is shown in Fig. 1. At the SMF-MMF interface, the fundamental mode (solid line) propagating through the SMF would excite the higher order modes (dashed line) in the MMF. These higher order modes would propagate through the MMF together with the fundamental mode. However, due to differences in their propagation constants, the higher order modes would accumulate a phase difference. At the MMF-external environment interface, part of the energy of all the modes would be reflected and the amount of reflectance would be governed by the Fresnel equation:

$$R = \left(\frac{n_{core} - n_{env}}{n_{core} - n_{env}}\right)^2 \tag{1}$$

where n_{core} and n_{env} are the RIs of the core of the MMF and the external environment, respectively. The reflected modes would then propagate back along the length of the MMF and interfere and recombine with each other at the MMF-SMF interface. Due to this interference and recombination, well defined interference peaks and dips (spectral features) can be observed in the reflected spectrum. These spectral features can then be used as accurate reference points to observe any variations in intensity of the back reflected light due to RI perturbations in the external environment around the MMF end face. Following the deposition of CNTs onto the cleaved

MMF end face of the joint fiber segment to form the sensing probe, all the modes arriving at the MMF-CNT interface would interact with the CNTs and experience a reflectance [31, 32]. Hence, the continuous detectable range of RIs for the sensing probe would be significantly wider.

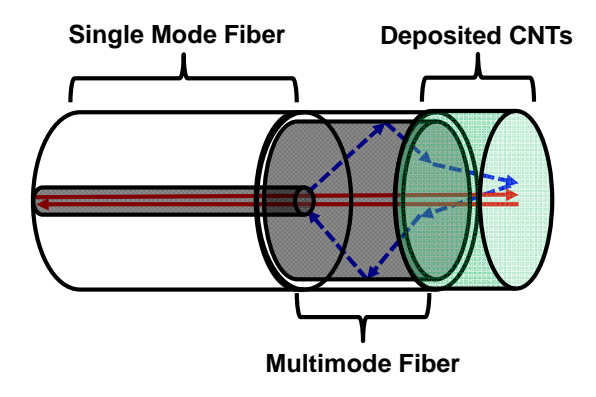


Fig. 1 Schematic illustration of sensor probe with carbon nanotubes (CNTs) deposited onto the cleaved MMF end face of a joint fiber segment.

In our experiment, a MMF fiber (Thor Labs AFS105/125Y) with core and cladding diameters of 105 μm and 125 μm , respectively, was first fusion spliced to a standard SMF. The MMF was then cleaved to a length of 21 mm from the SMF-MMF splice point to form the SMF-MMF joint fiber segment as shown in Fig. 1.

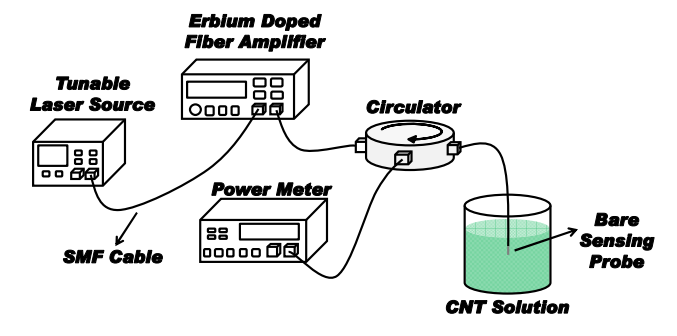


Fig. 2 Experimental setup for the optical deposition of CNTs onto the cleaved MMF end face of the joint fiber segment.

To deposit CNTs onto the cleaved MMF end face of the joint fiber segment, a CNT solution was prepared by first dispersing CNT powder into a fixed volume of dimethylformamide (DMF) solution and then sonicating the resulting solution in an ultrasonic water bath for approximately 30 hours. Optical deposition of CNTs onto the end face of the MMF was carried out using the setup shown in Fig. 2. The SMF end of the joint fiber segment was connected to a fiber circulator while the MMF end of the joint fiber segment was lowered vertically into the CNT solution. Light from a tunable laser source, amplified to an intensity of 19 dBm (at 1550 nm) by an erbium doped fiber amplifier, was coupled into the joint fiber segment via a circulator. The back reflected light from the joint fiber segment would propagate through the circulator and be coupled into a power meter where its intensity would be monitored throughout the deposition process. Changes in the intensity would indicate that CNTs have been deposited onto the MMF end face of the joint fiber segment to form the sensing probe as shown in Fig. 1. The joint fiber segment was removed from the CNT solution 5 s after the change in intensity was observed and left to dry without any further

physical or chemical treatment. The output spectrum of the joint fiber segment before (dashed line) and after (solid line) the optical deposition process is shown in Fig. 3. As can be seen, the deposition of CNTs resulted approximately in a 6 dB increase in intensity and approximately 0.6 nm red shift in the wavelength. The increase in intensity of the reflected spectrum is to be expected as the CNTs would vary the amount of reflectance. The red shift is relatively small and can be attributed to measurement errors from the equipment.

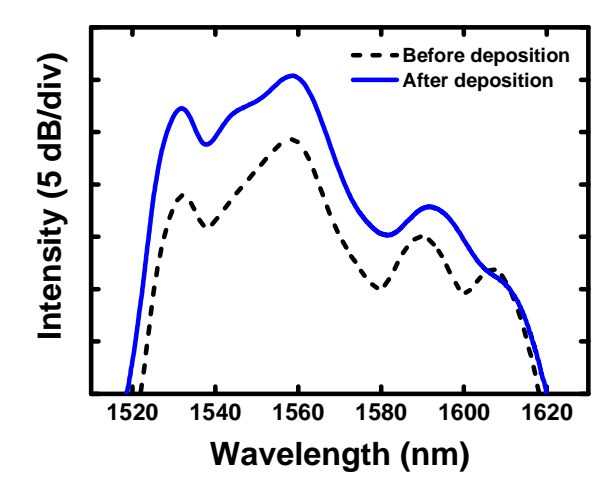


Fig. 3 Output spectrum of the joint fiber segment before (dashed line) and after (solid line) deposition of CNTs onto the cleaved MMF end face.

III. EXPERIMENT AND DISCUSSION OF RESULTS

In order to carry out the RI characterization, test solutions of different sugar concentrations and hence different RIs, were used to simulate perturbations in RI of the external environment of the sensing probe. These test solutions were prepared by first dissolving sugar into de-ionized (DI) water until a saturated sucrose solution was obtained. Fixed volumes of the saturated sucrose solution were then drawn out and diluted with different volumes of DI water to obtain the test solutions with different RIs. A commercially available refractometer (Krauss DR201-95) was used to measure the RI of each test solution. To minimize the crosscoupling effects between RI and temperature, the characterization process was carried out in a thermally stable environment at an ambient temperature of 23.7 \pm 0.1 °C. The SMF end of the sensing probe was connected to a broadband source (Optical Link Limited CL 15-16ASE) via a circulator as shown in Fig. 4. The back reflected light from the sensing probe was monitored by an optical spectrum analyzer (OSA, Ando AQ6317B). 1 ml of each of the test solutions was dropped on a glass slide and the sensing probe was then completely immersed in the test solution and the corresponding variation in intensity of the spectral features in the output spectra was recorded on the OSA. The sensing probe was properly rinsed with DI water and allowed to dry in between test solutions. It was ensured that the reflected spectrum when the sensing probe was exposed to air, as shown in Fig. 3 (solid line), was recovered before the sensing probe was immersed in the next test solution.

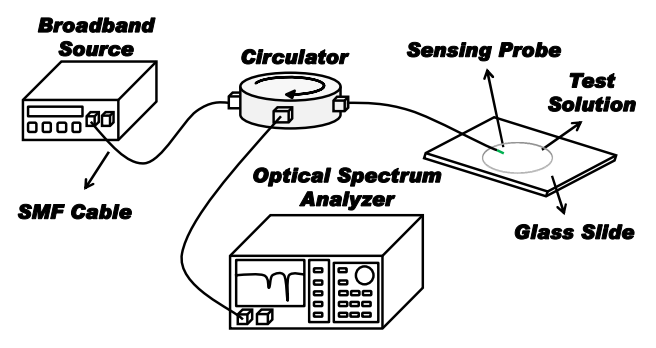


Fig. 4 Experimental setup of the RI measurements with the fabricated sensing probe.

The behavior of the sensing probe to RI perturbations in the external environment for the entire characterization process is shown in Fig. 5. The interference peak at 1558.84 nm was monitored for any observable variations. This peak was chosen due to its close proximity to that of the telecommunications wavelength of 1550 nm where the conventional SMF operates with minimal power attenuation. As can be seen from the figure, there is an observable decrease in the intensity of the interference peak with an increase in RI of the external environment. It can also be seen that data from RIs higher than that of the MMF core (1.4446) could be continuously recorded without the need for new reference points to be obtained first.

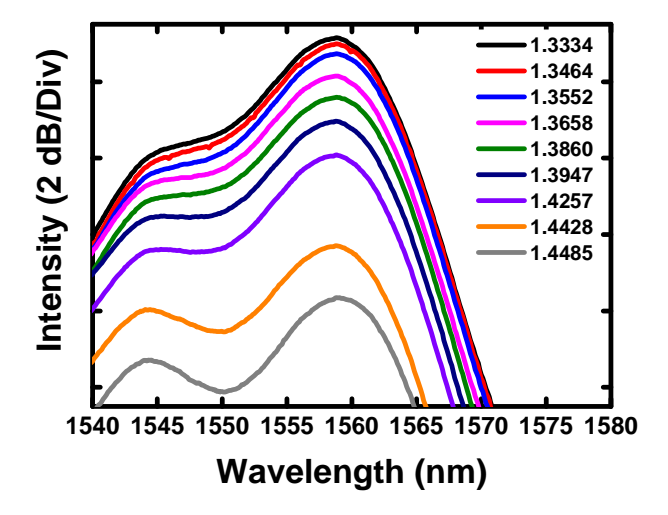


Fig. 5 Variations in intensity of the interference peak at 1558.84 nm of the sensing probe due to RI perturbations in the external environment.

To test the repeatability of the sensing probe, a second trial was carried out for a different set of RIs after a month. The variation in intensity of the interference dip due to RI perturbations in the external environment for both trials is plotted in Fig. 6. The intensity at each RI value, for both trials were plotted in relation to the intensity corresponding to the lowest RI value for the respective trials (1.3331 for trial 1 and 1.3334 for trial 2). A single line was fitted through all the data points (diamonds for trial 1 and circles for trial 2) for both trials. It can be seen that the sensing probe exhibited a nonlinear variation in intensity as the RI of the external environment increased. This nonlinear behavior is to be expected where a variation in RI of the external environment would lead to a nonlinear variation in the amount of reflectance. From here, the sensitivity of the sensing probe was calculated to be approximately 35.8 dB/RIU for the RI range of 1.33-1.40 and approximately 98.8~dB/RIU for the RI range of 1.40-1.46.

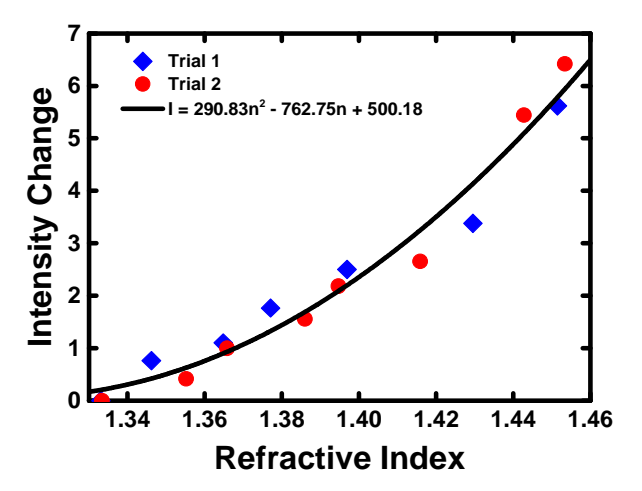


Fig. 6 Plot of the intensity values of the same interference peak corresponding to the various RIs of the external environment for two separate trials.

IV. SUMMARY

In summary, a refractive index (RI) sensing probe, fabricated through fusion splicing a multimode fiber (MMF) segment to a single mode fiber (SMF) and depositing carbon nanotubes (CNT) onto the MMF end face of the resulting joint fiber segment, has been presented. The MMF enabled the excitation of higher order modes which led to the formation of interference peaks and dips which served as accurate reference points for RI measurements. The high RI of the deposited CNTs enabled the continuous detection of a wider range of RIs. The sensing probe displayed clear and distinct variations in its output spectrum to perturbations in RI of its external environment. The achievable sensitivity was calculated to be approximately 35.8 dB/RIU for the RI range of 1.33-1.40 and approximately 98.8 dB/RIU for the RIs of 1.40-1.46. The sensing probe also demonstrated good repeatability and stability behaviors as the RI of the external environment varied. Due to its ability to measure variations in RI and temperature through variations in intensity and shifts in wavelength, respectively, such a sensing probe would be able to resolve any RI-temperature related crosscoupling effects in its RI measurements and possibly function as a dual parameter sensor.

REFERNCES

- [1] H. Meng, W. Shen, G. Zhang, C. Tan, and X. Huang, "Fiber Bragg grating-based fiber sensor for simultaneous measurement of refractive index and temperature," *Sens. Actuators, B*, vol. 150, no. 1, pp. 226-229, Sep. 2010.
- [2] C. Guan, X. Tian, S. Li, X. Zhong, J. Shi, L. Yuan, "Long period fiber grating and high sensitivity refractive index sensor based on hollow eccentric optical fiber," *Sens. Actuators, B*, vol. 188, pp. 768-771. Nov. 2013.Q. Li, X. L. Zhang, Y. S. Yu, Y. Qian, W.
- [3] B. Gu, W. Qi, J. Zheng, Y. Zhou, P. P. Shum and F. Luan, "Fiber Bragg grating-based fiber sensor for simultaneous measurement of refractive index and temperature," *Opt. Lett.*, vol. 39, no. 1, pp. 22-25, Jan. 2014.
- [4] W. C. Wong, C. C. Chan, L. H. Chen, Z. Q. Tou, and K. C. Leong, "Highly sensitive miniature photonic crystal fiber refractive index sensor based on mode field excitation," *Opt. Lett.*, vol. 36, pp. 1731-1733, May 2011.

- [5] Q. Wu, Y. Semenova, P. Wang, G. Farrell, "A comprehensive analysis verified by experiment of a refractometer based on an SMF28- Small-Core Singlemode fiber (SCSMF) -SMF28 fiber structure", J. Opt., vol. 13, no. 12, pp. 125401, Dec. 2011
- [6] S. Silva, O. Frazão, J. L. Santos, and F. X. Malcata, "A reflective optical fiber refractometer based on multimode interference," *Sens. Actuators*, B, vol. 161, no. 1, pp. 88-92, Jan. 2012.
- [7] W. C. Wong, C. C. Chan, Y. F. Zhang, and K. C. Leong, "Miniature single-mode fiber refractive index interferometer sensor based on high order cladding mode and core-offset," *IEEE Photon. Technol. Lett.*, vol. 24, no. 5, pp. 359-361, Mar. 2012.
- [8] C. Gouveia, G. Chesini, C. M. B. Cordeiro, J. M. Baptista, and P. A. S. Jorge, "Simultaneous measurement of refractive index and temperature using multimode interference inside a high birefringence fiber loop mirror," *Sens. Actuators*, B, vol. 177, pp. 717-723, Feb. 2013.
- [9] J. Zhou, Y. Wang, C. Liao, B. Sun, J. He, G. Y, S. Liu, Z. Li, G. Wang, X, Zhong and J. Zhao, "Intensity modulated refractive index sensor based on optical fiber Michelson interferometer," *Sens. Actuators, B*, vol. 208, pp. 315-319, Mar. 2015.
- [10] M. H. Tu, T. Sun and K. T. V. Grattan, "Optimization of gold-nanoparticle-based optical fibre surface plasmon resonance (SPR)-based sensors," *Sens. Actuators*, *B*, vol. 164, no.1, pp. 43-53. Mar. 2012
- [11] Z. Q. Tou, C. C. Chan, W. C. Wong, and L. H. Chen, "Fiber optic refractometer based on cladding excitation of localized surface plasmon resonance," *IEEE Photon. Technol. Lett.*, vol. 25, no.6, pp. 556-559, Mar. 2013.
- [12] H. Tu, T. Sun, and K. T. Grattan, "SPR-based optical fiber sensors using gold-silver alloy particles as the active sensing material," *IEEE Sensors J.*, vol. 13, no. 6, pp. 2192-2199, Jun. 2013.
- [13] J. Wang, Y. Jin, Y. Zhao, and X. Dong, "Refractive index sensor based on all-fiber multimode interference," *Optik*, vol. 124, no. 14, pp. 1845-1848, Jul. 2013.
- [14] Y. Li, L. Chen, E. Harris and X. Bao, "Double-Pass In-Line Fiber Taper Mach–Zehnder Interferometer Sensor," *IEEE Photon. Technol. Lett.*, vol. 22, no. 23, pp. 1750-1752, Dec. 2010.
- [15] P. F. Wang, G. Brambilla, M. Ding, Y. Semenova, Q. Wu, and G. Farrell, "High-sensitivity, evanescent field refractometric sensor based on a tapered, multimode fiber interference," *Opt. Lett.*, vol. 36, no. 12, pp. 2233-2235, Jun. 2011.
- [16] W. Ji, H. H. Liu, S. C. Tjin, K. K. Chow, and A. Lim, "Ultrahigh sensitivity refractive index sensor based on optical microfiber," *IEEE*, *Photon. Technol. Lett.*, vol. 24, no. 20, pp. 1872-1874, Oct. 2012.
- [17] W. Ji, Y. C. Tan, B. Lin, S. C. Tjin, and K. K. Chow, "Non-adiabatically tapered microfiber sensor with ultra-short waist," *IEEE Photon. Technol. Lett.*, vol. 26, pp. 2303-2306, Sep. 2014.
- [18] G. Salceda-Delgado, D. Monzon-Hernandez, A. Martinez-Rios, G. A. Cardenas-Sevilla, and J. Villatoro, "Optical microfiber mode interferometer for temperature-independent refractometric sensing," *Opt. Lett.*, vol. 37, no. 11, pp. 1974-1976, Jun. 2014.

- [19] M. Smietana, D. Brabant, W. J. Bock, P. Mikulic, and T. Eftimov, "Refractive-index sensing with inline core-cladding intermodal interferometer based on silicon nitride nano-coated photonic crystal fiber," *J. Lightw. Technol.*, vol. 30, no. 8, pp. 1185-1189, Apr. 2012.
- [20] J. R. Zhao, X. G. Huang, W. X. He, and J. H. Chen, "High-resolution and temperature-insensitive fiber optic refractive index sensor based on fresnel reflection modulated by Fabry-Perot interference," *J. Lightw. Technol.*, vol. 28, no. 19, pp. 2799-2803, Oct. 2010.
- [21] Q. Li, X. L. Zhang, Y. S. Yu, Y. Qian, W. F. Dong, Y. Li, J. G. Shi, J. T. Yan, H. Y. Wang, "Enhanced sucrose sensing sensitivity of long period fiber grating by self-assembled polyelectrolyte multilayers," *React. Funct. Polym.*, vol. 71, no. 3, pp. 335-339, Mar. 2011.
- [22] K. S. Kim, Y. Mizuno, M. Nakano, S. Onoda, and K. Nakamura, "Refractive index sensor for liquids and solids using dielectric multilayer films deposited on optical fiber end surface," *IEEE Photon. Technol. Lett.*, vol. 23, no. 20, pp. 1472-1474, Oct. 2011.
- [23] C. Wu, B. O. Guan, C. Lu, and H. Y. Tam, "Salinity sensor based on polyimide-coated photonic crystal fiber," *Opt. Express*, vol. 19, no. 21, pp. 20003-20008, Oct. 2011.
- [24] Y. C. Tan, W. B. Ji, V. Mamidala, K. K. Chow, and S. C. Tjin, "Carbon-nanotube-deposited long period fiber grating for continuous refractive index sensor applications," *Sens. Actuators, B*, vol. 196, pp. 260-264, Jun. 2014.
- [25] Y. C. Tan, Z. Q. Tou, V. Mamidala, K. K. Chow, and C. C. Chan, "Continuous refractive index sensing based on carbon-nanotubedeposited photonic crystal fibers," *Sens. Actuators*, B, vol. 202, pp. 1097-1102, Oct. 2014.
- [26] Y. C. Tan, Z. Q. Tou, K. K. Chow, and C. C. Chan, "Graphene-deposited photonic crystal fibers for continuous refractive index sensing applications," *Opt. Express*, vol. 23, pp. 31286-31294, Nov. 2015.
- [27] E. B. Li, X. L. Wang and C. Zhang, "Fiber-optic temperature sensor based on interference of selective higherorder modes," Appl. Phys. Lett., vol. 89, pp. 0911191-09111913, Apr. 2006.
- [28] J. W. Nicholson, R. S. Windeler and D. J. DiGiovanni, "Optically driven deposition of single-walled carbon-nanotube saturable absorbers on optical fiber end-faces," *Opt. Express*, vol. 15, no. 15, pp. 9176-9183, Jul. 2007.
- [29] K. Kashiwagi, S. Yamashita and S. Y. Set, "In-situ monitoring of optical deposition of carbon nanotubes onto fiber end," *Opt. Express.*, vol. 17, no. 7, pp. 5711-5715, Mar. 2009.
- [30] V. A. Margulis and E. A. Gaiduk, "Nature of near-infrared absorption in single-wall carbon nanotubes," *Phys. Lett. A*, vol. 281, no. 1, pp. 52-58, Mar. 2001.
- [31] M. Consales, A. Crescitelli, M. Penza, P. Aversa, P. D. Veneri, M. Giordano, A. Cusano, "SWCNT nano-composite optical sensors for VOC and gas trace detection," *Sens. Actuators, B*, vol. 138, no. 1, pp. 351-361, Apr. 2009.
- [32] H. A. Macleod, Thin-film optical filters/ H. Anglus Macleod, 4th ed. Boca Raton, FL: CRC Press/Taylor & Francis, c2010., 2010.